UNIVERSITÀ DI PISA

SORBONNE UNIVERSITÉS

DIPARTIMENTO DI FISICA "E. FERMI"
CORSO DI LAUREA MAGISTRALE IN FISICA

MASTER 2: PHYSIQUE DES PLASMAS
ET DE LA FUSION

A STUDY OF MAGNETIC RECONNECTION IN NEAR-EARTH SPACE

Master Thesis

Candidate:
Giulia COZZANI

Supervisors:
Dr. Alessandro RETINÒ
Prof. Francesco CALIFANO

Graduation Session September 2016
Academic Year 2015/2016

Unviersità di Pisa & UPMC Sorbonne Universités

Abstract

A study of magnetic reconnection in near-Earth space

Giulia Cozzani

Magnetic reconnection is a fundamental process by which two plasmas with different magnetic fields interact, changing the magnetic field topology, and transferring energy from the magnetic field to particles, resulting in electron and ion acceleration and heating. It is a multi-scale process: the small spatial and temporal scales are strongly coupled with the large scales. Although magnetic reconnection can be individuated in a bunch of different situation in space plasmas, we are interested in reconnection processes driven by the interaction between the solar wind and the magnetosphere. This work focuses on asymmetric reconnection - in which the two reconnection plasmas have different features - produced at Earth's magnetopause. In this study, we propose a study of magnetic reconnection focused on the microphysics of the process, which is still poorly understood. In particular, we investigate the relative contributions of various terms in the generalized Ohm's law by means of *in situ* measurements by the Magnetospheric Multiscale (MMS) mission. MMS is a NASA four-spacecraft constellation mission launched in 2015 with the aim to conduct a definitive experiment to determine the causes of collisionless magnetic reconnection.
The evaluation of Ohm's law has always been a challenge because of the lack of high resolution data preventing the achievement of a proper computation of the electron scale terms of Ohm's law. Indeed, the computation of the pressure and the inertia term using *in situ* measurements has never been achieved with data from previous missions.
We consider the event of October, 3 2015 in which several consecutive magnetopause crossings occurred. Around 1500 UTC the MMS satellites were located in the afternoon side of magnetosphere and separated by a distance of about 20 km. The analysis focuses in particular on two consecutive complete crossings: during the first crossing signatures of reconnection are observed while these are absent in the second one. We report an encounter with an ion diffusion region. Then, we compute of all the terms of the generalised Ohm's law. Since the spacecraft did not cross the electron diffusion region, we expect the inertia and the pressure terms to be negligible compared to the others. This is what is found at the end of the analysis: the reconnection electric field is mainly sustained by the Hall term in presence of reconnection; ideal Ohm's law holds when reconnection stops.

Acknowledgements

I would like to thank my supervisor Dr. Alessandro Retinò for giving me the possibility to work with him and the *plasmas spatiaux* team of LPP during this months. He always gave me the possibility to express my thoughts and doubts and he left me a lot of freedom in my research. I want to thank the members of the LPP/LERMA that have welcomed me and with who I shared scientific discussions (and beers): Olivier Le Contel, Laurent Mirioni, Ilyasse, Roberto, Vivien, Hugo, Francesca, Julien, Loïc, Benjamin, Julie. A special thank to Alexandros who managed to spend some of his time on helping me in my very first days in the lab (and afterwards as well).
I want to thank the team of the IRF-Uppsala, in particular the PhD students that have been so welcoming during the MMS-SWT meeting I attended. A special thank to Daniel and Cecilia for their help with Matlab.
I express my gratitude to Prof. Francesco Califano. In quality of my 'italian' supervisor, he constantly gave me precious advices about my master thesis work. In addiction, together with Prof. Philippe Savoini, he organised the double master degree between Università di Pisa and UPMC Sorbonne Universités I have taken part to, giving to me the priceless opportunity to spend my last year of master studies in Paris.

Somebody said that Paris is a moveable feast but I am sure that I would not agree if it was not for all the people of the First Floor Pasteur. Thank you for everything. *Auf uns!*
Then, I want to thank Marco and Ambra, Marc, Nicolas and David for all the nice time spent together in France and in Italy.

Being one year far from home, I discovered that some things never change. I am grateful to my dearest friends Chiara, Giulia (Borri), Irene, Valentina, Greta.
I would love to thank the friends that I met in my beloved Pisa, especially Federico and Giuseppe.

A special thank to my friend Bianca, for all the years so close, for the years so distant.

A chapter on its own has to be dedicated to Paolo, Francesco (Mache) and Marcello: *La Spezia Gang*. We shared everything in these years. I have learnt so much from all of you during all our discussions - and fights. Not only in a scientific way (since you all have brains with superpowers) but also in a philosophical way.

Now, it's time for family. I am grateful to all of you: I owe a lot to the trust you place in me.
I would love to thank Fabio who wants to live freely and to my grandmother Carmen with her endless strength.
I am grateful to my father, Ettore and to my mother, Gianna because they taught me *a pensare con la mia testa* and to be brave enough to be myself.

At the end, I want to thank Marcello *but, looking for a phrase, I found none to stand beside your name.*

Contents

Introduction

Magnetic reconnection is a process able to produce a topological rearrangement, at large scale, of the magnetic field. It is known to occur in interplanetary space and in the solar corona where it is responsible for solar flares and the disconnection events known as coronal mass ejections, [1], [2]. Far to be a topic of interest only in the astrophysical environment, active research is also being conducted on reconnection in the laboratory and specifically in magnetic-confinement fusion devices in which reconnection is a limiting factor in achieving and maintaining electron temperatures high enough to initiate fusion [3].

This phenomenon has fundamental consequences on the energy transfer between the magnetic field and the plasma flow and particles: reconnection leads to a field topology with lower magnetic energy, the result is that the particles gain kinetic energy. In this thesis, we intend to investigate the process by *in situ* observations in the near-Earth space. Here, plasma density is of the order of $\sim 1 - 10\ cm^{-3}$ so that collisions between particles are usually negligible, and the plasma can be considered collision-less.
Historically, the idea of magnetic reconnection was proposed for the first time by Giovannelli [4] in 1946 in order to explain solar flares. In 1961, Dungey [5] realized how reconnection at the subsolar magnetosphere and in the magnetotail could explain many of the features of the polar cap and the aurora. Then, the first models [6], [7] were considering *resistive* reconnection. The well-known Sweet-Parker model [8], [9] quantifies the properties of collisional reconnection. The reconnection rate predicted by the Sweet-Parker model was too little to explain observations, leading to the development of a faster model, the so-called Petschek's model [10] in which magnetic field line curvature helps accelerate the plasma. However, it was realized that the collisional theory does not apply to all the scenarios, in particular it does not reproduce *magnetopause* reconnection. As a result, it is not possible to explain the irreversible dissipation required for field lines to break in an essentially collisionless plasma using the *resistive* approach so that different aspects of the process are still poorly understood, among them we can cite the onset for collisionless reconnection.

Although magnetic reconnection can be individuated in a bunch of different situation in space plasmas, we are interested in reconnection processes driven by the interaction between the solar wind and the magnetosphere. In particular, in this thesis we intend to investigate the process occurring at the *magnetopause*. The solar wind is composed by the solar magnetic field (with its peculiar configuration caused by the rotational motion of the sun) and by the particles of the plasma with typical velocities of $\sim 40\ km/s$ for protons and $\sim 350 - 400\ km/s$ for electrons.

Since the solar wind is a ultrasonic and ultralfvenic plasma, the interaction between it and the Earth environment gives rise to a *bow shock*. The result is the presence of a region between the external space and the magnetosphere, the *magnetosheath*, characterised by turbulence, by increment in density and temperature and where the plasma becomes subsonic. The next region, going Earthward, is the *magnetosphere*, separated from the *magnetosheath* by the *magnetopause*. The *magnetopause* is a layer characterised by strong currents due to the spatial variation of the magnetic field from the *magnetosheath* to the *magnetosphere*. Being its thickness in general negligible compared to the other regions, it is usually modelised as a 2D layer, [11].

Earth's magnetopause offers the perfect conditions for the observations: in this region, magnetic reconnection is responsible of merging terrestrial and interplanetary magnetic fields to produce an open field line geometry that allows mass and momentum transfer from the solar wind into the magnetosphere. Magnetopause reconnection constitutes then an ubiquitous example of coupling across different spatial scales in which the breaking of the *frozen in* condition occurs as a result of kinetic processes occurring on electron scales while the release of the magnetic energy is manifested on a global scale.

In this thesis, data from the MMS *Magnetospheric Multiscale* mission will be used [12]. These data are a unique opportunity for the experimental study of magnetic reconnection since electrons scales are accessible for the first time. The target regions of MMS are the boundaries of the Earth's magnetosphere, in particular in the day-side region and in the magnetic tail, [14], [15]. One of the fundamental purposes of this mission is to determine the trigger of reconnection in a collisionless plasma and to distinguish between the interplay of the ions and electrons physics around the reconnection layer. These points are the two major problems of reconnection since *i*) the conditions for reconnection to occur are still poorly understood and *ii*) the electrons physics is at the moment investigated only by means of numerical simulations. In this regard, experiments in laboratory can't give exhaustive replies because in a laboratory experiment *i*) the *onset* conditions that lead to reconnection must be prepared "a priori" and *ii*) because of the technical difficulties to measure the electron distribution function or more generally the physics occurring at the electron scale in the reconnection layer. *In situ* observations are then essential in order to achieve a complete understanding of this scenario.

The main goal of my thesis is then to analyse the MMS data in order to describe the microphysics of reconnection. In particular, once reconnection is ongoing an electric field is produced. Using a fluid approach, this field can be described through the generalized Ohm's law (in SI units) $\mathbf{E} + \mathbf{u} \times \mathbf{B} = \mathbf{R}$, where $\mathbf{R}$ contains the Hall term, the electron inertia term, the electron pressure term and the resistive term. While $\mathbf{R}$ is negligible in the region where *ideal* MHD holds, it has to be taken into account in the reconnection site, where the *frozen in* conditions are not valid. My purpose is then to compute and then compare every term present in $\mathbf{R}$ at the highest resolution available, given by the MMS mission. It exists only one example of that, a paper by Torbert *et al.* [16] published in June 2016 during the writing of this thesis. There have been already attempts to do that [17], [18] but a complete estimation of the Ohm's law was no achievable since the computation of some terms, for example the one $\propto \nabla \cdot \overline{\mathbf{P}}_e$ (the divergence of the electrons pressure tensor) needs data at the electron scales resolution. That has been already done in

simulations, for example by Che *et al.* [20] but the same result using *in situ* measurements can be achieved only with MMS data.

In this thesis

In the following, we shall give an outline of the work by summarizing the content and the main ideas of each chapter.

Chapter 1: Theoretical background

We set the theoretical basis that will be useful for the comprehension of this work. In section 1.1, after giving a definition of the plasma state, we introduce the theory of Magnetohydrodynamics (MHD) focusing in particular on its applicability conditions. In section 1.2 the *ideal* MHD is described: the *fronzen in* condition its the most important feature, leading to the same dynamics for the magnetic field and the particles of the plasma.
The first part of section 1.3 will be devoted to the description of the Sweet-Parker and the Petscheck models, both based on the presence of a not negligible resistivity. Even if during this work we deal with the process of *collisionless* reconnection, we report them for their historical importance since they are the two first models attempting to explain magnetic reconnection and they set the base for the following studies. Section 1.3.3 finally describes *collisionless* reconnection and it is devoted primarily to the analysis of the Ohm's law. Ohm's law is a key point in this approach since it clarifies the fundamental multi-scales nature of the reconnection process. On the other hand, the computation of all the terms in Ohm's law is also the aim of this work. Section 1.4 lists some evidences of reconnection that one should be able to observe in presence of a reconnection event. Finally, section 1.5 briefly characterises the environment in which the process we are looking at takes place: the plasma in the near-Earth space.

Chapter 2: Methods of data analysis

This chapter is mainly devoted to the description of different methods leading to the determination of the local frame of a structure such as a current sheet. It is desirable to examine it in its proper co-moving frame since there it appears as time stationary as the data permit and we are able to eliminate the effects due to the relative movement of the spacecraft and the studied discontinuity. Our aim is also to determine the physical dimension of the structure, so we have to establish the frame velocity. In order to find this frame and its velocity several methods have been developed. In this chapter, we give a description of methods that will be used in the data analysis. In section 2.1.1 we describe the Minimum Variance Analysis method, a single spacecraft method used in order to find a coordinate frame composed by vector normal to the studied structure and the other two vectors directed tangentially to the structure. In this work, the Minimum Variance method is applied to the magnetic field. Section 2.1.1.2 is then devoted to the definition of errors to apply to the directions found with the MVA method.
Section 2.1.2 deals with the *deHoffmann-Teller* method. It is a single spacecraft method meant

to determine the velocity of the analysed structure. Definition of the deHoffmann-Teller velocity's error and analysis of velocity's stability over time is then shown in section 2.1.2.1. The last adopted method is the timing method, explained in section 2.1.3. It differs from the others because it is a multi-spacecraft method. It allows to get the direction of the normal to the structure and also the structure's velocity along the normal direction. The reference for the first part of the chapter is [25]. In particular, chap.8 and chap.11 for the Minimum Variance Analysis, chap.9 for the *deHoffmann-Teller* method and chap.12 and 13 for the timing method.
The last part of the chapter addresses the problem of the current computation giving a description of the *curlometer* technique. It deals with a multi-spacecraft technique that allows to compute the electric current density at the barycentre of a tetrahedron by using four-point magnetic field measurements.

Chapter 3: Instruments and data product

The bulk of our analysis uses data from the MMS mission, [12], [14], [15], [22]. The MMS mission design is fundamentally different from other multispacecraft magnetospheric missions in that it targets the electron diffusion region, which the four identically instrumented spacecraft, flying in a tetrahedral configuration, probe over a range of interspacecraft separations.
This chapter is divided in two parts. In the first one, an overview of the mission is proposed. In particular, we will present the main new features of the mission, its target and the requirements to reach it. In sections 3.1.1, 3.1.2 and 3.1.3 the orbit, the constellation features and the data products are detailed.
The second part of the chapter is dedicated to the instruments whose data are used in this thesis. It addresses in particular the basic principles, operating modes and data products of those instruments. Section 3.2.1 contains the description of the spin-double probes that together with the axial double probes (section 3.2.2) yields the measurements of the electric field. The analog and the digital magnetometer are described in section 3.2.3 and they yield measurements of the magnetic field. Finally, section 3.3 focuses on the fast plasma investigation instrument which is responsible for the measurements of the distribution function and the momenta of the plasma.

Chapter 4: Observations: the event of October, 3 2015

In this chapter the first part of my work is presented. The bulk of the thesis is composed by the analysis of data from the Magnetospheric Multiscale (MMS) mission. We are interested on the event of October 3, 2015, since around 1500 UT two complete magnetopause crossings occured and they presented the proper features for reconnection.
Since the analysis focuses on repeated magnetopause crossings, as already underlined in chapter 2, the first thing to do is individuate the proper frame of the magnetopause. Then, we characterise the boundary with its velocity and its width. In order to compute the discontinuity local frame and the discontinuity's velocity, the methods explained in chapter 2 are used. They are single or multi-spacecraft methods. In section 4.1 the Minimum Variance method is used. It needs only the magnetic field data. We perform the analysis on each crossing separately and

we obtain two local discontinuity frames that are quite different. We conclude that the magnetopause is moving fast and in a way that does not allow us to define a single local frame able to describe the discontinuity along the entire interval containing two crossings. We define a local frame for the first crossing (section 4.1.1) and a local frame for the second (section 4.1.2).
In section 4.2 the *timing* method is applied to each crossing. We find a good agreement with the results of the MVA method, especially for the first crossing, while the structure of the signal during the second one does not allow such a good accordance. The *timing* method yield also the normal component of the velocity. Thanks to that, the width of the magnetopause crossed by the spacecraft is computed in section 4.2.1. Another estimation of the normal component of the velocity is given by the *deHoffmann-Teller* method. Results are shown in section 4.4. There is a quite good agreement with the values we get from the *timing* method.
The last section of the chapter is devoted to the computation of the current density, exploiting both the *curlometer* technique and the data from the *FPI* instrument. This analysis shows that currents computed with the two different methods have globally the same behaviour and that the current density peaks in correspondence of the magnetic field inversions.

Chapter 5: Electric field calibration

This short chapter contains the re-calibration that has been operated on the electric field data. During the data analysis, we realised the presence of an offset in the electric field that needed to be fixed. In fact, in the magnetosheath region, an almost constant gap was present between the electromagnetic velocity computed with the *l2* electric field data and the velocity obtained with the *FPI* instrument, directly from the particles data. The presence of such a gap would have meant that the particles were decoupling from the magnetic field. Since there was no reason for this to happen in that region we concluded that it was the result of a calibration problem. In this chapter we illustrate in details the calibration procedure we adopted to fix this problem.

Chapter 6: Evaluation of the terms of Ohm's law

Chapters 4 set all the basis for the data analysis in the local frame of the magnetopause. This is essential, as we already underlined before, since in this way we are able to look at the data without the effects that rotations and motion could induce on them. Furthermore, only in that way a fruitful comparison with the results from simulation can be conducted.
In this chapter, we continue the analysis of the event of October,3 2015, characterised with two consecutive magnetopause crossings, with the aim of computing all the terms of the generalised Ohm's law and to understand their contribution to the electric field during magnetic reconnection. Section 6.1 analyses in details the two crossings and individuates the presence of evidences of reconnection throughout the first one (Hall field signature, particle acceleration) while these are not present anymore at the time of the second crossing. A comparison between the electric and $\mathbf{v}_i \times \mathbf{B}$ and $\mathbf{v}_e \times \mathbf{B}$ allows to identify an ion diffusion region.
Section 6.2 is devoted to the computation of the electric field parallel to the magnetic field. This is always a tricky quantity to measure because of the value of the electric field, usually of the same order of the error bar. We manage to individuate a DC electric field lasting ~ 1 s during

the first crossing that confirms the reconnection's signatures identified before.
In the last part of the chapter we deal with the computation of the terms of the generalised Ohm's law. Section 6.3 starts presenting the results that have been achieved until now with data from the previous missions [17], [18] and conclusions from simulations [20], [21]. Then we present our results: we report an encounter with a ion diffusion region in the first crossing, Ohm's law's predominant term is the Hall term as expected. During the second crossing we do not observe reconnection, the ideal Ohm's law holds. In the last section of the chapter we apply our scripts to the data ot October,16 in order to check them. We obtain a good agreement with the results of [16].

Chapter 7: Conclusions and outlook

In this chapter we summarize the main concepts and results of this thesis and discuss possible future work.

All the numerical analyses and plots have been realized by means of the software MATLAB.

Chapter 1

Theoretical background

In this chapter, we set the theoretical basis that will be useful for the comprehension of this work. In section 1.1, after giving a definition of the plasma state, we introduce the theory of Magnetohydrodynamics (MHD) focusing in particular on its applicability conditions. In section 1.2 the *ideal* MHD is described: the *fronzen in* condition its the most important feature, leading to the same dynamics for the magnetic field and the particles of the plasma.
The first part of section 1.3 will be devoted to the description of the Sweet-Parker and the Petscheck models, both based on the presence of a not negligible resistivity. Even if during this work we deal with the process of *collisionless* reconnection, we report them for their historical importance since they are the two first models attempting to explain magnetic reconnection and they set the base for the following studies. Section 1.3.3 finally describes *collisionless* reconnection and it is devoted primarily to the analysis of the Ohm's law. Ohm's law is a key point in this approach since it clarifies the fundamental multi-scales nature of the reconnection process. On the other hand, the computation of all the terms in Ohm's law is also the aim of this work. Section 1.4 lists some evidences of reconnection that one should be able to observe in presence of a reconnection event. Finally, section 1.5 briefly characterises the environment in which the process we are looking at takes place: the plasma in the near-Earth space.

1.1 Basic theory of Magnetohydrodynamics

A plasma is defined as a collection of a very large number of charged particles, globally neutral, but dominated by the electromagnetic forces. Plasma state is normally named in literature as the *forth state of matter* since a plasma can be thought to be produced by heating an ordinary gas to such temperature that the amount of charged particles drastically affects the system dynamics. Even if on Earth the amount of matter that can be considered plasma is little, the large majority of matter in space is in the plasma state. A plasma is composed by charged particles and for this reason two different tendencies can be seen: a tendency to cohesion, due to the electromagnetic forces; a tendency to disaggregate, due to the chaotic movement of the particles. In general, a plasma can contain atoms and ions pf different kind; by the way, in this work we consider a

simple plasma, composed of neutral particles of the same type (hydrogen in particular), ions of the same kind and electrons.
Studying a plasma system means to deal with a self-consistent problem: the currents and charges are affected by the presence of the electric and magnetic fields; the fields are modified by the charges trough the Maxwell's equations. We will always describe the system in the *non relativistic* limit: $V \ll c$ holds for all the characteristic velocities V of the analysed system.

We list below the Maxwell's equations:

$$\nabla \times \mathbf{E} = -\frac{\partial \mathbf{B}}{\partial t} \qquad \nabla \cdot \mathbf{B} = 0 \tag{1.1}$$

$$\nabla \cdot \mathbf{E} = \frac{\rho}{\epsilon_0} \qquad \nabla \times \mathbf{B} = \mu_0 \, \mathbf{J} \tag{1.2}$$

where we have neglected the *displacement current*, $\varepsilon_0 \frac{\partial \mathbf{E}}{\partial t}$. Indeed, it is easy to show that the *displacement current* term is negligible in the *non relativistic* limit. Let us indicate as L and t_c the characteristic length and time of the system. Then, $|\nabla| \sim 1/L$, $\partial_t \sim 1/t_c$ and $L/t_c = V \ll c$. From Ampère equation and Faraday equation we obtain

$$E \sim V \; B \tag{1.3}$$

$$\frac{B}{L} \sim \mu_0 \; J + \frac{1}{c^2} \frac{E}{t_c} \tag{1.4}$$

Then,

$$\frac{B/L}{E/t_c \; c^2} = \frac{c^2}{V^2} \tag{1.5}$$

so we can see that the term $\propto \frac{\partial \mathbf{E}}{\partial t}$ is negligible compared to the others. Ampère's law is then reduced to $\nabla \times \mathbf{B} = \mu_0 \mathbf{J}$.

There are many approaches to describe a plasma, depending on the level of precision needed and/or on the phenomena that has to be analysed.
The dynamics of the system is described, in general, using a kinetic description via the distribution function and the Vlasov equation ([11], [23]) since space plasmas can be considered as collisionless. The fluid approach, (in particular the multi-fluid approach where each species is described separately and the magnetohydrodynamics approach, where the plasma is modelized as a single fluid) is obtained directly from the kinetic one. Of course, such an approach based on a macroscopic view of the plasma ceases to be valid as soon as the system develops fluctuations comparable to the ion gyroradius. Nevertheless, the magnetohydrodynamics (called MHD in the following) approach is suitable to describe magnetic reconnection, as far as the evolution of large-scales is concerned. Furthermore, these different models can be used at the same time to describe the system: hybrid models are common, especially in the domain of numerical simulation. In these cases a species that has to be studied at a higher level of 'precision' is modelised

using the kinetic approach and the others with the fluid approach; this is only an example of a hybrid model for a plasma.

Note that MHD is based on a number of assumptions on the system dimension and dynamics. Firstly, the system has to behave in a non relativistic way. Then, in order to consider the plasma as a unique fluid the characteristic dimension L of the system and of any fluctuation has to be much larger than the ion Larmor radius ρ_i and the ion inertial length λ_i and the characteristic frequency ω_c has to be much smaller than the ion cyclotron frequency Ω_i. Then, the quasi-neutrality of the plasma ($n_i \sim n_e \sim n$) is required. Since $\rho_e \ll \rho_i$, $\Omega_e \ll \Omega_i$ and $\omega_{pe} \ll \omega_{pi}$ the MHD applicability conditions reduce to:

$$L \gg (\rho_i, \lambda_i) \tag{1.6}$$

$$t_c \gg (\Omega_i^{-1}, \omega_{pi}^{-1}) \tag{1.7}$$

If this is fulfilled, it is possible to consider the plasma in its whole.

The equations of the single fluid model are obtained as the moments of velocity of the kinetic equation, self-consistently coupled to Maxwell's equations. MHD equations are then derived by combining the equation of the multi-fluid model. In order to describe the plasma as one fluid, we define:

$$\rho = \sum_\alpha m_\alpha n_\alpha \quad \text{the density of mass} \tag{1.8}$$

$$\mathbf{u} = \frac{\sum_\alpha m_\alpha n_\alpha \mathbf{v}_\alpha}{\sum_\alpha m_\alpha \, n_\alpha} \quad \text{the velocity of the center of mass} \tag{1.9}$$

$$\mathbf{J} = \sum_\alpha q_\alpha n_\alpha \mathbf{v}_\alpha \quad \text{the current density} \tag{1.10}$$

where α indicates the species. In the following, we will consider plasmas where only electrons and ions are present. The derivation of the equations that constitute the MHD model is not showed here, we enumerate the fundamental ones:

- the continuity equation

$$\frac{\partial \rho}{\partial t} + \nabla \cdot (\rho \mathbf{u}) = 0 \tag{1.11}$$

that states the conservation of mass (we assume that all the processes of ionization and recombination are negligible);

- the motion equation:

$$\frac{\partial \mathbf{u}}{\partial t} + \mathbf{u} \cdot (\nabla \mathbf{u}) = -\nabla \cdot \frac{\overline{\mathbf{P}}}{\rho} + \frac{\mathbf{J} \times \mathbf{B}}{\rho} \tag{1.12}$$

where the term $\overline{\mathbf{P}}$ is the pressure tensor defined as:

$$P_{ij} = \sum_{\alpha} m_{\alpha} \langle (v_i - u_i)(v_j - u_j) \rangle_{\alpha} \tag{1.13}$$

where $v_{i,j}$ are the velocities of the particles in the frame of the laboratory. The system of equation 1.11 - 1.12, together with the Maxwell equations and with an appropriate expression for $\overline{\mathbf{P}}$ (an adequate *equation of state*) constitutes a closed system.

Combining the Maxwell's equations and the equations describing the plasma dynamics we are able to achieve a complete description of the system. In the presence of a finite plasma conductivity σ, the MHD evolution equation for the magnetic field reads:

$$\frac{\partial \mathbf{B}}{\partial t} = \nabla \times (\mathbf{u} \times \mathbf{B}) + \frac{\nabla^2 \mathbf{B}}{\mu_0 \sigma} \tag{1.14}$$

where $\mathbf{u}$ is the fluid velocity of the plasma, see Eq. 1.9. The first term in RHS is called the *convective* term and the second one is the *diffusion* term. Their ratio defines the Raynolds number $R_m = uL\sigma\mu_0$, where L is the characteristic length of the system.
When $\sigma \to \infty$ (or, equivalently, $R_m \to \infty$), the MHD is called *ideal* MHD.

1.2 Plasma and magnetic field: the *frozen in* condition

The equation 1.14 describes the behaviour of the magnetic field in function of the time. The interesting thing is that there is a strong synergy between the particles of the plasma and the magnetic field: the centre of mass velocity $\mathbf{u}$ and the magnetic field $\mathbf{B}$ are linked trough this equation. We consider now a magnetised plasma that can be described with the equations of the *ideal* MHD. In this case:

$$\frac{\partial \mathbf{B}}{\partial t} = \nabla \times (\mathbf{u} \times \mathbf{B}) \tag{1.15}$$

In this condition the *frozen-in* law of the magnetic field holds. This means that the field's lines are linked with the plasma and they can not break. In other words, if a line connecting two plasma particles is tangential to a field line at t_0, it will remain tangential to the same field line at every time:

$$\frac{d}{dt}\, \mathbf{r} \times \mathbf{B} = 0. \tag{1.16}$$

To understand better this concept, we can consider a fluid element of the plasma and the magnetic field's flux within it. If the magnetic field and the plasma are frozen their dynamics is linked: there is no diffusion and the magnetic flux ϕ within the fluid element surface stays constant, even if the fluid element moves or changes its shape. In fact,

$$\frac{d\phi}{dt} = \frac{\partial \phi}{\partial t} + \mathbf{u} \cdot \nabla \phi = \frac{\partial \phi}{\partial t} - \int \mathbf{u} \times \mathbf{B} \cdot \mathbf{dl} \tag{1.17}$$

and if 1.15 is valid, the two terms on the right hand side of 1.17 are the same, so we obtain that the flux of $\mathbf{B}$ trough a fluid element is a constant quantity. This is valid for all the fluid element. If we consider two different fluid element of the plasma, the magnetic flux within each of them is constant. This means that if the same field lines are passing trough the two elements at time t_0, this will be true also at any time t_1. The MHD formulation that contains Eq.1.15 is *ideal* in the sense that there is no diffusion and dissipation.

As a consequence of such frozen-in condition, the magnetic field can not change its topology and every magnetic field line maintains its "identity". This condition represents a strong constraint on the system dynamics.

Furthermore, if we combine the first of Eq. 1.1 with Eq. 1.15 we obtain:

$$\mathbf{E} = -\mathbf{u} \times \mathbf{B} \tag{1.18}$$

This is called ideal Ohm's law. One can see that since the cross-product between any velocity component parallel to the magnetic field and the field itself is zero, any component of the electric field parallel to the magnetic field must vanish when *ideal* MHD holds.
It is interesting to notice that in this condition the velocity of the plasma in the plane perpendicular to $\mathbf{B}$ and of the magnetic field lines are the same:

$$\mathbf{v}_{EM} = \frac{\mathbf{E} \times \mathbf{B}}{B^2} \tag{1.19}$$

There is no diffusion, so the particles and the field have the same dynamics, characterised by $\mathbf{v}_{EM}$.

Even if until this moment the velocity in Eq. 1.14 has been $\mathbf{u}$, the total velocity of the plasma, we can write Eq. 1.14 also for single specie, α. In this case, $\mathbf{v}_\alpha = \mathbf{v}_{EM} = \frac{\mathbf{E}\times\mathbf{B}}{B^2}$ and while the specie α is *frozen* with the magnetic field, the other species may be not.

Until now, we have presented the ideal MHD, where no reconnection can happen. In the next section, we will talk about the process of magnetic reconnection where all these relation do not hold anymore. Nevertheless, the picture depicted in this section is really important because it describes the large scale dynamics of the plasma. In space plasmas, the *frozen in* condition that holds between the plasma and the magnetic field explain the fact that the solar environment (the magnetic field of the Sun, carried along by the *solar wind*) and the Earth's environment (the *magnetosphere*) are seen as separate plasmas, each of them presenting peculiar features. The separation is broken only by process of magnetic reconnection that lead to the mixing of the two different plasmas, in particular to the injection of particles of the solar wind in the Earth's region.

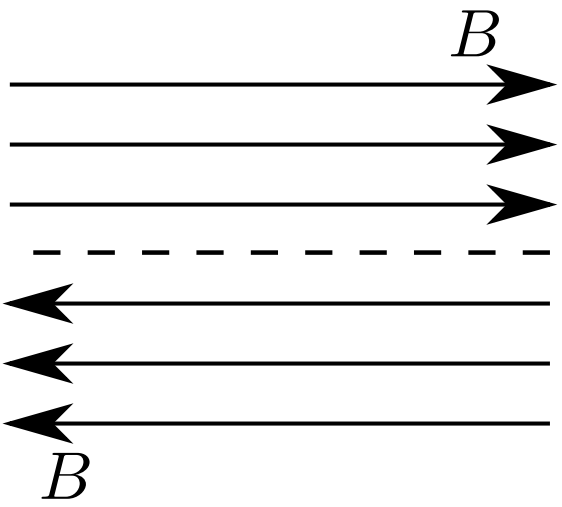

FIGURE 1.1: The initial configuration of the magnetic field

1.3 The process of magnetic reconnection

In order to have a first idea of the process, one can refer to the simplest 2D model of reconnection, in which there are two adjacent zones with anti-parallel magnetic field as we can see in figure 1.1. Being the fields anti-parallel, there is a region in the space where the field reverse its direction. In that region there is a current sheet, as consistent with the Ampère law

$$\nabla \times \mathbf{B} = \mu_0 \, \mathbf{J}.$$

Magnetic reconnection, as already said, is a topological reorganization of the fields lines. Always referring to the typical $2D$ picture, during the process the two field lines break and reconnect around a point. It is called the *X-point* while the lines separating magnetic fields with different topologies are called *separatrices*. The process is schematically shown in figure 1.2.

The first panel of the picture 1.2 represents a field line and two fluid element of the plasma frozen to it at three different times in the case of no reconnection. Nothing special happens in this case, particles and field line stay frozen.
In the second panel we see two field lines, in the same configuration shown in figure 1.1. The little circles indicated with the capital letters represent four fluid elements of the plasma: A and B are initially fronzen to the same field line, the same for C and D. Then, for some reason they are pushed together at time t_2 (in the magnetopause environment, this can be due to the solar wind pushing the magnetosphere) creating a strong current density $\mathbf{J}$. The third image shows the condition at time t_3: the topology of the magnetic field has changed. Now A and C are frozen to the same field line, the same for B and D.

Figure 1.2 is only a sketch but we can obtain some interesting information about the process. First of all, magnetic reconnection appears to be a phenomenon where the main role is played by the electromagnetic field: we did not specify anything about the plasma elements, the only information is that at time t_1 they are taken on a field line. Furthermore, magnetic reconnection is a multiscale process. In fact, the field lines break and reconnect in a region with a dimension

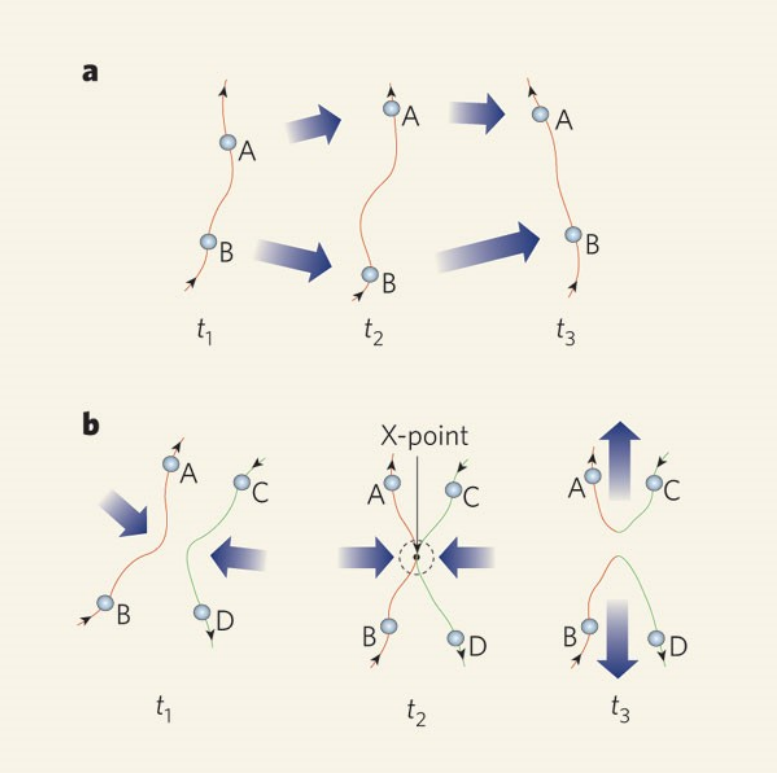

FIGURE 1.2: Time evolution of magnertic field lines in the case of no reconnection (panel *a*) and reconnection (panel *b*). In panel *a* magnetic field lines are generally frozen into the plasma flow (blue arrows), so two fluid elements of plasma, A and B, connected by a field line at time t_1 remain connected by the same field line at all later times. In panel *b*, two oppositely directed field lines, identified by the fluid elements A, B and C, D, respectively, are moving towards each other at time t_1. At time t_2 they break and reconnect at the so-called *X-point*, so that A, C and B, D, are connected at time t_3. Plasma flows out from the region at high speeds. Adapted from [32].

of the order of ρ_e: only in this small region the frozen in condition does not hold for every specie of the plasma. The fluid element A in figure 1.2 stays frozen to the same field line all the time but at time t_3 it is able to reach regions that were inaccessible at time t_1. In a certain sense, A is frozen to a 'different' field line since the magnetic field underwent the process of reconnection. This means that, even if the magnetic reconnection is a local process, its consequences affect the system in its bigger length scales. Therefore, there is a region where the plasma and the fields can not be described by the *ideal* MHD. In this region, Eq. 1.18, 1.15 and 1.16 are not valid anymore.

We have described in the simplest way the process of magnetic reconnection. As we already said, the magnetopause reconnection sees the presence of a collisionless plasma. However, the first attempt to model magnetic reconnection has been accomplished by adding the resistivity term in MHD. It is for this reason that the following of the chapter will host an overview of the Sweet-Parker model of *resistive* reconnection before passing to the *collisionless* description.

1.3.1 Resistive reconnection: the Sweet Parker model

The first attempt to model magnetic reconnection was made by Sweet and Parker in 1956. Their model was based on a collisional plasma.

We adopt the simple geometry already used in the last section: we have two spatial dimensions x and y, assuming z as ignorable . We will consider steady states. The basic configuration is shown in figure 1.3. All field quantities are independent of time. Also, while the magnetic field $\mathbf{B}$ and the plasma velocity $\mathbf{v}$ are assumed to lie in the $x-y$ plane, for the electric field a non-vanishing z-component is admitted. We consider a stagnation-type flow field $\mathbf{v}$ and oppositely directed magnetic fields in the upper and lower part of the inflow region. The magnetic field vanishes at the origin. The magnetic field lines are advected with speed v_1, they reconnect and then they are ejected at speed v_2. We assume stationarity.

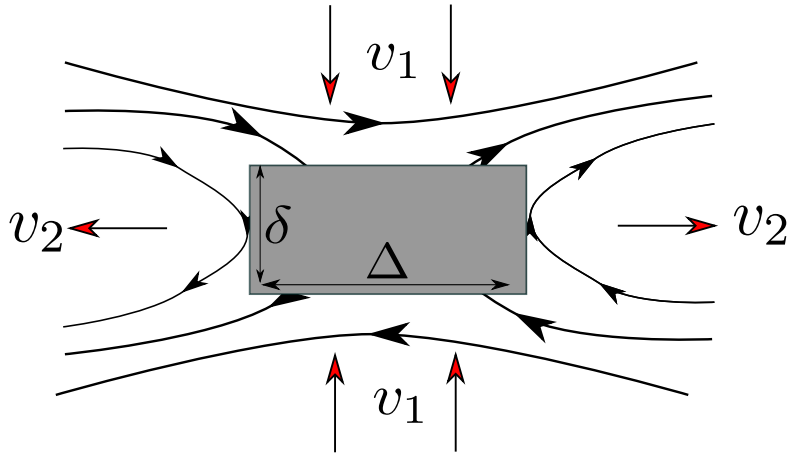

FIGURE 1.3: Pattern of two-dimensional reconnection. The grey rectangle represents the resistive region where reconnection takes place.

The Sweet-Parker model hypothesize the presence of a diffusion region near the neutral line, where a non-neglecting resistivity σ is present. The diffusion region has length scales δ (along the x-direction) and Δ (along the y-direction) that are small compared to the scale of the system L. A locally defined Raynolds number, computed with the characteristic length δ can be considerably smaller than the global Raynolds number: $R_{m,\delta} = u\delta\sigma\mu_0$ and $R_{m,L} = uL\sigma\mu_0$ with $\delta \ll L$. The fact that $\sigma \neq 0$ indicates that in the diffusion region resistive diffusion can play an important role. There, the plasma and magnetic fields may decouple. Starting from Eq. 1.14 and the other equations of the non-ideal MHD that where introduced in 1.1 we obtain the resistive Ohm's law:

$$\mathbf{E} + \mathbf{u} \times \mathbf{B} = \eta \mathbf{J} \tag{1.20}$$

where $\eta = \sigma^{-1}$ is the resistivity of the plasma. This equation is important because it gives information that may be valid also for collisionless reconnection. Even in that case we will have that $\mathbf{E} \neq -\mathbf{u} \times \mathbf{B}$. This means that in the diffusion region an electric field parallel to $\mathbf{B}$ is allowed to exist while this is not true in the ideal MHD region.

Since we assume stationarity, the others equation of the model are the Faraday equation

$$0 = \nabla \times \mathbf{E} \tag{1.21}$$

the equation of the motion

$$\rho(\mathbf{u} \cdot \nabla)\mathbf{u} = -\nabla \cdot \overline{\mathbf{P}} + \mathbf{J} \times \mathbf{B} \tag{1.22}$$

the equation of the evolution of the magnetic field

$$0 = \nabla \times (\mathbf{u} \times \mathbf{B}) + \frac{\nabla^2 \mathbf{B}}{\mu_0 \sigma}. \tag{1.23}$$

We impose also the incompressibility condition $\nabla \cdot \mathbf{u} = 0$. All the inflow and outflow quantities will be indicated respectively with the subscript 1 and 2. Then, from Eq. 1.23 and the incompressibility condition give

$$u_1 \sim \frac{1}{\mu_0 \sigma \delta} \qquad \Delta u_2 = \delta u_1. \tag{1.24}$$

Because of the stationarity condition we also have $u_1 \Delta = u_2 \delta$. Furthermore, since outside of the diffusion region the ideal MHD holds and since the system is stationary we obtain:

$$E_z \sim u_1 B_1 \sim u_2 B_2 \tag{1.25}$$

The *reconnection rate* is defined as the ratio between the inflow velocity and the local Alfvén velocity:

$$\mathcal{R} = \frac{u_1}{V_{A,1}} \tag{1.26}$$

The so-defined reconnection rate should not be confused with the rate of magnetic flux reconnection, which is defined by the rate at which flux conservation is violated in the reconnection process. Therefore,

$$\mathcal{R} \sim \frac{1}{\mu_0 \sigma \delta V_{A,1}} \sim \sqrt{\frac{u_2}{R_{m,1} V_{A,1}}} \tag{1.27}$$

where $R_{m,1}$ is the Raynolds number computed with the Alfvén velocity. If we suppose that the pressure term in Eq. 1.22 is negligible compared to the magnetic one we can write:

$$\frac{\rho u_2^2}{\Delta} \sim j B_2 \tag{1.28}$$

$$\frac{\rho u_2^2}{\Delta} \sim \frac{B_1 B_2}{\mu_0 \delta} \tag{1.29}$$

Then, substituting the expression for u_2 obtained trough Eq. 1.29 and 1.25:

$$u_2^2 \sim \frac{B_1^2}{\mu_0 \rho} \tag{1.30}$$

This relation says that the outflow velocity is of the same order of the Alfvén velocity computed in the inflow region.
The expression for $\mathcal{R}$ becomes:

$$\mathcal{R} \sim \frac{1}{\sqrt{R_{m,1}}} \tag{1.31}$$

As we can see, the reconnection rate is extremely small if we apply this model to a collisionless plasma where we can say that $R_{m,1} \to \infty$ (for example, in the magnetosphere $Rm \sim 10^{11}$).

As we said, we mention this model for historical reasons: it is not suitable to describe the plasma conditions we are looking at. Nevertheless, the Sweet-Parker approach is still interesting because it allows to know some of the typical scales of the process using really simple geometry and hypothesis. On the other side, this model is completely not able to explain the observations.

1.3.2 Resistive reconnection: the Petscheck model

In the frame of resistive reconnection, another important model is the Petscheck's one, [10]. He modified the Sweet-Parker model by introducing a new element. A dissipative region continues to exists (even if the size is reduced) where the presence of a non-zero conductivity allows for the breaking of the field lines. The difference is that the particles of the plasma are not 'obliged' to pass through this region. He proposed the presence of *slow shocks* as the mechanism responsible for the particles acceleration. With this configuration, only a small fraction of the inflowing plasma must go through the diffusion region while the most part of it is accelerated at the slow shocks. The reconnection rate is:

$$\mathcal{R} \sim \frac{1}{log(R_{m,1})} \tag{1.32}$$

where $R_{m,1}$ is the magnetic Reynolds number calculated in the inflow region. Since $log(R_{m,1})$ is a slowly varying function of $R_{m,1}$ the reconnection rate is much higher than the one provided by the Sweet-Parker model. So, this description leads to a reconnection rate $\mathcal{R}$ which is less drastically different from observations that the one obtained with the Sweet-Parker model. Nevertheless, the slow shocks supposed by Petscheck were never conclusively observed in the extensive observations around the Earth's dayside magnetopause and magnetotail.

1.3.3 Collisionless reconnection

In section 1.2, we used Eq. 1.16 to define the *frozen-in* condition. It is natural to say that magnetic reconnection occurs when Eq. 1.16 it is no longer valid, at least in a very thin boundary layer due to the generation of very strong gradients: [1]:

$$\frac{d}{dt}\,\delta\mathbf{r}\times\mathbf{B}\neq 0. \tag{1.33}$$

From this we obtain

$$\frac{d}{dt}\,\delta\mathbf{r}\times\mathbf{B}=\frac{d\delta\mathbf{r}}{dt}\times\mathbf{B}+\delta\mathbf{r}\times\frac{d\mathbf{B}}{dt}=\frac{d\delta\mathbf{r}}{dt}\times\mathbf{B}-\delta\mathbf{r}\times[\nabla\times\mathbf{E}-(\mathbf{v}_{EM}\cdot\nabla)\mathbf{B}] \tag{1.34}$$

where we used Faraday equation. Then,

$$\frac{d\ \delta\mathbf{r}}{dt}=(\delta\mathbf{r}\cdot\nabla)\ \mathbf{v}_{EM} \tag{1.35}$$

$\delta\mathbf{r}$ is an infinitesimal vector connecting two plasma elements, initially frozen to the magnetic field. The two extremities of $\delta\mathbf{r}$ are then moving with the local $\mathbf{v}_{EM}$ velocity. Substituting in 1.34,

$$[(\mathbf{B}\cdot\nabla)\mathbf{v}_{EM}+\nabla\times\mathbf{E}-(\mathbf{v}_{EM}\cdot\nabla)\mathbf{B}]\times\delta\mathbf{r}\neq 0 \tag{1.36}$$

we finally obtain [2]

$$[\nabla\times(\mathbf{E}+\mathbf{v}_{EM}\times\mathbf{B})]\times\delta\mathbf{r}\neq 0 \tag{1.37}$$

This gives a condition for magnetic reconnection based on the electric field:

$$(\nabla\times\mathbf{E}_{||})\times\delta\mathbf{r}\neq 0 \tag{1.38}$$

A parallel electric field as a reconnection sign is already present in the contest of resistive reconnection. Here we have shown that this is true even for the collisionless one. In particular, the non-resistive MHD is characterised by different characteristic length scales.

In this section the *generalised* Ohm's law will be derived. Looking at this equation it will be clear that collisionless reconnection is a multi-scale process.

[1] Here we write $\delta\mathbf{r}$ to underline that it is an infinitesimal vector
[2] The identity $\nabla\times(\mathbf{A}\times\mathbf{B})=\mathbf{A}(\nabla\cdot\mathbf{B})-\mathbf{B}(\nabla\cdot\mathbf{A})+(\mathbf{B}\cdot\nabla)\mathbf{A}-(\mathbf{A}\cdot\nabla)\mathbf{B}$ has been used.

1.3.3.1 Generalised Ohm's law

In order to obtain the Ohm's law in the case of a collisionless plasma, we consider a bi-fluid model.

$$\rho_e \frac{\partial \mathbf{v}_e}{\partial t} + \rho_e(\mathbf{v}_e \cdot \nabla)\mathbf{v}_e = -\nabla \cdot \bar{\mathbf{P}}_e + q_e n_e \mathbf{E} + q_e n_e(\mathbf{v}_e \times \mathbf{B}) + \mathbf{R}_e \tag{1.39}$$

$$\rho_i \frac{\partial \mathbf{v}_i}{\partial t} + \rho_i(\mathbf{v}_i \cdot \nabla)\mathbf{v}_i = -\nabla \cdot \bar{\mathbf{P}}_i + q_i n_i \mathbf{E} + q_i n_i(\mathbf{v}_i \times \mathbf{B}) + \mathbf{R}_i \tag{1.40}$$

The term $\mathbf{R}_\alpha$ is traditionally introduced as function of the collisional term (defined in the frame of the kinetic approach). Even we are focusing on collisionless plasma we do not delete this term from the beginning of this derivation since its presence will be useful for the interpretation of the generalisez Ohm's law.
We multiply 1.39 for $\frac{q_e}{m_e}$ and 1.40 for $\frac{q_i}{m_i}$, then we subtract the two new equations. We remember that $n_i = n_e$. Using the Eq. 1.8, 1.9 and 1.10 we finally obtain

$$\mathbf{E} + \mathbf{u} \times \mathbf{B} = \frac{1}{ne}\mathbf{J} \times \mathbf{B} - \frac{1}{ne}\nabla \cdot \left(\overline{\mathbf{P}}_e - \frac{m_e}{m_i}\overline{\mathbf{P}}_i\right) + \frac{m_e}{ne^2}\left[\frac{\partial \mathbf{J}}{\partial t} + \nabla \cdot (\mathbf{J}\mathbf{u} + \mathbf{u}\mathbf{J})\right] + \mathbf{A}_e \tag{1.41}$$

the *generalised* Ohm's law [3]. Indeed, we can see that the structure of this equation is $\mathbf{E}+\mathbf{u}\times\mathbf{B} =$ **RHS** and that it has the same shape of the Eq. 1.20 introduced in the frame of the resistive reconnection. The only approximations we made in this computation were based on the mass relation $m_e \ll m_i$; the complete derivation can be found in [23]. We have different terms in the RHS of Eq. 1.41:

- the Hall term: $\frac{1}{ne}\mathbf{J} \times \mathbf{B}$;
- the thermoelectric term, due to the pressure gradient: $\frac{1}{ne}\nabla \cdot \left(\overline{\mathbf{P}}_e - \frac{m_e}{m_i}\overline{\mathbf{P}}_i\right)$ which, assuming $\overline{\mathbf{P}}_e \simeq \overline{\mathbf{P}}_i$, reduces to $\frac{1}{ne}\left(\nabla \cdot \overline{\mathbf{P}}_e\right)$;
- the inertia term, due to the electron finite mass: $\frac{m_e}{ne^2}\left[\frac{\partial \mathbf{J}}{\partial t} + \nabla \cdot (\mathbf{J}\mathbf{u} + \mathbf{u}\mathbf{J})\right]$.

The last term derives from the term $\mathbf{R}_e$ in Eq. 1.39 and it is linked with collisionality. In a collisional medium it is possible to write $\mathbf{A}_e$ in function of the resistivity η: $\mathbf{A}_e = \eta\mathbf{J}$. This underlines the fact that Eq. 1.41 is effectively an *Ohm's law*. In the case of collisionless plasmas, several simulations and even the first observations from the MMS mission show that there is not a prefect balance between the RHS and the LHS of Eq. 1.41, [16]. For this reason, a term $\mathbf{A}_e$ is maintained also in the collisionless description. The difference consists in the *source* of this term, in a certain sense in its *meaning*. Now it is no more function of conductivity defined in

[3] Note that the divergence in the square brackets is applied to a tensor. Here and in the following, **ab** does not indicates the dot product but the tensorial product of **a** and **b**.

the traditional way but it points out that it is some other kind of interaction (e.g particle-waves interactions) that has to be taken into account in order to well compute the generalised Ohm's law. It is for this reason that we usually refer to $\mathbf{A}_e$ as the term of *anomalous resistivity* while working with collisionless plasmas.

In order to visualize the fact that the collisionless reconnection is a multi-scale process we evaluate the ratio between the different terms of Eq. 1.41. Let us indicate as L and t_c the characteristic length and time of the system. Then, $|\nabla| \sim 1/L$, $\partial_t \sim 1/t_c$ and $L/t_c = V$. The ratio between the pressure and $\mathbf{u} \times \mathbf{B}$ is:

$$\frac{|\nabla \cdot \overline{\mathbf{P}}_e|/ne}{|\mathbf{u} \times \mathbf{B}|} \sim \frac{\overline{\mathbf{P}}_e/Lne}{v_{th,i}B} \sim \frac{nT_i/Lne}{v_{th,i}B} \sim \frac{m_i v_{th,i}^2/Le}{v_{th,i}B} \sim \frac{\rho_i}{L} \tag{1.42}$$

where we used that $u_\perp \sim v_{th,i}$, the ion thermal velocity; that $\overline{\mathbf{P}}_e \sim \overline{\mathbf{P}}_i$ and we suppose that $\overline{\mathbf{P}}_e \sim nT_i$; that $\rho_i = \frac{v_{th,i}}{\Omega_{c,i}}$. In MHD model, where Ł $\gg \rho_i$, the 'ideal' term is much greater than the thermoelectric one.
The ratio between the Hall term and the pressure term is:

$$\frac{|\nabla \cdot \overline{\mathbf{P}}|/ne}{|\mathbf{J} \times \mathbf{B}|/ne} \sim \frac{P}{B^2/\mu_0} \sim \beta \tag{1.43}$$

where we used Ampère law. β is defined as the ratio between the kinetic pressure and the magnetic pressure. Then, also the Hall term in negligible compared to the 'ideal' term if the characteristic length of the process L is much greater than ρ_i.
An important remark is that the characteristic scale connected to the process of decoupling from the magnetic field is usually the ion (or electron) inertial length $d_{i,e} = c/\omega_{p,i,e}$ and $d_{i,e} \geq \rho_{i,e}$. Since $\frac{\rho_i}{d_i} = \sqrt{\beta}$ (the same for electrons) and $\beta \sim 1$ in the plasma and field conditions analysed in this study, we use $\rho_{i,e}$ as characteristic length without forgetting the role of $d_{i,e}$.
Now, if we consider the inertia term, we have that

$$\frac{m_e}{ne^2}\nabla \cdot (\mathbf{Ju}) \sim \frac{m_e}{ne^2}\nabla \cdot (\mathbf{uJ}) \sim \frac{m_e}{ne}\frac{\partial \mathbf{J}}{\partial t} \tag{1.44}$$

then it is sufficient to evaluate

$$\frac{\frac{m_e}{ne^2}|\nabla \cdot (\mathbf{Ju})|}{|\mathbf{u} \times \mathbf{B}|} \sim \frac{\frac{m_e}{ne^2}\frac{v_{th,i}}{L}\frac{|\nabla \cdot \overline{\mathbf{P}}|}{B}}{|\mathbf{u} \times \mathbf{B}|} \tag{1.45}$$

Using Eq. 1.42,

$$\frac{m_e}{e}\frac{v_{th,i}}{L}\frac{\rho_i}{B} \sim \frac{m_e}{m_i}\left(\frac{\rho_i}{L}\right)^2 \ll 1. \tag{1.46}$$

We see that if the scale of the system is much greater than ρ_i all the terms are negligible compared to the ideal one, $\mathbf{u} \times \mathbf{B}$, as expected.
An ordering between the terms emerges from this computation: we seen that the Hall term

becomes not negligible when $L \sim \rho_i$ while we need to go at even smaller scales to have a not negligible contribution of the pressure term and especially of the inertia term, which can be important only for $L \sim \rho_e$. This is clearer if we assume that $T_i \sim T_e$. From Eq. 1.46 we obtain that the inertia term is $\sim \frac{\rho_e^2}{T_e}\frac{T_i}{\rho_i^2}\left(\frac{\rho_i}{L}\right)^2 \sim \left(\frac{\rho_e}{L}\right)^2$.

Furthermore, we notice that when $L \sim \rho_i$ ion are decoupling while electron are still frozen to the field. Indeed, in this condition we have to consider the following generalised Ohm's law:

$$\mathbf{E} + \mathbf{u} \times \mathbf{B} = \frac{1}{ne}\mathbf{J} \times \mathbf{B} \tag{1.47}$$

in other words, we add only the Hall term since the others are negligible at this length scale. From Eq. 1.9 and 1.10 we have:

$$\mathbf{E} = -\mathbf{v}_e \times \mathbf{B} \tag{1.48}$$

which is the Ohm's law in the ideal MHD model written for electrons. Since the frozen-in conditions still holds for electrons, a strong current (and an electric field) is generated. It gives place to a magnetic field that assumes a typical quadrupolar shape, as can be seen in the sketch of figure 1.4

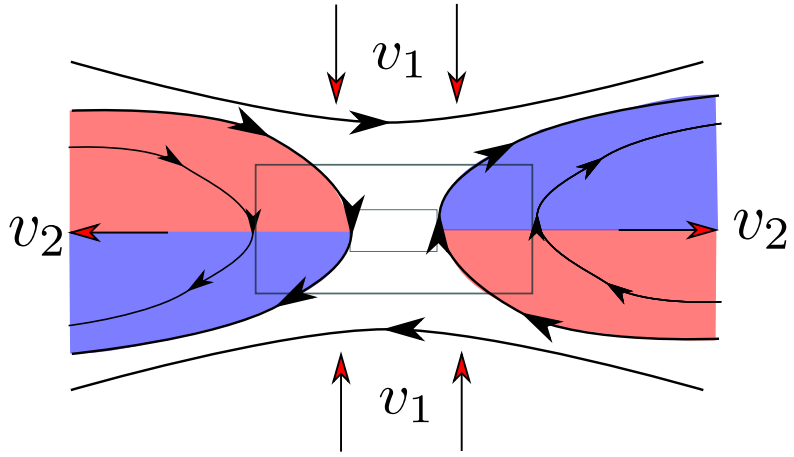

FIGURE 1.4: A sketch of the anti-parallel magnetic reconnection. The bigger rectangle represent the ion diffusion region (IDR), the smaller one represent the electron diffusion region (EDR). In the IDR the ion are decoupled from the magnetic field while the frozen-in condition is still valid for electrons. The consequence is the presence of a Hall electric and magnetic field. Here we show only the magnetic one: blue indicates a region of $B_{Hall} > 0$, red indicates a region of $B_{Hall} < 0$.

1.4 Signatures of magnetic reconnection

This small section is meant to summarize some of the features and consequences of the magnetic reconnection process. One signature of magnetic reconnection is the presence of a normal (to the initial $\mathbf{B}$) component of the magnetic field: if a $B_n \neq 0$ exists, then the field has been modified and reconnection is likely to be occurred. It is worth remembering that we are considering 2D

reconnection and that the initial magnetic field is directed along a direction, let us call it x. The presence of reconnection leads the magnetic field have also a component along y, always lying in the same plane.
Another sign is the the presence of *jets*, particle acceleration. Magnetic reconnection leads the magnetic field to reach a state of lower energy: it is a process of energy conversion that causes particles acceleration and heating. It can be considered as a dissipative process: in this sense one of the reconnection signatures is the presence of a relatively high value of dissipate power $\mathbf{J} \cdot \mathbf{E}$ in the region corresponding to the reconnection site.

Therefore, at the end of this chapter, we are able to indicate some of the feature that should be observed while looking at a reconnection event: non-zero parallel electric field at the X-line, non-zero component of the magnetic field perpendicular to the current sheet (in the reconnection plane), reconnection jets and plasma heating.

1.5 Near Earth's space plasma

Plasma in near-Earth space is composed mainly by electrons and protons (there are also α particles, but they represent $\sim 5\%$ of the total density). The particle density is of the order of $\sim 1 - 10\ cm^{-3}$ [4] As a result, collisions between particles are usually negligible, and the plasma can be considered collisionless.

Although magnetic reconnection can be individuated in a bunch of different situation in space plasmas, we are interested in reconnection processes driven by the interaction between the solar wind and the magnetosphere. Figure 1.5 gives a schematic representation of the system we are looking at.

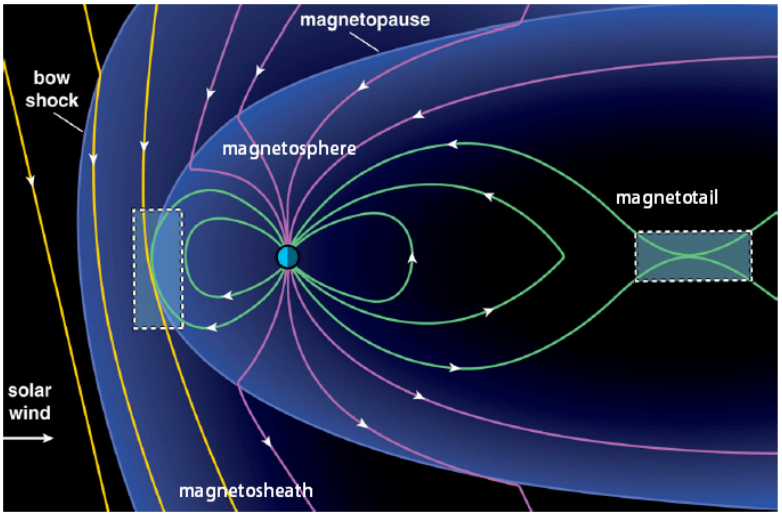

FIGURE 1.5: The near-Earth space, the Sun is on the left. Adapted from [12]

[4] We do not specify whether the *particle density* is the electron or the ion density. In fact, deviations from charge neutrality $n_e \neq n_i$ occur only on spatial scales of order λ_D, the Debye length. Since most plasmas of interest in the present context are sufficiently dense, such that λ_D is small and ω_{pe}^{-1} is short compared to all other spatial and time scales, we have $(n_i - n_e)/n_e \ll 1$, so that we can set $n_e = n_i = n$.

The solar wind is composed by the solar magnetic field (with its peculiar conformation caused by the rotational motion of the sun) and by the particles of the plasma with typical velocities of $\sim 40km/s$ for protons and $\sim 350 - 400km/s$ for electrons. Since the solar wind is a ultrasonic and ultralfvenic plasma, the interaction between it and the Earth environment gives rise to a *bow shock*. The result is the presence of a region between the external space and the magnetosphere, the *magnetosheath* characterised by turbulence, by increment in density and temperature and where the plasma becomes subsonic.
The next region, going Earthward, is the *magnetosphere*, separated from the *magnetosheath* by the *magnetopause*. The *magnetopause* is a layer characterised by strong currents due to the spatial variation of the magnetic field from the *magnetosheath* to the *magnetosphere*. Being its thickness in general negligible compared to the other regions, it's usually modelised as a 2D layer.

In the subsolar magnetosphere region, the typical configuration is characterised by a southward directed interplanetary magnetic field advected by the solar wind and a northward directed magnetospheric magnetic field. This condition leads to magnetic reconnection. Once reconnected, field lines are pulled over the polar caps, enter the magnetotail, and reconnecte once more across the tail current sheet (magnetic reconnection of the magnetotail), setting up a global plasma dynamics. Furthermore, magnetic reconnection is crucial for magnetosphere dynamics. Particles are able to reach regions that were inaccessible before leading to momentum, energy and mass transport. This as been directly seen, [26]. In addiction, even if it is likely to occur in the subpolar region, the position of the *X point* resulting from the reconnection event can largely vary depending on the conditions of the interplanetary magnetic field (IMF). In the periods when the IMF is directed northward, reconnection can not occur on the dayside regions of magnetoshere. In these conditions, for example, it is possible to have magnetic reconnection near to the polar cusps.

Chapter 2

Methods of data analysis

To study structures, such as current sheets, flux ropes, or fully three-dimensional configurations, it is desirable to examine them in their proper co-moving frame, in which they appear as time stationary as the data permit. Our aim is also to determine their physical dimensions, so we have to establish the frame velocity. In order to find this frame and its velocity several methods have been developed. In this chapter, we give a description of methods that will be used in the data analysis. In section 2.1.1 we describe the Minimum Variance Analysis method, a single spacecraft method used in order to find a coordinate frame composed by a vector normal to the studied structure and the other two vectors of the set directed tangentially to the structure. In this work, the Minimum Variance method is applied to the magnetic field. Section 2.1.1.2 is then devoted to the definition of errors to apply to the directions found with the MVA method. Section 2.1.2 deals with the *deHoffmann-Teller* method. It is a single spacecraft method meant to determine the velocity of the analysed structure. Definition of the deHoffmann-Teller velocity's error and analysis of velocity's stability over time is then shown in section 2.1.2.1. The last adopted method is the timing method, explained in section 2.1.3. It differs from the others because it is a multi-spacecraft method. It allows to get the direction of the normal to the structure and also the structure's velocity along the normal direction. The reference for the first part of the chapter is [25]. In particular, chap.8 and chap.11 for the Minimum Variance Analysis, chap.9 for the *deHoffmann-Teller* method and chap.12 and 13 for the timing method.
The last part of the chapter addresses the problem of the current computation giving a description of the *curlometer* technique. It deals with a multi-spacecraft technique that allows to compute the electric current density at the barycentre of a tetrahedron by using four-point magnetic field measurements.

2.1 Finding the proper frame

2.1.1 Minimum Variance Analysis

The Minimum Variance Analysis (MVA) method is used to individuate the normal direction to a transition layer (in our case, a current sheet) that can be considered as a surface, i.e a

layer where the thickness is negligible if compared to the other characteristic scale lengths. The method relies on the magnetic field vector measured by a spacecraft crossing the transition layer. In principle, a single spacecraft is sufficient to obtain the desired unit vector $\hat{n}$; on the other hand when more than one spacecraft (four in the MMS mission) measure the magnetic field vector we have the possibility to improve the result and, in particular, to have information about the stationarity of the current sheet.
The main assumption imposed by this method is that along the two directions tangent to the surface layer (x and y), there are no variations. Since $\nabla \cdot \mathbf{B} = 0$ holds, we get $\frac{\partial B_z}{\partial z} = 0$.
Furthermore, from the initial hypothesis $\frac{\partial}{\partial x}, \frac{\partial}{\partial y} = 0$ we get from Faraday's law that B_z is also constant in time. We are then looking for the unit vector $\hat{n}$, whose direction, according to our reference frame, is directed along the z axis, $\hat{n} = \hat{z}$. Note that the variance of the field B is the smallest along this direction.
To obtain the unit vector $\hat{n}$ three values of the magnetic field are needed: two values, $\mathbf{B_1}$ and $\mathbf{B_3}$, are taken at opposite sides respect to the layer; the last one, $\mathbf{B_2}$, in the proximity of the layer. Generally, the presence of a current layer can be easily individuated from the fact that the three component of the magnetic field change sign. Using Faraday's law, we get that this inversion leads to a current. Therefore, the problem is not the individuation of the current sheet but the understanding of its orientation in space. Since B_n has to be constant and uniform the n component of the three measured fields has to be constant.

$$\mathbf{B_1} \cdot \hat{\mathbf{n}} = \mathbf{B_2} \cdot \hat{\mathbf{n}} = \mathbf{B_3} \cdot \hat{\mathbf{n}} \quad \rightarrow \quad \hat{\mathbf{n}} \cdot (\mathbf{B_1} - \mathbf{B_2}) = \hat{\mathbf{n}} \cdot (\mathbf{B_2} - \mathbf{B_3}) = 0 \tag{2.1}$$

This means that both $(\mathbf{B_1} - \mathbf{B_2})$ and $(\mathbf{B_2} - \mathbf{B_3})$ are orthogonal to $\hat{n}$. This leads to the definition of $\hat{\mathbf{n}}$ in terms of $\mathbf{B_1}, \mathbf{B_2}, \mathbf{B_3}$:

$$\hat{\mathbf{n}} = \pm \frac{(\mathbf{B_1} - \mathbf{B_2}) \times (\mathbf{B_2} - \mathbf{B_3})}{|(\mathbf{B_1} - \mathbf{B_2}) \times (\mathbf{B_2} - \mathbf{B_3})|} \tag{2.2}$$

It is clear from this definition that the two vectors of the measured magnetic field have *not* to be parallel. Selecting values from the two different side of the layer should avoid this problem in the majority of the cases.

2.1.1.1 Minimum Variance Analysis on Magnetic Field

Even if with the previous consideration we do are able to obtain a normal direction to the layer, the result is not so reliable since we used only three measures of $\mathbf{B}$. The next step is to obtain $\hat{\mathbf{n}}$ in a different way. We know that the variations of $\mathbf{B}$ are the smallest along the normal direction and that $\hat{\mathbf{n}}$ is a unit vector ($|\hat{\mathbf{n}}|^2 = 1$). Let us assume that we have M measured values of the magnetic field. We define the quantity that we want to minimize as:

$$\frac{1}{M} \sum_{m=1}^{M} |(\mathbf{B_m} - \langle \mathbf{B} \rangle) \cdot \hat{\mathbf{n}}|^2 \tag{2.3}$$

where $\langle \mathbf{B} \rangle$ is the average of the magnetic field on the M measures. We can find the minimum of 2.3 using the method of Lagrange multipliers.

$$\frac{\partial}{\partial n_i} \left[\frac{1}{M} \sum_{m=1}^{M} |(\mathbf{B_m} - \langle \mathbf{B} \rangle) \cdot \hat{\mathbf{n}}|^2 - \lambda(|\hat{\mathbf{n}}|^2 - 1) \right] = 0 \tag{2.4}$$

where $i = x, y, z$. After calculations, we reduce the problem to an eigenvalue problem:

$$\mathcal{M}\ \hat{\mathbf{n}} = \lambda\ \hat{\mathbf{n}} \quad \text{where} \quad \mathcal{M}_{ij} = \langle \mathbf{B_i B_j} \rangle - \langle \mathbf{B_i} \rangle \langle \mathbf{B_j} \rangle \tag{2.5}$$

To solve the problem we must find the eigenvalues $(\lambda_1, \lambda_2, \lambda_3)$ and the corresponding eigenvectors $(\mathbf{v}_1, \mathbf{v}_2, \mathbf{v}_3)$ of the matrix $\mathcal{M}$. In the following the relation $\lambda_3 < \lambda_2 < \lambda_1$ holds, so that λ_2 is always the intermediate eigenvalue.
Since the matrix is symmetric all the eigenvalues will be real. The best ordering corresponds to $\lambda_3 \ll \lambda_2 \ll \lambda_1$: we are able to identify a direction of maximal, intermediate and minimal variance. When the three eigenvalues of the variance matrix are distinct, the matrix is said to be *non-degenerate*. In this case, being λ_3 the smallest eigenvalue, $\mathbf{v}_3$ will be the eigenvector of the minimum variance. Its direction individuate the normal direction to the transition layer, *i.e* $\hat{\mathbf{n}}$. Moreover, the corresponding λ_i values represent the variances in those field components. In fact, if $\mathcal{M}$ is written in the eigenvectors' set, it becomes a diagonal matrix. The elements on the diagonal are $\mathcal{M}_{ii} = \langle \mathbf{B_i B_i} \rangle - \langle \mathbf{B_i} \rangle \langle \mathbf{B_i} \rangle = \langle \mathbf{B_i}^2 \rangle - \langle \mathbf{B_i} \rangle^2$ and this is the definition of the variance of the $i-th$ component of the $\mathbf{B}$ field. All the λ_i values are therefore non-negative.

The optimal ordering of the three eigenvalues is not always found. Nevertheless, in order to find $\hat{\mathbf{n}}$ it is sufficient to have a λ_i really small compared to the other eigenvalues. The matrix is said *degenerated* when two of the eigenvalues are of the same order. If $\lambda_3 \simeq \lambda_2$ it is not possible to identify the minimum variance direction. In this case, provided that $\lambda_1 \gg \lambda_2 \simeq \lambda_3$, we can still infer that the eigenvector corresponding to λ_1 is tangential to the current sheet. Lastly, if $\lambda_3 \simeq \lambda_2 \simeq \lambda_1$ we have no information about the orientation of the current sheet. Empirically, for a relatively small set of data ($M < 50$) , if $\frac{\lambda_2}{\lambda_3} > 10$, $\hat{\mathbf{n}}$ is well defined (often, also $\frac{\lambda_2}{\lambda_3} > 5$ is accepted as well).

Other types of MVA have been developed. For example, if we are looking for a tangential discontinuity we have $\langle \mathbf{B} \rangle \cdot \hat{\mathbf{n}} = 0$ and the quantity to be minimized is $\frac{1}{M} \sum_{m=1}^{M} |(\mathbf{B_m}) \cdot \hat{\mathbf{n}}|^2$. The results of the different methods are coherent and similar if the $\mathbf{B}$ has actually a component long $\hat{\mathbf{n}}$ which is near to zero. Otherwise, the MVA calculation proposed here is the most appropriate.

2.1.1.2 Error Estimates

At this point, we need to give an adequate error to the normal direction. In the case the incertitude has a statistical nature we can obtain an analytical formulation for the errors. Note that we have also to deal with possible systematic errors due to the finite sampling or stationarity noise of the $\mathbf{B}$ signal. In addition, source of errors can be the lack of stationarity or quasi-one-dimensionality of the structure being studied: this can be addressed with a *nested analysis* of

the normal direction. This analysis is widely explained in the section 2.1.2.1 since it is a general method that can be used with different quantities. It is functional to address to this kind of problem, in particular to check if the hypothesis of stationarity is reliable.

In order to give an appropriate error to the normal direction, we start doing some hypothesis on the field $\mathbf{B}$. First, we suppose that there are not systematic errors. Then, let us assume that $\Delta\mathbf{B}$ - the error of $\mathbf{B}$ - is a noise component that is stationary, isotropic, and spatially uncorrelated. This properties are listed below:

$$\langle \Delta\mathbf{B}_i^m \rangle = 0 \tag{2.6}$$

$$\langle \Delta\mathbf{B}_i^m \ \Delta\mathbf{B}_j^n \rangle = \delta_{ij}\delta_{nm} \ \langle (\Delta\mathbf{B}_3^m)^2 \rangle \tag{2.7}$$

$$\langle \Delta\mathbf{B}_i^m \ \Delta\mathbf{B}_j^n \ \Delta\mathbf{B}_k^l \rangle = 0 \tag{2.8}$$

where $i = 1, 2, 3$ (similarly j and k) indicates the cartesian component and $m = 1, 2 \dots M$ (similarly n and l) indicates the set of measures. The average $\langle\ \rangle$ indicates the *ensemble* [1] mean done on the sets of measures. The first property means that that $\Delta\mathbf{B}$ has a effectively a noise feature. The second property indicates that the variance of each of the three vector components of the noise has been assumed to be the same (isotropy) and that it is represented by the variance of the component along $\mathbf{v}_3$. From the hypothesis of stationarity we can also say that $\Delta\mathbf{B}_3^m$ is not time dependent.

At this point, we write the eigenvalues equation Eq. 2.5 in a perturbative way to the first order: every quantity a can be written as $a = a^\star + \Delta a$ where Δa is the noise component.

$$(\mathcal{M}^\star + \Delta\mathcal{M}) \ (\mathbf{v}_i^\star + \Delta\mathbf{v}_i) = (\lambda_i^\star + \Delta\lambda_i) \ (\mathbf{v}_i^\star + \Delta\mathbf{v}_i) \tag{2.9}$$

with $i = 1, 2, 3$ indicating the three elements of the set of eigenvectors. Taking only the first order terms and projecting Eq. 2.9 along $\mathbf{v}_j$ we obtain:

$$(\lambda_j^\star - \lambda_i^\star) \ (\Delta\mathbf{v}_i)_j = -\Delta\lambda_i\delta_{ij} - \Delta\mathcal{M}_{ij} \tag{2.10}$$

Since $\mathcal{M}$ and $\mathcal{M}^\star$ are symmetric, so is $\Delta\mathcal{M}$. We can infer that $\Delta\mathbf{v}_{ij} = -\Delta\mathbf{v}_{ji}$ and this is coherent with the request of orthogonality between the perturbed eigenvectors.

We obtain:

$$\Delta\mathbf{v}_{ij} = \frac{-\Delta\mathcal{M}_{ij}}{\lambda_j^\star - \lambda_i^\star} \qquad i \neq j \tag{2.11}$$

$$\Delta\mathbf{v}_{ii} = \mathbf{v}_i^\star \cdot \Delta\mathbf{v}_i = 0 \qquad i = j \tag{2.12}$$

[1] By ensemble average we mean the average over a large number of realisations of the noise component of the measured field. In reality, only one such realisation is available to us, namely the one contained in the measured set of vectors $\mathbf{B}^m$. The mean will be done on the number of magnetic field vectors in the set.

Note that having $\lambda_j^\star \simeq \lambda_i^\star$ leads to a great increase on the eigenvectors uncertainties. Furthermore, in the linear approximation, we can give a simple geometric interpretation to $\Delta\mathbf{v}_{ij}$: it represents the angular deviation from the unperturbed eigenvector $\mathbf{v}_i^\star$ towards the direction of the eigenvector $\mathbf{v}_j^\star$.
Now we want to compute $\langle(\Delta\mathbf{v}_{ij})^2\rangle$. To do that we have to express $\Delta\mathcal{M}$ in terms of $\Delta\mathbf{B}$.
It can be shown (see [25]) that $\Delta\mathbf{B}_3 = \lambda_3\ M/(M-1)$ where M is the number of measures. Having in mind the definition of $\mathcal{M}$ from Eq. 2.5 and the properties of $\Delta\mathbf{B}$, we obtain

$$\langle(\Delta\mathcal{M}_{ij})^2\rangle = \langle\lambda_3\rangle\ (\langle\lambda_j\rangle + \langle\lambda_i\rangle - \langle\lambda_3\rangle)\frac{(1+\delta_{ij})}{M-1} \tag{2.13}$$

So [2],

$$\langle(\Delta\mathbf{v}_{ij})^2\rangle = \langle\lambda_3\rangle\ \frac{(\langle\lambda_j\rangle + \langle\lambda_i\rangle - \langle\lambda_3\rangle)}{(\lambda_j-\lambda_i)^2}\frac{(1-\delta_{ij})}{M-1} \tag{2.14}$$

This is the expression of the square of the error of the eigenvector directions. Due to the geometric interpretation previously underlined we will indicate $\sqrt{\langle(\Delta\mathbf{v}_{ij})^2\rangle}$ as $\Delta\phi_{ij}$.

2.1.2 deHoffmann-Teller Analysis

The so-called deHoffmann-Teller Analysis consists in looking for an inertial frame where the electric field is zero (empirically, quasi-zero). Since we usually use the non-relativistic approximation, the sought frame is a Galilean frame and the transformation law is:

$$\mathbf{E}' = \mathbf{E} + \mathbf{v}\times\mathbf{B} \tag{2.15}$$

where $\mathbf{v}$ is the relative velocity between the two considered frames.
If $\mathbf{E}$ is the field in the spacecraft frame (where the measure take place), then the deHoffmann-Teller velocity $\mathbf{V}_{HT}$ is defined as follows:

$$\mathbf{E}' = \mathbf{E} + \mathbf{V}_{HT}\times\mathbf{B} = 0 \tag{2.16}$$

It is worth remarking that electric field measurements are not always available with sufficiently high precision. If the direct measure of $\mathbf{E}$ is not reliable, we suppose that the data are taken in regions across the layer where the ideal MHD is valid so that $\mathbf{E} \simeq -\mathbf{v}\times\mathbf{B}$. In this way, the measured values of $\mathbf{v}$ and $\mathbf{B}$ will be the proxy for the electric field. The knowledge of the HT frame is useful because we can obtain some information about the discontinuity's frame.

If $\mathbf{v}_m$ is a generic measured value of plasma velocity in the spacecraft frame, $\mathbf{v'}_m = \mathbf{v}_m - \mathbf{V}_{HT}$ is the plasma velocity in the HT frame. Assuming that the electric field is strictly zero in HT frame, $\mathbf{v}_m \times \mathbf{B}_m = \mathbf{V}_{HT}\times\mathbf{B}_m$. This means that $\mathbf{v'}_m$ has the same direction of $\mathbf{B}_m$. So, an

[2] Note that another approximation is done:$\langle\lambda_j\rangle$ is replaced by λ_j in the error estimates, we do not take into count $\Delta\lambda_j$

important feature of the HT frame is that plasma velocity and magnetic field are aligned in both the sides of the layer. Another characteristic is that the particle's energy is only kinetic since $\mathbf{E} = 0$.
In addiction, if we are in presence of a discontinuity and we are able to know the normal direction $\hat{\mathbf{n}}$ to it, the determination of $\mathbf{V}_{HT}$ allows to compute the normal component of the discontinuity's velocity. In fact, we can always write

$$\mathbf{V}_{sat}^{HT} = \mathbf{V}_{dis}^{HT} + \mathbf{V}_{sat}^{dis} \tag{2.17}$$

where $\mathbf{V}_{sat}^{dis}$ is the discontinuity velocity in the satellite's frame, the others are similarly defined. Since for construction $\mathbf{V}_{dis}^{HT} \cdot \hat{\mathbf{n}} = 0$, we obtain

$$\mathbf{V}_{sat}^{HT} \cdot \hat{\mathbf{n}} = \mathbf{V}_{sat}^{dis} \cdot \hat{\mathbf{n}}. \tag{2.18}$$

Knowing the direction normal to the discontinuity and the velocity of the *deHoffmann-Teller* velocity allows to get the normal component of the discontinuity velocity in the spacecraft frame. This is useful also to get the characteristic length of the discontinuity layer.
In order to find $\mathbf{V}_{HT}$, we minimize the quantity:

$$D(\mathbf{V}_{HT}) = \frac{1}{M}\sum_{m=1}^{M} |\mathbf{E'}_m|^2 = \frac{1}{M}\sum_{m=1}^{M} |\mathbf{E}_m + \mathbf{V}_{HT} \times \mathbf{B}_m|^2 = \frac{1}{M}\sum_{m=1}^{M} |(\mathbf{v}_m - \mathbf{V}_{HT}) \times \mathbf{B}_m|^2 \tag{2.19}$$

By calculating $\frac{\partial D(\mathbf{V}_{HT})}{\partial \mathbf{V}_{HT,i}} = 0$ for $i = 1, 2, 3$ we find:

$$\langle \mathcal{K}_m \rangle \mathbf{V}_{HT} = \langle \mathcal{K}_m \mathbf{v}_m \rangle \qquad \text{where} \qquad \mathcal{K}_{m,ij} = \mathbf{B}_m^2 \left(\delta_{ij} - \frac{\mathbf{B}_{m,i}\mathbf{B}_{m,j}}{\mathbf{B}_m^2} \right) \tag{2.20}$$

If the matrix $\langle \mathcal{K}_m \rangle$ is not singular, $\mathbf{V}_{HT}$ can be written as follows:

$$\mathbf{V}_{HT} = \langle \mathcal{K}_m \rangle^{-1} \langle \mathcal{K}_m \mathbf{v}_m \rangle \tag{2.21}$$

To quantify the goodness of the found HT frame two parameters are often used:

- The correlation coefficient c. It is defined

$$c = \frac{\sum_{i=x,y,z}\sum_{m=1}^{M}(x_i^m - \bar{x})(y_i^m - \bar{y})}{\sqrt{\sum_{i=x,y,z}\sum_{m=1}^{M}(x_i^m - \bar{x})^2}\sqrt{\sum_{i=x,y,z}\sum_{m=1}^{M}(y_i^m - \bar{y})^2}} \tag{2.22}$$

  and it quantifies the strength of the linear association between the variables $\mathbf{x}$ and $\mathbf{y}$ (in our case $\mathbf{E}$ and $\mathbf{E}_{HT}$, with $\mathbf{E}_m = -\mathbf{v}_m \times \mathbf{B}_m$ and $\mathbf{E}_{m,HT} = -\mathbf{V}_{HT} \times \mathbf{B}_m$). If $c = 1$ the positive correlation is maximal.

- The ratio d. It is defined

$$d = \sqrt{\frac{D(\mathbf{V}_{HT})}{D(0)}} \tag{2.23}$$

and to have a good HT frame d has to be $d \ll 1$.

It can be demonstrated that $c^2 + d^2 = 1$.

2.1.2.1 $\mathbf{V}_{HT}$'s error and stability

In this section we look for a method to assign an error to $\mathbf{V}_{HT}$ and to understand whether $\mathbf{V}_{HT}$ is constant in time.
Concerning our first aim, we assume that the incertitude on $\mathbf{V}_{HT}$ is due to some kind of random fluctuation, a stationary noise statistically independent from the data series. We assume that this noise has for *only* source the residual field $\mathbf{E'}_m = (\mathbf{v}_m - \mathbf{V}_{HT}) \times \mathbf{B}_m$. Moreover, it has an isotropic probability distribution in the plane normal to $\mathbf{B}_m$ and two values of $\mathbf{E'}_m$ that are separated in time or space have no correlation. This assumptions are not justified but they allow to achieve an analytical and quite simple calculation of the $\mathbf{V}_{HT}$ incertitude.

We want to calculate $\langle\langle \Delta\mathbf{V}_{HT,i}\ \Delta\mathbf{V}_{HT,j}\rangle\rangle$ $(i,j = 1,2,3)$, supposing that the only source of noise is $\mathbf{E'}_m$. From Eq. 2.21 we deduce

$$\Delta\mathbf{V}_{HT} = \langle\mathcal{K}_m\rangle^{-1}(\Delta\mathbf{E}_m \times \mathbf{B}_m) \qquad \text{with} \qquad \Delta\mathbf{E}_m = \mathbf{E'}_m \tag{2.24}$$

After some calculation [3], we find that

$$\langle\langle \Delta\mathbf{V}_{HT,i}\ \Delta\mathbf{V}_{HT,j}\rangle\rangle = \langle\mathcal{K}_m\rangle^{-1}_{ij}\ \frac{D(\mathbf{V}_{HT})}{2M-3} \tag{2.25}$$

For any chosen spatial direction, specified by a unit vector $\hat{\mathbf{k}}$, the variance of the velocity component $\mathbf{V}_{HT} \cdot \hat{\mathbf{k}}$ is

$$\sigma^2 = \hat{k}_i \langle\langle \Delta\mathbf{V}_{HT,i}\ \Delta\mathbf{V}_{HT,j}\rangle\rangle \hat{k}_j \tag{2.26}$$

The eigenvectors of the variance matrix $\langle\langle \Delta\mathbf{V}_{HT,i}\ \Delta\mathbf{V}_{HT,j}\rangle\rangle$ are the same as those of $\langle\mathcal{K}_m\rangle^{-1}$ (called λ_i in the following), and the respective eigenvalues are

$$\Lambda_i = \frac{1}{\lambda_i}\frac{D(\mathbf{V}_{HT})}{2M-3}. \tag{2.27}$$

The eigenvalues Λ_i are the variances of the components of $\mathbf{V}_{HT}$ long the eigenvectors of the variance matrix.

Another level of analysis is represented by the study of the stationarity of $\mathbf{V}_{HT}$. This can be done through a *nested analysis*. This method allows on one side to check the time-evolution of $\mathbf{V}_{HT}$ and on the other to individuate an optimal time interval for the analysis of the event. During a *nested analysis*, a set of nested segment of data are centred in the event (*e.g.* the centre of a current sheet); at every step a bigger segment is considered and the $\mathbf{V}_{HT}$ is calculated. The first step consists of taking 3 data (the first corresponding to the center of the event, the others

[3] Computation is detailed in [25], chap. 9

one on each side) and calculating $\mathbf{V}_{HT}$. In all the following steps, the time segment is augmented by adding a measure on each side of the event, and each time $\mathbf{V}_{HT}$ is calculated.
If the sought velocity is strictly time stationary, then the results from all the different nested segments should be the same. In reality, a group of the shortest and longest segments often gives results that are significantly different from those obtained for "medium" segments. Within the intermediate range, the results of $\mathbf{V}_{HT}$ should be the same, or nearly the same, regardless of segment duration. In other words, plotting $\mathbf{V}_{HT}$ in function of the number of measures M (proportional to the segment duration because $T = (M-1)\tau$, being τ the duration of the sampling) should show a *plateau* region for intermediate values of M. The longer and the flatter the *plateau* is, the more stationary is $\mathbf{V}_{HT}$.

As said before, the shortest and the longest segments in the *nested analysis* often give results that different from the intermediate region. For the longest segments, this is normally due to the presence of magnetic structures, different from the event we are focusing on, that begin to be inserted in the considered interval of time. For the shortest segments, these differences can be caused by low scale structures that the current layer may present.
The *nestes analysis*, used in this section to control the stability of $\mathbf{V}_{HT}$, can be an useful tool also for other parameters, for example it can be applied to the direction of the normal to the current layer.

2.1.3 Multispacecraft methods

The determination of the de Hoffmann-Teller velocity and of the normal direction to the current sheet can be done, in principle, with measurements from a single spacecraft. The difficulty is then to verify the result. The quality of these estimations can be affected by the detailed microstructure of the sampled discontinuity. For example, the presence of waves on the surface of the discontinuity as well as the natural noise can modify the results and invalidate the assumptions of a simple model for the boundary. Often, the sampling or the low-pass filtered apply to the data can limit these effects. But the good sampling can be also totally fortuitous and it is difficult to be conscious of that using a single spacecraft method. Except for special situations, no check on consistency is available for a single spacecraft. In addiction, with a single spacecraft it is hard to determine whether a structure that is observed for a short time (for example, during a magnetopause crossing) is due to an extended and rather steady layer, or a short burst of activity limited in both space and time.

The presence of a constellation of spacecraft can reply to the necessity to have consistency check and gives also the possibility to have a bigger conscience on what the data are showing. (In the case of Cluster and MMS missions we have four satellites and so four different "points of view").
Even in the case of multispacecraft analysis, some general assumptions are made. Some of them as been already pointed out in the previous sections but we will summarise them here in order to have a complete vision of the usual hypotheses.
The first assumption, made to compute the MVA, is planarity. We suppose that the current layer is a 1D structure so that we can infer, from the solenoidality of $\mathbf{B}$, that $\frac{\partial B_n}{\partial x_n} = 0$. The second general hypothesis is stationarity. It can be verified with a *nested* analysis or a *timing*

analysis. As a third assumption, the boundary is generally consider as moving with constant velocity. Another important hypothesis is about the space scale: it is assumed that the event scale length is much larger than the spacecrafts separation distances.
It is worth to underline that non-colinear normals between the different spacecraft can of course be due to the curvature of the boundary but, in fact, the difficulty in the interpretation of the resulting normals is often caused by the combined effect of non-constant motion and curvature.

2.1.3.1 Timing analysis

While the methods discussed above are single spacecraft analysis (in the sense that a single spacecraft can perform them, then the presence of more than one spacecraft doing the same measure gives a more precise result), the *timing* is defined only when a constellation of spacecrafts is present. If all the assumptions presented in the previous section hold, we can imagine the current sheet as a plane layer crossing the spacecraft constellation with a constant velocity. The discontinuity is supposed to be plane in a length scale of the order of the separation between the spacecrafts and its motion to be uniform during the time of the constellation crossing.
In this way, we are able to determine the component of the discontinuity's velocity along its normal and the normal's direction. If t_α is the time when the spacecraft α observes the discontinuity, and if $\mathbf{r}_\alpha$ is the spacecraft position we can say:

$$(\mathbf{r}_\alpha - \mathbf{r}_4) \cdot \hat{\mathbf{n}} = V_{CS}\ (t_\alpha - t_4) \tag{2.28}$$

where spacecraft 4 has been arbitrary chosen as the reference and $\alpha = 1, 2, 3$; V_{CS} is the velocity of the current sheet. The times t_α are assumed to be all well defined. Said

$$\mathbf{m} = \frac{\hat{\mathbf{n}}}{V_{CS}} \tag{2.29}$$

we see that the linear system to be solved is

$$\begin{pmatrix} \mathbf{r}_{14} \\ \mathbf{r}_{24} \\ \mathbf{r}_{34} \end{pmatrix} \mathbf{m} = \begin{pmatrix} t_{14} \\ t_{24} \\ t_{34} \end{pmatrix} \tag{2.30}$$

More explicitly,

$$\begin{pmatrix} r_{14,x} & r_{14,y} & r_{14,z} \\ r_{24,x} & r_{24,y} & r_{24,z} \\ r_{34,x} & r_{34,y} & r_{34,z} \end{pmatrix} \begin{pmatrix} m_x \\ m_y \\ m_z \end{pmatrix} = \begin{pmatrix} t_{14} \\ t_{24} \\ t_{34} \end{pmatrix} \tag{2.31}$$

In order to solve this system the matrix containing all the positions (called $\mathcal{D}$ in the following) has to be non-singular: this condition is satisfied if and only if the four spacecraft are not coplanar. In general, the events can not always be identified unambiguously on each spacecraft. In this

cases, we can still determine time delays of the observations made by one spacecraft with respect to those done by the others. This can be done, for example, by calculating the cross correlation of the data from the different spacecraft but also by inspection (taking necessary precautions). To determine the best direction of the normal $\hat{\mathbf{n}}$ we can minimize the quantity S:

$$S = \sum_{\alpha=1}^{N} \sum_{\beta=1}^{N} [(\mathbf{r}_\alpha - \mathbf{r}_\beta) \cdot \hat{\mathbf{n}} - V_{CS}(t_\alpha - t_\beta)]^2 \tag{2.32}$$

If we divide both sides with V_{CS} we the sought vector $\mathbf{m}$ appears and we have a new quantity to minimize:

$$S' = \sum_{\alpha=1}^{N} \sum_{\beta=1}^{N} [(\mathbf{r}_\alpha - \mathbf{r}_\beta) \cdot \mathbf{m} - (t_\alpha - t_\beta)]^2 \tag{2.33}$$

The only undetermined quantity is $\mathbf{m}$ so we calculate $\frac{\partial(S')}{\partial m_k} = 0$. We obtain:

$$\sum_{\alpha=1}^{N} \sum_{\beta=1}^{N} [(\mathbf{r}_\alpha - \mathbf{r}_\beta) \cdot \mathbf{m} - (t_\alpha - t_\beta)] \ (r_{\alpha,k} - r_{\beta,k}) = 0 \tag{2.34}$$

Now, we can define $\mathbf{R}$ as the barycentre of the constellation:

$$\mathbf{R} = \sum_{\alpha=1}^{N} \mathbf{r}_\alpha \tag{2.35}$$

and with an axis translation is always possible to set $\mathbf{R} = 0$.
After calculation, we obtain from Eq. 2.34, keeping in mind the new consideration:

$$m_j \sum_{\alpha=1}^{N} \sum_{\beta=1}^{N} (r_{\alpha,j} r_{\alpha,k} + r_{\beta,j} r_{\beta,k}) = \sum_{\alpha=1}^{N} \sum_{\beta=1}^{N} (t_\alpha - t_\beta) \ (r_{\alpha,k} - r_{\beta,k}) \tag{2.36}$$

At this point we introduce the *volumetric* tensor $\mathcal{R}$, called in this way because its eigenvalues give information about the shape of the polyhedron having the spacecraft as vertices.

$$\mathcal{R}_{jk} = \frac{1}{N} \sum_{\alpha=1}^{N} r_{\alpha,j} \ r_{\alpha,k} \tag{2.37}$$

Then, substituting the volumetric tensor definition in Eq. 2.36

$$2 \ N^2 \ m_j \mathcal{R}_{jk} = \sum_{\alpha=1}^{N} \sum_{\beta=1}^{N} (t_\alpha - t_\beta) \ (r_{\alpha,k} - r_{\beta,k}) \tag{2.38}$$

And if $\mathcal{R}$ is not singular we can obtain $\mathbf{m}$:

$$m_j = \frac{1}{2\ N^2} \left(\sum_{\alpha=1}^{N} \sum_{\beta=1}^{N} (t_\alpha - t_\beta)\ (r_{\alpha,k} - r_{\beta,k}) \right)\ \mathcal{R}^{-1}_{jk} \tag{2.39}$$

It can be seen easily that $|\mathcal{R}| \neq 0$ if the spacecraft are not all coplanar.

2.2 Current density evaluation

The determination of the current density is fundamental in order to have a good understanding of the system we are looking at. In the previous sections the expression *current sheet* has been widely used and the presence of one of them is normally indicated by magnetic field gradients. By the way, it is important to analyse directly the current density.
At this moment, thanks to the MMS data, we are able to compute the current density **J** directly from the particles data. In particular, we are able to get the momenta of both ions and electrons with high time resolution so that **J** can be actually written as:

$$\mathbf{J} = e\ (n_i \mathbf{v}_i - n_e \mathbf{v}_e) \tag{2.40}$$

Where $\mathbf{v}_{i,e}$ are respectively the ion and the electron velocities and $n_{i,e}$ are the ion and electron densities. Furthermore, because of plasma's quasi-neutrality n_i and n_e can be considered equal. This current density will be indicated in the following as $\mathbf{J}_p$ since it is computed with particles data. Since these data were not present in the past, the currents were computed with the *curlometer* technique.

2.2.1 The curlometer technique

It is a multi-spacecraft technique that allows to directly compute the electric current density at the barycenter of a tetrahedron by using four-point magnetic field measurements. The fundamental hypothesis is that the magnetic field gradient can be approximated as linear variations of field between spacecraft. This means that the density current can be considered as constant in the volume occupied by the tetrahedron. Generally, this requires that the scale lengths on which the current density varies are big compared to the spacecraft separation. It has already been developed for the Cluster mission [25]. The basic idea is to compute **J** from the Ampére law

$$\mu_0 \mathbf{J} = \nabla \times \mathbf{B}. \tag{2.41}$$

The finite difference equations that are the base of the curlometer technique can be solved using different methods: an approach based on Stokes' theorem can be used [25] (chap.16); then the method of the barycentric coordinates, [34] as well as the method of least squares,[25] (chap.12). The curlometer also provides an estimate of $\nabla \cdot \mathbf{B}$ (for example, via Gauss's theorem in the

approach based on Stokes' theorem). In this approximation ($\mathbf{B}$ varying linearly), the barycentric estimates for $\nabla \cdot \mathbf{B}$ and $\nabla \times \mathbf{B}$ are identical to those defined by contour integrals as they are supposed to.

In this section, we give a derivation of the barycentric coordinates curlometer technique with a linear interpolation of the field measurements by the four spacecraft, [25] chap.14. This is the approach that is used to compute the current densities in chapter 4.
Since we know the value of the magnetic field only in the point occupied by the spacecraft (the vertexes of the tetrahedron $S_\alpha = 1, 2, 3, 4$), we want to write a continuous field by linear interpolation. The linearly interpolated field $\mathcal{L}[\mathbf{B}](\mathbf{r})$ can be written in this way:

$$\mathcal{L}[\mathbf{B}](\mathbf{r}) = \sum_{\alpha=1}^{4} \mathbf{B}_\alpha \mu_\alpha(\mathbf{r}) \tag{2.42}$$

where $\mathbf{B}_\alpha$ is the value of the field measured at the vertex α and the function $\mu_\alpha(\mathbf{r}) = \nu_\alpha + \mathbf{k}_\alpha \cdot \mathbf{r}$ allows the interpolation. Furthermore, $\mu_\alpha(\mathbf{r}_\beta) = \delta_{\alpha\beta}$. From this condition we obtain $\mu_\alpha(\mathbf{r}) = 1 + \mathbf{k}_\alpha \cdot (\mathbf{r} - \mathbf{r}_\alpha)$ and

$$\mathbf{k}_\alpha = \frac{\mathbf{r}_{\beta\gamma} \times \mathbf{r}_{\beta\delta}}{\mathbf{r}_{\beta\alpha} \cdot (\mathbf{r}_{\beta\gamma} \times \mathbf{r}_{\beta\delta})}, \tag{2.43}$$

an expression for $\mathbf{k}_\alpha$[4].
The vectors $\mathbf{k}_\alpha$ represent the *reciprocal vectors* of the tetrahedron. Each of them appears to be proportional to the area of the face of the tetrahedron opposite to vertex S_α and inversely proportional to the volume of the tetrahedron.

We define $\mathbf{G}[u]$ as the gradient of a scalar quantity u and $\mathcal{G}[\mathbf{B}]$ as the gradient of a field so that $\mathcal{G}_{ij} = \partial_{x_i} B_j$ (in cartesian coordinates). It is straightforward to notice that

$$\mathbf{G}[\mu_\alpha] = \mathbf{k}_\alpha \tag{2.44}$$

Then, since the linear interpolation operator $\mathcal{L}$ is a linear operator we have that $\mathcal{L}[\mathbf{G}](u) = \mathbf{G}[\mathcal{L}](u)$ and $\mathcal{L}[\mathcal{G}](\mathbf{B}) = \mathcal{G}[\mathcal{L}](\mathbf{B})$. So, using Eq. 2.44

$$\mathcal{G}_{ij}[\mathcal{L}](\mathbf{B}) = \mathcal{G}_{ij} \sum_{\alpha=1}^{4} \mathbf{B}_\alpha \mu_\alpha = \sum_{\alpha=1}^{4} \mathbf{B}_{\alpha,i} \mathbf{k}_{\alpha,j} \tag{2.45}$$

The diagonal terms of $\mathcal{G}[\mathbf{B}]$ are the terms of the divergence, $\mathcal{L}[\nabla \cdot \mathbf{B}] = \sum_{\alpha=1}^{4} \mathbf{k}_\alpha \cdot \mathbf{B}_\alpha$; combinations of the non diagonal terms of the tensor give the curl: $\mathcal{L}[\nabla \times \mathbf{B}] = \sum_{\alpha=1}^{4} \mathbf{k}_\alpha \times \mathbf{B}_\alpha$. Furthermore, The differences $\mathcal{L}[\mathcal{G}](\mathbf{B}) - \mathcal{G}(\mathbf{B})$ and $\mathcal{L}[\mathbf{G}](u) - \mathbf{G}(u)$ are respectively, and by definition, the errors of truncation of $\mathcal{L}[\mathcal{G}](\mathbf{B})$ and $\mathcal{L}[\mathbf{G}](u)$.

[4] $\alpha,\beta,\gamma,\delta$ all indicate the vertexes of the spacecraft constellation. They can assume value $1, 2, 3, 4$. We use $\mathbf{r}_{\alpha\beta}$ to indicate $\mathbf{r}_\alpha - \mathbf{r}_\beta$.

The current density obtained from the curlometer technique can be affected by different errors due to different sources:

- error due to deviations from linearity (*physical* error): the magnetic field is assumed to vary linearly in the region occupied by the spacecraft but this condition is quite difficult to be fulfilled in reality.
- measurement errors: the uncertainties of the magnetic field and spacecraft positions determine the error of the current density.
- geometrical error: the quality of the gradient estimates is affected by the shape of the spacecraft configuration.

The last two kind of error mentioned concur to the current density uncertainty $\frac{\delta J}{J}$ in this way:

$$\frac{\delta J}{J} = \frac{|\mathbf{J}|^{curlometer} - |\mathbf{J}|^{model}}{|\mathbf{J}|^{model}} = F_B \frac{\delta r}{\Delta r} + F_S \frac{\delta B}{\Delta B} \tag{2.46}$$

where F_B and F_S are two quantities that depend on the shape of the constellation, in particular on the elongation and the planarity of the tetrahedron but also on the curvature and magnitude of the magnetic field. The value of F_B and F_S is normally taken to be 1 except when the tetrahedron is really far from be regular. Then the value of the parameters can vary between 2 and 10. For seek of simplicity, $\frac{\delta J}{J}$ will be called *measurement* error in the following even though it contains also the contribution of the geometrical error.

The value of $\nabla \cdot \mathbf{B}$ can provide a quality estimate of the physical error of the current density within the tetrahedron. In fact, because of the solenoidality of the magnetic field, $\nabla \cdot \mathbf{B} = 0$. So, the reason to find $\nabla \cdot \mathbf{B} \neq 0$ lies in the fact that there are neglected nonlinear gradients in $\mathbf{B}$.

As a result, we can look at two quality indicators to evaluate the goodness of the curlometer technique applied to a specific structure:

$$\frac{\nabla \cdot \mathbf{B}}{|\nabla \times \mathbf{B}|} \qquad \text{and} \qquad \frac{\delta J}{J}$$

The first one represents the physical error, it is sensitive to the spatial scale of the structure and to its anisotropy. We actually use the ratio $\nabla \cdot \mathbf{B}/|\nabla \times \mathbf{B}|$ instead of the divergence alone in order to handle a dimensionless quantity.

In order to understand whether $\frac{\nabla \cdot \mathbf{B}}{|\nabla \times \mathbf{B}|}$ can be considered as a good indicator for the current density uncertainty, it has been compared to the value of the measurement error for different current density profiles, [25] (chap.16) and [35]. The results indicate that the physical and the measurement errors normally show the same behaviour, except for very large values of elongation and planarity of the constellation. The use of $\nabla \cdot \mathbf{B}$ as an indicator is therefore less valid at extreme distortions of the spacecraft tetrahedron. Then, both the shape of the spacecraft configuration and its orientation relative to the magnetic field structure are important monitors to use. In

addiction, even if the behaviour of the two errors is qualitatively the same, it has been seen on close inspection that the is no point-to-point correlation.

Finally, when $\frac{\nabla \cdot \mathbf{B}}{|\nabla \times \mathbf{B}|}$ remains small we can assume that $\mathbf{J}$ is statistically well represented by the data. More than giving a real vale of the uncertainty of the current density, the field divergence acts as an estimator: it can only indicate whether the current estimate is bad, at least for the case of a regular tetrahedron.

Chapter 3

Instruments and data products

The bulk of our analysis uses data from the MMS mission, [12], [14], [15], [22]. The MMS mission's design is fundamentally different from other multispacecraft magnetospheric missions in that it targets the electron diffusion region, which the four identically instrumented spacecraft, flying in a tetrahedral configuration, probe over a range of interspacecraft separations.
This chapter is divided in two parts. In the first one, an overview of the mission is proposed. In particular, we will present the main new features of the mission, its target and the requirements to reach it. In sections 3.1.1, 3.1.2 and 3.1.3 the orbit, the constellation features and the data products are detailed.
The second part of the chapter is dedicated to the instruments whose data are used in this thesis. It addresses in particular the basic principles, operating modes and data products of those instruments. Section 3.2.1 contains the description of the spin-double probes that together with the axial double probes (section 3.2.2) yields the measurements of the electric field. The analog and the digital magnetometer are described in section 3.2.3 and they yield measurements of the magnetic field. Finally, section 3.3 focuses on the fast plasma investigation instrument which is responsible for the measurements of the distribution function and the momenta of the plasma.

3.1 Magnetospheric Multiscale mission overview

The Magnetospheric Multiscale is a NASA mission launched on March 12, 2015. It consists of a constellation of four identically instrumented spacecraft. Each satellite has an octagonal shape that is approximately 3.5 m wide and 1.2 m high. The satellites have a spin period of 20 s during science operations. The scientific target of this mission is magnetic reconnection in the boundary regions of the Earth's magnetosphere, particularly along its dayside *i.e.* in the magnetopause region and in the magnetic tail (figure 3.1). The fact that the mission is composed by four spacecraft is not a completely new feature: the ESA Cluster mission, launched in 2000, is a four satellites mission as well. However, MMS is fundamentally different from other magnetospheric missions because it targets the very small electron diffusion region in the

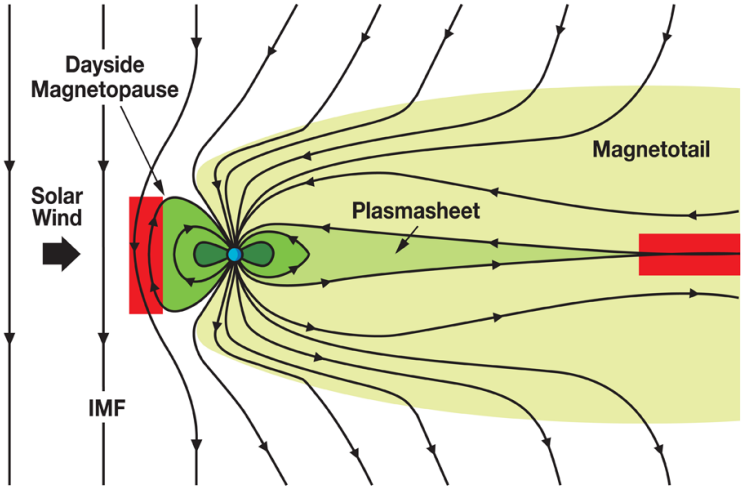

FIGURE 3.1: Target regions of the MMS mission. Adapted from [12].

sites that most likely host magnetic reconnection. In order to do that, higher spatial resolution are needed, as well as unprecedented time resolution (30 ms in order to compute 3D electron distribution functions, 150 ms for the ion distribution function). To achieve such conditions, the inter-spacecraft separation varies from 400 km to as close as 10 km.

The required time scales of the MMS measurements derive from the scale sizes of the electron and ion inertial lengths or skin depths. Equally important are the motions of the reconnection layers (generally oscillatory, in and out, at the dayside magnetopause and tailward in the magnetotail), which have velocities on the order of tens of km/s to over 100 km/s. Simple considerations about the motion led to the conclusion that electron distribution functions need to be measured at an unprecedented time resolution of 0.03 s for electrons and of 0.15 s for ions. In fact, if we consider an electron diffusion region of width $d_{EDR} \sim 5$ km moving at 50 km/s, that would only contain one of the MMS spacecraft for 0.1s. In order to have at least 3 measures a time resolution of 0.03 s is required. Since the ions diffusion region is wider ($d_{IDR} \sim 250$ km), a time resolution of 0.15 s has been chosen, leading ~ 30 measurements taking the same value as before for velocity.
The baseline aim for MMS is to understand the microphysics of magnetic reconnection by determining the kinetic processes occurring in the electron diffusion region that are believed to be responsible for collisionless magnetic reconnection. A major goal is to determine how reconnection is initiated.
One of the first goals is to compute all the terms in the generalized Ohm's law in order to quantify every term's contribution to the electric field. In order to do that MMS will measure full electron distribution functions within the electron diffusion region, ion flow velocities ($100 - 1000$ km/s) with composition (H^+ and O^+), energetic electrons and ions with energies up to 500 keV.

3.1.1 The orbit

The orbit of the mission is shaped in order to explore the regions where the probability of encountering the diffusion region is highest: the dayside magnetopause and the near-Earth magnetotail, [22]. The orbit is then characterised by two different phase of scientific interest. In phase 1 the focus of the mission is on the dayside magnetopause. Its location at the subpolar point varies between 9 R_E and 13 R_E (R_E is the Earth's radius), depending on the pressure of the IMF, so the nominal science region of interest is defined as the region with $d > 9\ R_E$, where d is the distance from Earth. The orbit apogee is set to 12 R_E. The probability of encountering a diffusion region in the dayside magnetopause is higher near the subsolar point, the plane of the orbit is therefore required to make an angle of $\pm 20°$ with the xy plane of the GSE system. The orbit apogee has then to be increased in the second phase of the mission since the probability to cross the diffusion region in the magnetotail is high for $15\ R_E < d < 25\ R_E$. In addition, the nominal region of interest is allowed to shift almost every week according to expected magnetospheric conditions in order to optimize science data collection. The portions of the orbit that are not considered of scientific interest are used for calibration, health/safety, and maintenance activities.

3.1.2 The constellation

Throughout the regions of interest the four MMS spacecraft are maintained in a tetrahedral or pyramid-shaped configuration: one spacecraft is positioned at the origin of the cartesian system and the other three spacecrafts placed in order that the inter-satellites distances are directed as the x, y and z axis of the system. The inter-spacecrafts separation are smaller in phase 1 (160 km to 10 km) and they range between 400 and 30 km in phase 2. The tetrahedral configuration is useful to have four different point of view but it also allows to compute three dimensional gradients of quantities of interest. For example, it is possible to obtain the current **J** using the *curlometer* technique as explained in section 2.2.1. However, we remind that this method can be used only if the non-linear terms of **B** (or the quantity of which the gradient is computed) are neglected and the current can be assumed uniform over the tetrahedron.
The optimal constellation configuration is a regular tetrahedron with separation appropriate to the region of interest crossed by the spacecraft. A quality factor was already defined for the Cluster mission:

$$Q_C = \frac{V_{act}}{V_{reg}}$$

where V_{act} is the volume of the actual MMS tetrahedron and V_{reg} is the volume of the regular tetrahedron having as sides the average of the spacecrafts separations of the actual formation. Since for the MMS mission also the spacecraft separation in function of the position in the orbit is a crucial parameter, a new quality factor is defined:

$$Q_{MMS} = Q_C \cdot Q_{sep}$$

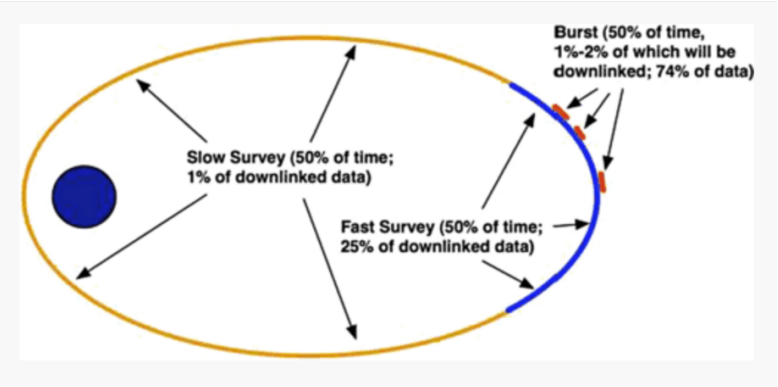

FIGURE 3.2: The slow survey collection period represent about half of each orbit period (orange curve), but comprises only about 1% of the downlinked data. The fast survey data are collected within each region of interest (blue curve) and comprise about 25% of the downlinked data. Burst intervals (red segments) will comprise 75% of downlinked data. Adapted from [15].

where Q_{sep} takes into account the spacecraft separations, [22].

3.1.3 The data

There are two basic instrument science operation modes, *slow survey* and *fast survey* and three data acquisition rates: *slow*, *fast* and *burst*, [15]. Outside of the region of interest, slow survey mode is used while the fast survey mode is used within the regions of interest. The data are acquired in both the fast and burst rates and they are stored onboard at the highest resolution. The time resolution of the fast mode data is comparable (and in some cases faster) than that of previous magnetospheric mission; the burst data resolution is one or two times faster than the fast data's one. Then, the data acquired at fast rates are totally transmitted to the ground. The same treatment is not possible for the burst data because of their high resolution: they have a volume that exceed the capability of the MMS telemetry transmission system.
Even though almost 75% of the telemetry bandwidth is allocated to burst data, this allows the transmission of $\sim$ 2% of the totality of the burst data. This means $\sim$ 15 minutes per day which are sufficient, most of the time, to transmit to the ground all the segments that contain a magnetopause crossing within an orbit. Therefore, the instruments have several burst mode triggers that select the highest quality events for transmission to the ground.

The selection of the data segments is not trivial and download priority is given to segments where the spacecraft are in their high-rate data collection mode precisely when sites of magnetic reconnection have been probed. This cannot be done *a priori*: it is necessary to analyse the lower resolution measurements in order to understand which parts of the burst data should be transmitted to the ground. The basic strategy of MMS mission is to store all of the burst data obtained during an orbit ($\sim$ 1 to 3 days) in mass memory and then later select the most scientifically interesting segments of burst data (15 minutes for a 1-day orbit up to 45 minutes for a 3-day orbit) for transmission. The selection of the scientifically interesting periods is based on data quality values calculated on board and on survey data.
Even if a burst data trigger system has been developed, for the moment its activity is still

controlled by scientists that check the automatic selection and change it by including more segments if needed. This procedure is called *Scientist-In-The-Loop* (SITL).

In addition, multiple categories of data are produced and they are characterised by different levels of refinement and calibration. The *level 1* data are raw data at full resolution that are time-referenced; the *QuickLook* ones are scientific data products that are rapidly generated using simplified processing algorithms. These data provide basic scientific insight but they are characterised by provisional calibrations. Their generation occurs after some hours from the reception. Finally, the *level 2* data represent the highest level of research grade scientific data. They derived from the calibration of level 1 data, they have the same spatial or time resolution of the *level 1* data.

3.2 Fields measurements

Fields measurements are accomplished on MMS with six sensors integrated into the FIELDS suite, a scheme is shown in figure 3.3. The FIELDS suite contains in particular the Analog FluxGate (AFG) and the Digital FluxGate (DFG) for magnetic field measurements; the Spin-plane Double Probe (SDP) and the Axial Double Probe (ADP) for electric field measurements. Since data from this four instruments are used in the following, the next sections will focus on the basic principles and the operating modes of these instruments.

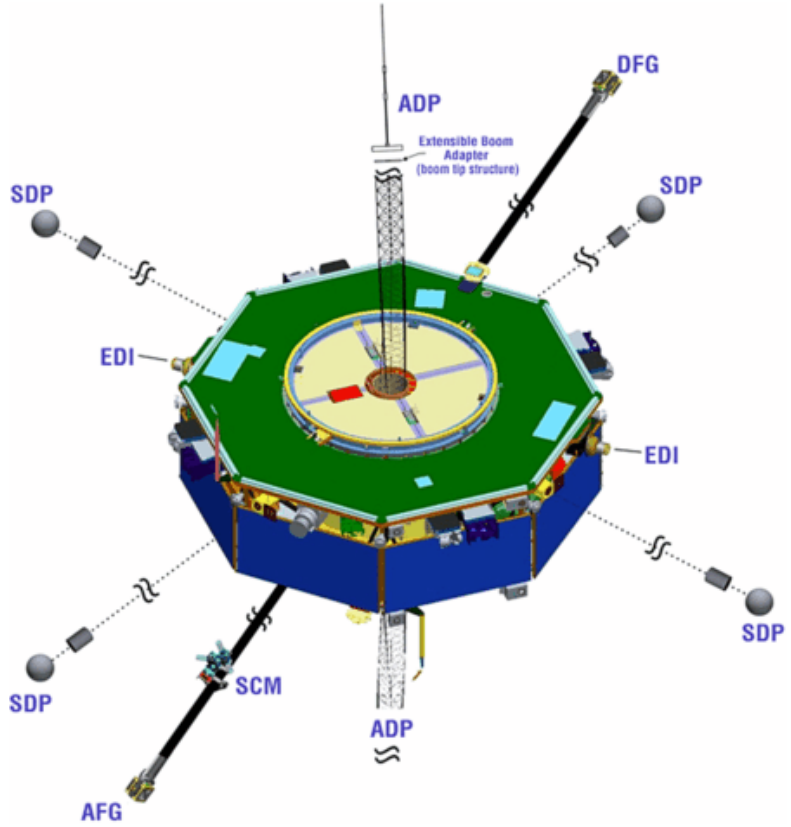

FIGURE 3.3: FIELDS sensors on a MMS spacecraft. The acronym EDI indicates the Electron Drift Instrument, it will not be detailed in this work. Adapted from [39].

3.2.1 Electric field measurements: the Spin-Plane Double Probe (SDP)

The Spin-plane Double Probe instrument (SDP) [40] measures the electric field in the spin plane from the potential difference between four spherical titanium-nitride electrodes, each of diameter 8 cm at the end of wire booms with a length of 60 m, as represented in the sketch in figure 3.4. Together with the axial double probe instrument (ADP, described in the next section), SDP measures the 3-D electric field with an accuracy of 0.5 mV/m over the frequency range from DC to 100 kHz.
The requirement for a relatively long distance between the probes and the spacecraft comes from the necessity to overcome the effects of the Debye shielding as well as the effects of the photoelectrons. Furthermore, a larger distance between the probes results in a larger potential difference, which is easier to measure. The potential difference between two opposed probes yields a measurement of the electric field in the direction along the axis defined by the two probes. Since two pairs of probes are present, we are able to have an estimation of two orthogonal components of the electric field in the plane of the spacecraft spin.

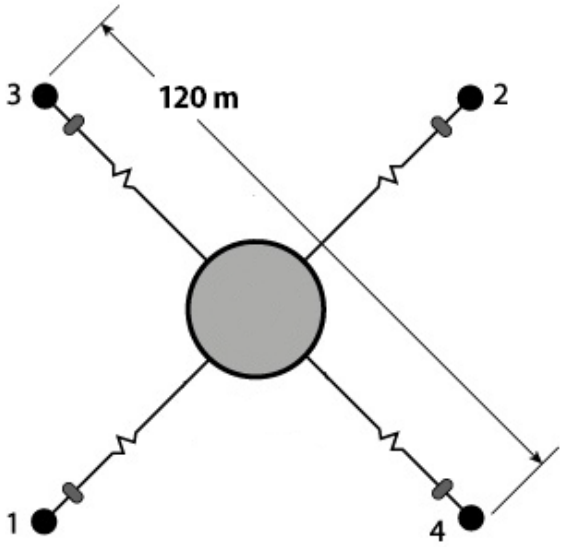

FIGURE 3.4: Schematic representation of the SDP four probes in the spin plane.

The tricky part of this measure lies in the fact that a metal sphere into a sunlit plasma does not sit at the same potential as the plasma around it. This is due to the interaction between the sphere and the photons coming from the Sun and the interaction between the sphere and the plasma itself. In particular, the interaction with the photons leads the sphere to be charged positively (because of the escaping photoelectrons) while the colliding particles of the plasma determines a net negative charge on the sphere (the plasma is globally neutral but the electrons are usually hotter than the ions). Both of these effects are usually in action, leading to an equilibrium state where:

$$I_{ph} + I_i = I_e \tag{3.1}$$

where I_{ph} is the photo-electron current, I_i is the plasma ion current and I_e is the plasma electron current. All currents are defined as positive *to* the probe, so that $I_e < 0$, $I_{ph} > 0$, $I_i > 0$. From this balance we are able to obtain the sphere's potential. In tenuous plasma such as the magnetosheath and the solar wind, the photo-electron current completely dominates. That leads to relatively high potential ($> 10\ V$). Additionally, the spacecraft potential has large variations for small fluctuations of the currents. In order to mitigate that effect an additional current I_{bias} is drawn by the instrument. This bias current adjust the spacecraft potential to a small positive value, allowing for a more steady spacecraft potential. I_{bias} can be set in the range $(-550\ nA, +110\ nA)$ and it needs to be adjusted over the course of the mission to account for changing solar photons flux and probe surface characteristics.

The SDP electric field instrument has only one basic operational mode, measuring the electric field and two individual probe potentials relative to the spacecraft. In contrast to other missions (*e.g.*, Cluster), which also had the possibility to set a voltage to the probes and measure the resulting current (the Langmuir mode), SDP can only set the bias current to the probe and measure the voltage (the E-field mode). The bias current will be set to compensate for emitted photoelectrons (which dominate in sunlight), and/or collected ambient plasma electrons (dominating in eclipse): the purpose is to keep the probe potential near the plasma potential. The instrument is also capable of an automatic sweep of the bias current, in order to get a $I - V$ characteristic. This procedure will be done outside the region of scientific interest in order to optimise the adopted value of I_{bias}.

The sampling frequencies are 8 Hz in slow survey, 32 Hz in fast survey, and 1024, 8192, or 65536 Hz in burst. After reception on the ground, SDP data will be combined with ADP data to yield the full electric field vector.

3.2.2 Electric field measurements: the Axial Double Probe (ADP)

The Axial Double Probe (ADP) instrument [41] measures the DC to $\sim 100\ kHz$ electric field along the spin axis of spacecraft, completing the 3-D electric field when combined with the SDP measurements. The presence of an axial probe allowing for the measurement of the complete electric field vector represents a new feature of MMS compared to Cluster, where the third component was computed using the relation $\mathbf{E} \cdot \mathbf{B} = 0$. The ADP is expected to measure DC electric field with a precision of $\sim 1\ mV/m$, a resolution of $\sim 25\ V/m$, and a range of $\sim \pm 1\ V/m$ in most of the plasma environments MMS will encounter.
Two cylindrical sensors are separated by over 30 m tip-to-tip. The antenna lengths are constrained by mechanical limitations, in particular deployment of rigid booms while preserving spacecraft stability. The ADP booms are designed to have cylindrical symmetry, primarily to eliminate modulation of the photoelectron current as the spacecraft rotates. The design also optimizes symmetry between the +Z and Z sensors; opposing sensors experience nearly the same potential created by the spacecraft and its booms and they have nearly identical photo- and secondary electron environments. The principles on which the ADP operates are the same of the SDP so they will not be detailed again here.
Data from SDP and ADP are combined in the EDP data products.

3.2.3 Magnetic field measurement: the Fluxgate Magnetometers (FGM)

On each spacecraft, the magnetic field measurements are acquired using two tri-axial fluxgate magnetometers, one of each mounted on the end of two 5 m booms. The two magnetometers are actually of two different kind: the Digital FluxGate (DFG) and the Analogue FluxGate (AFG). If magnetometers of the same kind are put onto the same spacecraft, they may experience similar problems and thus redundancy is reduced. Thanks to their different design approaches, AFG and DFG provide redundancy for the MMS magnetic field measurements. Of course, the signals from the two types of magnetometers are constantly compared and calibrated. The two magnetometers produce 3-D magnetic field measurements with an accuracy of 0.1 nT over the frequency range from DC to 64 Hz. The instruments form a synchronized, redundant, cross- and inter-spacecraft calibrated pair of magnetometers on each spacecraft. All details can be found here [42]. In this section we describe the basic principle of the instrument.
A fluxgate magnetometer consists of a ferromagnetic core wrapped by two coils of wire. An alternating electric current is passed through one coil, driving the core through an alternating cycle of magnetic saturation. This constantly changing field induces an electric current in the second coil, and this output current is measured. In absence of external magnetic field, the input and output currents are the same. However, when the core is exposed to a background field, it will be more easily saturated in alignment with that field and less easily saturated in opposition to it. Therefore, an external magnetic field will create an offset between the input and the output currents which yields a measurement of the magnetic field. The difference between the two currents is proportional to the strength of the background magnetic field.

The DFG and the AFG data are combined into a single FGM data product, the best data suited for general science are chosen.

3.3 Plasma measurements: the Fast Plasma Investigation (FPI)

The Fast Plasma Investigation (FPI) is dedicated to the rapid measurement of the phase space densities and 3-D space distributions of electrons and ions with unprecedented time resolutions of 30 ms and 150 ms for electrons and ions respectively. FPI has an energy range of (10 eV, 30 keV) with a resolution of the 20 % or better and an angular resolution of 15°. On each spacecraft, the FPI consists of eight electron spectrometers and eight ion spectrometers. These are organised in pairs in back-to-back configuration, as dual spectrometers for each species called DES and DIS. Four dual spectrometers for each species are placed around the spacecraft perimeter at 90° intervals as shown in figure 3.5.

The FPI spectrometers are *top hat* electrostatic analyzers (ESA). In its simplest configuration, *top hat* ESA consist of three concentric spherical section elements: an inner hemisphere with radius R_1 set to a potential V_{ESA}, an outer hemisphere with radius $R_1 + \Delta_1$ which contains a circular hole on the top and a small *top cap* section of radius $R_1 + \Delta_1 + \Delta_2$ positioned in conjunction with the hole of the the outer hemisphere, see figure 3.6. The region between the

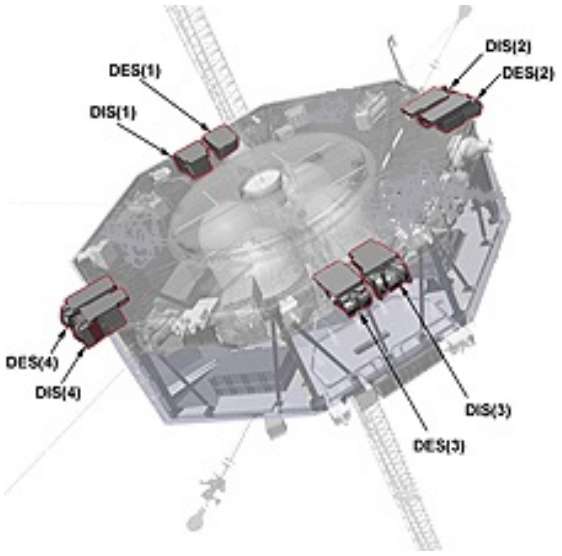

FIGURE 3.5: Schematic representation of the Dual Electron Spectrometers (DES) and Dual Ion Spectrometers (DIS) composing the FPI instrument. Adapted from [12].

outer hemisphere and the *top cap* defines the cylindrical entrance aperture and then also an acceptance angle [44]. The *top hat* ESA selects particles in function of their velocity's direction and of their energy (for unit of charge) $\epsilon = E/q$. When a V_{ESA} is applied to the inner hemisphere an electric field between the nested hemispheres is produced. The particles with the appropriate velocity's direction and energy are guided in the region between the two hemispheres and reach a detector. All the other particles collide against the walls of the analyzer and are absorbed or deviated. A stepped V_{ESA} sequence is used to change the central energy ϵ of the band pass $(\epsilon + \Delta\epsilon, \epsilon - \Delta\epsilon)$. The energy of the accepted particles varies proportionally to V_{ESA}.

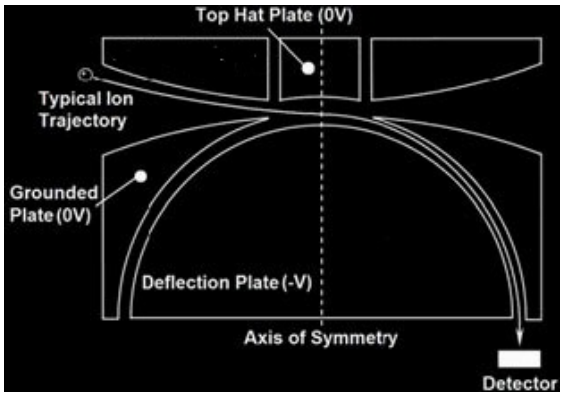

FIGURE 3.6: A scheme of the *top hat* electrostatic analyzer used in the FPI instrument.

Note that a *top hat* ESA allows simultaneous observation over an angular range of up to 360° in the plane perpendicular to the symmetry axis. FPI only uses 180° of the top hat's potential field of view, and we refer to this angular dimension as the polar angle θ because it corresponds to the angle opening from the spacecraft Z-axis. The FPI sensors consist of a *top hat* ESA with a 180° field of view able to span from the spacecraft spin axis to the anti spin axis. Each sensor is oriented so that the 16 pixels (each nominally 11.25° wide) of its 180° field of view are viewing radially in velocity space. The pole-to-pole pixel array and the distribution of eight

spectrometers around the spacecraft azimuth provide simultaneous sampling in the polar (θ) and azimuthal (ϕ) angular dimensions.
The fact that the sensors are distributed all around the spacecraft allows to have a full azimuthal sampling without depending on the spin of the spacecraft. This is a peculiarity of FPI since spacecraft spin has typically set the effective time resolution achievable for 3-D plasma measurements.

In order to reach the full view of sky, the FPI spectrometers also present electrostatic field of view deflection, such that center of the azimuth angle of the filed of view of each spectrometer may be deflected in the azimuth coordinate by up to $\sim \pm 17°$. Each of the eight DIS and DES samples 4 azimuths, providing a total 32 azimuthal samples separated by 11.25° for each species. This azimuth coverage is illustrated in figure 3.7.

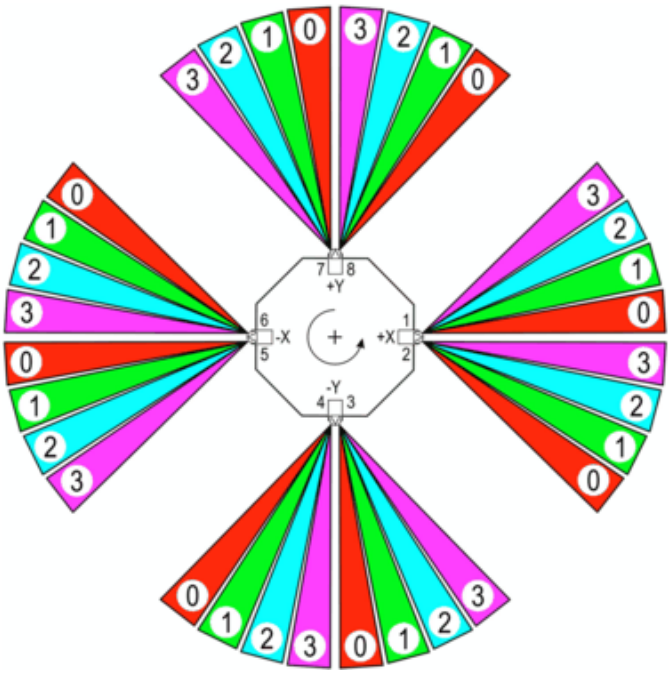

FIGURE 3.7: Azimuth coverage reached by the DIS and DES of the FPI instrument: each analyzer of each species samples 4 azimuths giving 32 azimuthal samples, 64 in total if we consider ions and electrons together.

The particles are then detected with Micro Channel Plates (MCP) which amplify each incoming electron or ion into a pulse of outgoing electrons. The number of particles per pulse is characterized with a histogram. The detector system and data processing are not detailed but all information can be found here [43]. The fundamental products in the burst mode are the so-called *skymaps*: they contain the raw counts from DES and DIS. These are count rate arrays 32 $\epsilon \times$ 32 $\phi \times$ 16 θ accumulated every 30 ms for DES and 150 ms for DIS. These data are put in the De-spun Body Spacecraft Coordinate System (DBCS) that is very close to Geocentric Solar Ecliptic (GSE) coordinates (within $2° - 3°$). In that way, a distribution function in the coordinates $(\epsilon, \phi, \theta, t)$ is obtained. This is converted in the distribution function that depends on $(\mathbf{v}, \mathbf{r}, t)$. Finally, the distribution function is properly integrated in order to obtain all the momenta.

Chapter 4

Observations: the event of October, 3 2015

In this chapter the first part of my work is presented. The bulk of the thesis is composed by the analysis of data from the Magnetospheric Multiscale (MMS) mission. On October 3, 2015, around 1500 UT the MMS satellites were at $(6.1, 10.1, -0.6)$ R_E (GSE), *i.e*, in the afternoon side of magnetosphere. The spacecraft were approximately in a regular tetrahedron formation, with separation distances of about 20 km, as you can see in figure 4.1. The magnetopause passed the spacecraft formation several times. For our study, we will consider the MMS data of October, 3 2015 between 14:45:34 (UTC) and 14:48:04(UTC), where two complete magnetopause crossings occured.

Since the analysis focuses on repeated magnetopause crossings, as already underlined in chapter 2, the first thing to do is individuate the proper frame of the magnetopause. Then, we characterise the boundary with its velocity and its width. In order to compute the discontinuity local frame and the discontinuity's velocity, the methods explained in chapter 2 are used. They are single or multi-spacecraft methods. In section 4.1 the Minimum Variance method is used. It needs only the magnetic field data. We perform the analysis on each crossing separately and we obtain two local discontinuity frames that are quite different. We conclude that the magnetopause is moving fast and in a way that does not allow us to define a single local frame able to describe the discontinuity along the entire interval containing two crossings. We define a local frame for the first crossing (section 4.1.1) and a local frame for the second (section 4.1.2).

In section 4.2 the *timing* method is applied to each crossing. We find a good agreement with the results of the MVA method, especially for the first crossing, while the structure of the signal during the second one does not allow such a good accordance. The *timing* method yield also the normal component of the velocity. Thanks to that, the width of the magnetopause crossed by the spacecraft is computed in section 4.2.1. Another estimation of the normal component of the velocity is given by the *deHoffmann-Teller* method. Results are shown in section 4.4. There is a quite good agreement with the values we get from the *timing* method.

The last section of the chapter is devoted to the computation of the current density, exploiting both the *curlometer* technique and the data from the *FPI* instrument. This analysis shows that

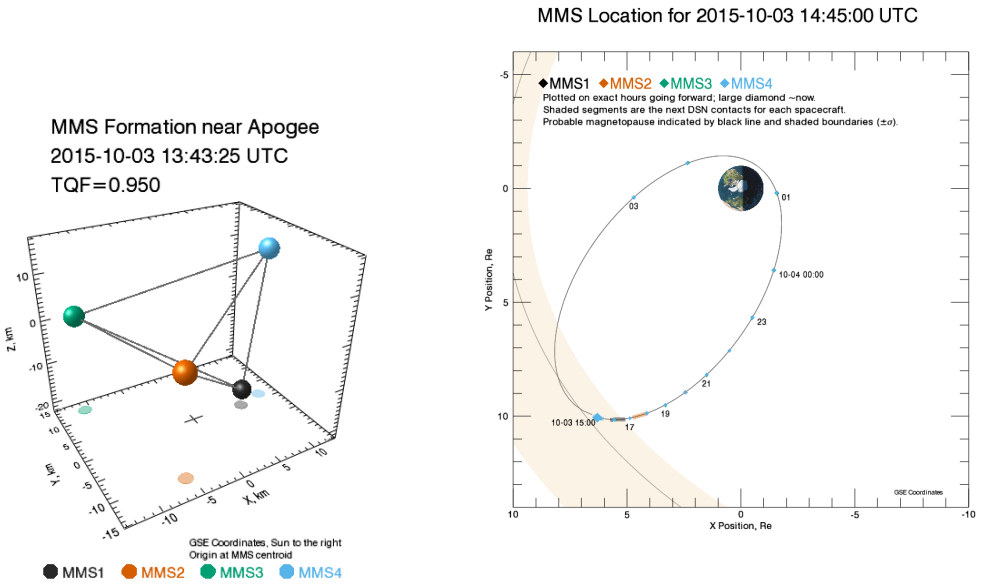

FIGURE 4.1: The tetrahedral formation and the position of the constellation in the orbit on the October 3, 2015 at around 1500 UT.

currents computed with the two different methods have globally the same behaviour and that the current density peaks in correspondence of the magnetic field inversions.

4.1 Minimum Variance Analysis of the magnetic field

In order to investigate and understand the data obtained by the MMS spacecrafts and to individuate the optimal spots for magnetic reconnection it is necessary, first, to individuate how the magnetopause is oriented in space and the region where measures were taken. A preliminary way to select a good set of data is to individuate current sheets. The presence of a current sheet is usually due to inversions of the magnetic field and this configuration can lead to magnetic reconnection. In addiction, if we want to understand whether magnetic reconnection is taking place or not, we should be able to measure the normal to the current sheet component of $\mathbf{B}$. If we consider the simplest 2D model of magnetic reconnection in which the current sheet separates two regions with opposite directed $\mathbf{B}$ fields, the presence of a magnetic field directed along the normal to the current sheet would be a sign of reconnection. The difficulty lies in the fact that generally $|\mathbf{B} \cdot \hat{\mathbf{n}}| \sim 1 - 2\ nT$. This quantity is small compared to the norm of the magnetic field (generally $\sim 20 - 50\ nT$) and even if the instrumental error can be small thanks to optimal calibration $(\delta \mathbf{B_n})_{instr} \sim 0.1\ nT$, there are several causes that make the error bigger. For example, the spin of the satellites makes harder to have a good estimation of the quantities in the axial direction in the spacecraft frame. Then, on one side the instrumental error can be bigger than $0.1\ nT$ and other sources of incertitude can be present. An other source of incertitude is the minimum variance methods itself, that gives an error as well.
The data are given by the *FGM* instruments which measure the magnetic field with a sampling frequency of 128 Hz.

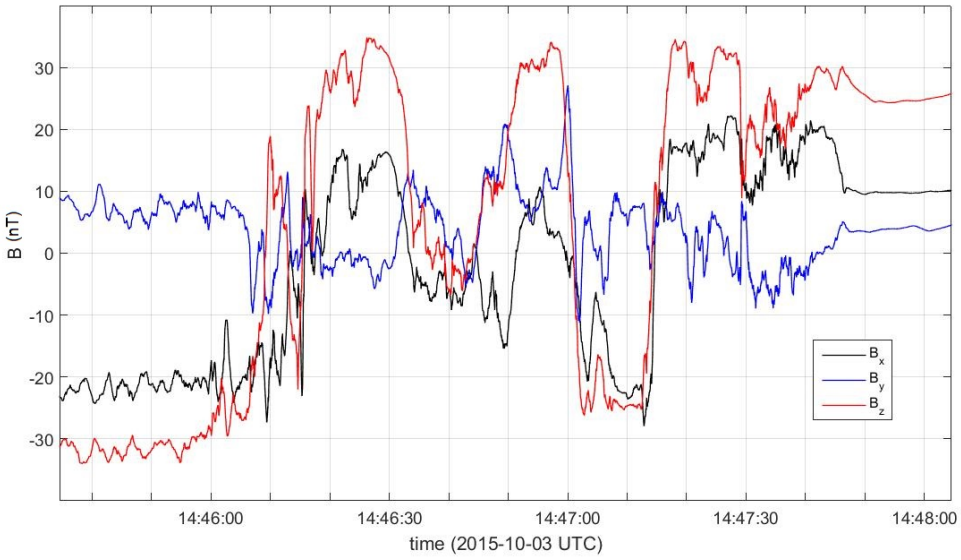

FIGURE 4.2: Components of the magnetic field from MMS1, entire interval.

TABLE 4.1: Time interval 1

t_1	$2015-10-03T14:46:55.9273Z$
t_2	$2015-10-03T14:47:10.1939Z$

In this section, the results from the MVA method are shown and, since it is a single spacecraft method and the signals from the spacecraft are almost identical, data from the satellite MMS1 will be used in all the images.

In figure 4.3 all the data of the studied interval are represented, they are *burst* data of level *l2*. As we can see, different partial and total magnetopause crossing are present (this will be justified looking at the behaviour of density and temperature). We will treat each crossing singularly, focusing on the ones that are likely to be complete crossings. The purpose of this sections is to find, for every crossing and for every satellite, the frame that has the directions of minimum, intermediate and maximum variance as axes: we want to know how the layer is oriented and whether it can be considered stationary or not. For the MVA on the magnetic field, we will select every time a time interval that contains only the considered crossing: we want to avoid a final minimum variance direction which is a mean between the $\hat{\mathbf{n}}$ of two different structures of the $\mathbf{B}$ field. This means that we will choose a quite narrow interval (compared to the total duration) that does not contain others 'structures' except for the selected magnetopause crossing.

4.1.1 First magnetopause crossing

I select the instant representing the *current sheet* of the first complete crossing: $t_{cs,1} = 2015-10-03T14:47:00Z$.

Looking at the magnetic field signal, one can notice that we are in the presence of an inversion of it. This makes us think about an actual transition from magnetosphere to magnetosheath.

TABLE 4.2: Time interval 2

t_1	$2015-10-03T14:46:58.00Z$
t_3	$2015-10-03T14:47:03.00Z$

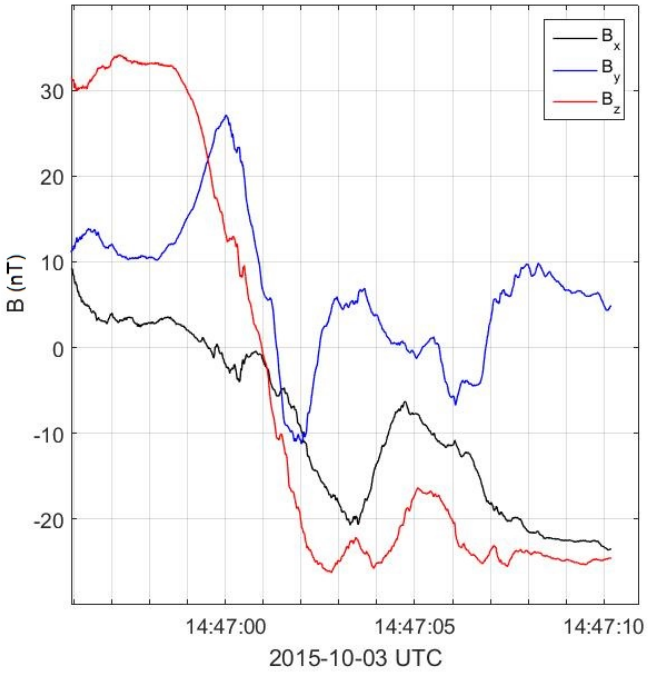

FIGURE 4.3: The three components of **B** from MMS1, first complete magnetopause crossing, time interval 1.

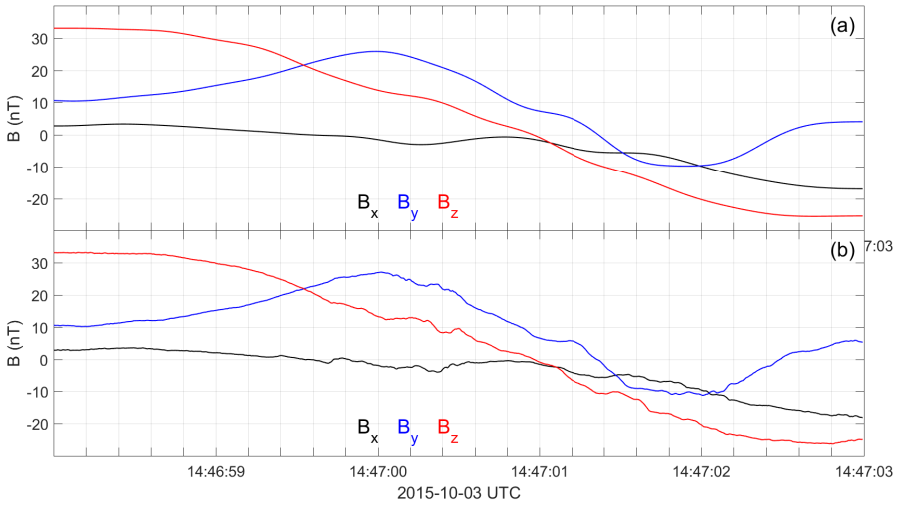

FIGURE 4.4: The three components of **B** from MMS1, first complete magnetopause crossing in time interval 2. The first panel shows the signal after the action of the low-pass filter with $f_{max} = 2\ Hz$, the second panel shows the 'raw' signal.

We can confirm such a hint by looking to the densities and temperature evolution. In panel b of figure 4.5 we can see a decrease in the ionic temperature, while the electronic temperature (panel d) maintains more or less a constant value in that interval. We have also to notice that $T_e \sim 60\ eV$ while $T_i \sim 2000\ eV$ in the first part of the interval and then becomes $T_i \sim 200\ eV$ in the last part of the transition. Since $T_e \ll T_i$ we can focus on the behavior of T_i and we find out that it reproduces the evolution of a crossing from the magnetosphere to the magnetosheath. Note that this is only a qualitative way to interpret what the data are showing. In order to do this, T_e and T_i are computed as the trace (divided by 3) of the temperature tensor. We are aware that we are not taking into account the anisotropies but the aim, at this point, is to have a general understanding of the temperature behaviour.

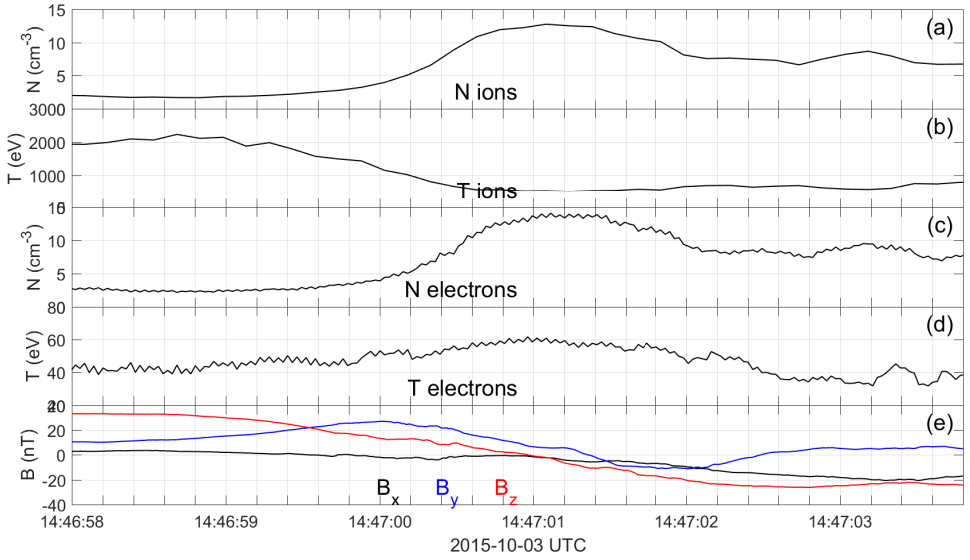

FIGURE 4.5: In panel (a) we have the ion density (cm^{-3}). In panel (b) the ions temperature (eV) is shown. Panel (c) containts the electron temperature (eV), panel (d) the electron density (cm^{-3}). In panel (e) we have the three components of the magnetic field (nT). All the data are from MMS1.

Another control can be done by looking at the ions and electrons density evolution (figure 4.5). Then, the density behavior reproduces the one expected from a magnetosphere-to-magnetosheath crossing, passing from a $n_e \sim n_i \sim 3\ cm^{-3}$ to $n_e \sim n_i \sim 10\ cm^{-3}$. Since the typical value of the density in the magnetosheath is $\sim 50\ cm^{-3}$ we infer that at the end of the interval we are still in the boundary layer.

Now we can start to analyse the magnetic field, in order to find the normal to the discontinuity. The first step is to apply a low-pass filter to the data. As one can see in figure 4.3 there are a lot of picks and fluctuations in the signal. These are mostly due to the presence of waves. These high frequencies can affect the computation of the minimum variance: increases and decreases in the signal lead to continuous readjustments of the minimum variance direction even if they are caused, for example, by a wave propagating on the magnetopause surface.

We select the maximal frequency in an *empirical* way: we begin with $f_{max} = 1\ Hz$ and then we adjust f_{max} to maintain the original data trend and not to pollute the signal with the effects of a too small sampling frequency. On the other side, we want to control the changing in the

TABLE 4.3: Variation of ϕ_i in function of f_{max}

$f_{max}(Hz)$	$\phi_3(^\circ)$	$\phi_1(^\circ)$
1	0.0552	0.00860
3	0.0059	0.00094
5	0.0028	0.00043

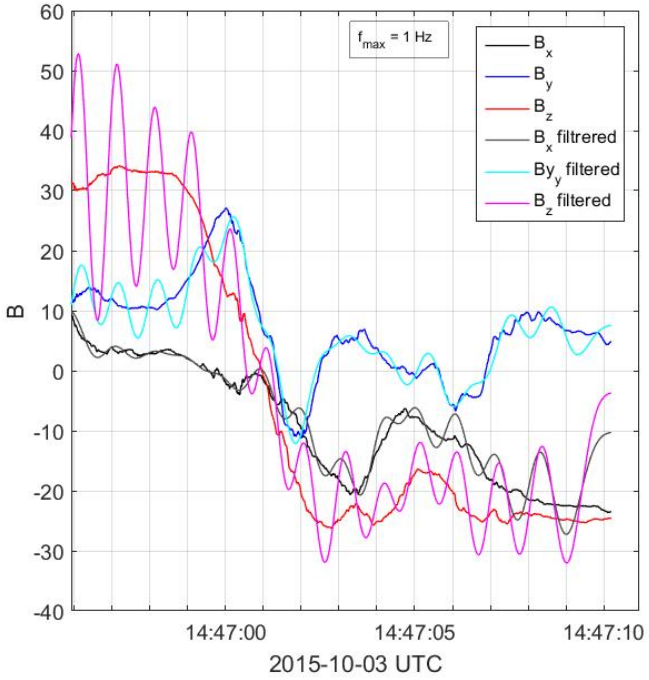

FIGURE 4.6: The three components of **B** from MMS1 in the time interval 1 and the result after the filtering with $f_{max} = 1\ Hz$.

direction of the minimum (and maximum variance) by computing the amplitude (in degrees) of the angle between the minimum ϕ_3 (maximum, ϕ_1) variance eigenvector computed with the original and the filtered data. In picture 4.6 we can see that the filtered field with $f_{max} = 1\ Hz$ presents artificial oscillations due to the low-pass filter. It is sufficient to have $f_{max} = 2\ Hz$ to obtain a better result. Furthermore, we can compare the values of ϕ_1 and ϕ_3.

Looking at table 4.3, we can see that $\phi_1 \ll 1^\circ$ and $\phi_3 \ll 1^\circ$ so the two vectors have substantially the same direction. Nevertheless, we can notice that ϕ_3 and ϕ_1 are decreasing with the augmentation of f_{max}. We select $f_{max} = 2\ Hz$. We obtain, for each spacecraft, the eigenvectors and eigenvalues resulting from the minimum variance analysis, the ratio between the eigenvalues and the values of ϕ_3 and ϕ_1. We use the second time interval because the ratio between the eigenvalues of minimum and intermediate variance is higher. This means that the direction of minimum variance is better identified. In fact, for the time interval 1 of table 4.1:

$$\overline{\left(\frac{\lambda_2}{\lambda_3}\right)} = 4.87 \tag{4.1}$$

TABLE 4.4: Eigenvectors obtained with the MVA method and their angular incertitudes in the first crossing

	$mms1$	$mms2$	$mms3$	$mms4$
$\mathbf{v}_1$	$(0.34, 0.21, 0.92)$	$(0.34, 0.22, 0.92)$	$(0.34, 0.22, 0.91)$	$(0.34, 0.21, 0.92)$
$\mathbf{v}_2$	$(0.44, -0.90, 0.04)$	$(0.41, -0.91, 0.07)$	$(0.44, -0.90, 0.05)$	$(0.43, -0.90, 0.05)$
$\mathbf{v}_3$	$(0.83, 0.39, -0.40)$	$(0.85, 0.35 - 0.40)$	$(0.83, 0.38, -0.40)$	$(0.840.38 - 0.40)$
$\lvert\Delta\phi_{13}\rvert$ (rad)	0.0035	0.0018	0.0027	0.0031
$\lvert\Delta\phi_{23}\rvert$ (rad)	0.0127	0.0064	0.0102	0.0107
$\lvert\Delta\phi_{12}\rvert$ (rad)	0.0040	0.0021	0.0031	0.0035

while for the time interval 2 (see table 4.2),

$$\overline{\left(\frac{\lambda_2}{\lambda_3}\right)} = 9.07 \tag{4.2}$$

Averaging the values of the eigenvectors obtained from the four spacecraft we get a mean value for the normal direction $\hat{\mathbf{n}}_{MVA}$.

$$\hat{\mathbf{n}}_{MVA} = \overline{\mathbf{v}_3} = (0.84,\ 0.38,\ -0.40) \tag{4.3}$$

Doing the same with the others eigenvectors we obtain the following set:

$\overline{\mathbf{v}_1}$	$(0.34,\ 0.22,\ 0.92)$
$\overline{\mathbf{v}_2}$	$(0.43,\ -0.90,\ 0.06)$
$\overline{\mathbf{v}_3}$	$(0.84,\ 0.37,\ -0.40)$

These three vectors are supposed to be a orthonormal set. Since they are an average from four different measures the orthonormality is not always held. We create a proper set choosing $\overline{\mathbf{v}_3}$, the vector between $\overline{\mathbf{v}_1}$ and $\overline{\mathbf{v}_2}$ that better respects the orthogonality condition with $\overline{\mathbf{v}_3}$ and then the vector got from the cross product between the first two components of the set.
Since $\overline{\mathbf{v}_3}\cdot\overline{\mathbf{v}_1} \sim 6\cdot10^{-5}$ and $\overline{\mathbf{v}_3}\cdot\overline{\mathbf{v}_2} \sim 10^{-5}$, the three vectors seems to be already quite orthogonal. By the way, we take $\overline{\mathbf{v}_2}$ as component of the set of the minimum variance frame. The third vector will be $\mathbf{l} = \overline{\mathbf{v}_3} \times \overline{\mathbf{v}_2} = (0.33,\ 0.22,\ 0.92)$. Let us use the letters LMN to indicate the axis of the new frame. In literature, the letters LMN indicate the three axis of a frame situated at the magnetopause nose. N indicates the normal direction to the magnetopause and it points through the magnetosheath, L and M are two vectors direct tangentially to the magnetopause: L is usually directed northwards (at the magnetopause nose this is also the Earth's magnetic field direction), and M direction is defined as the result of the cross product between N and L direction. The set is indicated in the following as $(\mathbf{l}, \mathbf{m}, \mathbf{n})$.

l	(0.33, 0.22, 0.92)
m	(0.43, −0.90, 0.06)
n	(0.84, 0.38, −0.40)

TABLE 4.5: LMN frame for the first crossing

4.1.2 Second magnetopause crossing

We select the instant representing the *current sheet* of the second complete magnetopause crossing: $t_{cs,2} = 2015 - 10 - 03T14 : 47 : 15.00Z$.
As for the first crossing analysis we show at first the temperature's and density's behaviour. In figure 4.7 we can see a decrease in the ionic temperature, while the electronic temperature maintains more or less a constant value in this interval. We have also to notice that $T_e \sim 60\ eV$ while $T_i \sim 1300\ eV$ in the first part of the interval and then becomes $T_i \sim 250\ eV$ in the last part of the transition. Since $T_e \ll T_i$ we can focus on the behavior of T_i and we find out that it reproduces the evolution of a crossing from the magnetosheath to the magnetopause. This figure has the aim to show qualitatively that we are in such kind of transition so the anisotropy of the temperature tensor is not taken into account and T_e and T_i are computed as the trace (divided by 3) of the temperature tensor. Nevertheless, this gives a first insight of the process.

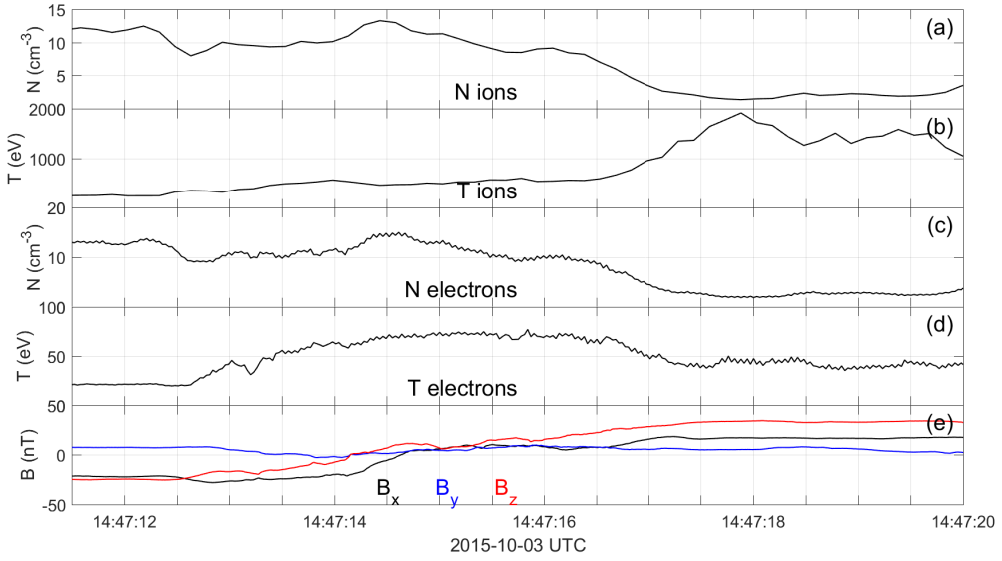

FIGURE 4.7: In panel (a) we have the ion density (cm^{-3}). In panel (b) the ions temperature (eV) is shown. Panel (c) containts the electron temperature (eV), panel (d) the electron density (cm^{-3}). In panel (e) we have the three components of the magnetic field (nT). All the data are from MMS1.

Another control can be done by looking at the ions and electrons density behaviour in figure 4.7. Note that the density behavior reproduces the one expected from a transition from magnetosheat to magnetosphere, passing from a $n_e \sim n_i \sim\ 10cm^{-3}$ to $n_e \sim n_i \sim 2\ cm^{-3}$. Since the typical value of the density in the magnetosheath is $\sim 50\ cm^{-3}$ we infer that at the end of the interval we are still in the boundary layer.

As we did in section 4.1.1, we start now the analysis of the magnetic field and the first step is to apply a low pass filter to the data.
In this case we adopt $f_{max} = 5\ Hz$ or $f_{max} = 4\ Hz$ depending on the spacecraft and we choose it comparing the eigenvalues ratio: it happens that a f_{max} of 4 Hz gives a signal's reproduction as good as $f_{max} = 5\ Hz$ but it yield to a higher value of $\frac{\lambda_2}{\lambda_3}$.
The individuation of the direction of minimum variance is less easy for this crossing. This can be due to the structure of the signal. For example, looking at B_z from the spacecraft MMS1 in figure 4.8 we can see that the transition between magnetosheath and magnetosphere is not characterised by a monotone behaviour. There is at least one wide interval (relatively to the total duration of the crossing) where we can notice a sort of perturbation: from 2015-10-03T14:47:14.70Z to 2015-10-03T14:47:15.95Z the signal is not monotone, it increases and it decreases twice. This is a low frequency effect that can not be eliminated with the usual low pass filter that allows to work with smoother signals.
We apply the MVA method to the interval in table 4.6. We select this interval in order to have

TABLE 4.6: Time interval second crossing

t_1	$2015-10-03T14:47:11.50Z$
t_2	$2015-10-03T14:47:18.00Z$

a signal as monotone as possible with two regions of constant signal at the edges. The problems in the individuation of the minimum variance direction are clear if we look at the maximal eigenvalues ratio:

$$\left(\frac{\lambda_2}{\lambda_3}\right)_{max} = 4.65 \tag{4.4}$$

$$\left(\frac{\lambda_1}{\lambda_2}\right)_{max} = 4.95 \tag{4.5}$$

The value of $\frac{\lambda_2}{\lambda_3} < 5$ for all the four spacecraft and so the direction of the eigenvector $\mathbf{v}_3$ is not a perfectly reliable indicator of the normal direction. Anyway, even in this case, similar normal directions are obtained from all the four spacecraft. The results are collected in table 4.7.

The mean normal direction is $\hat{\mathbf{n}}_{MVA} = (-0.43,\ 0.85,\ 0.31)$. We perform the same computation of section 4.1.1 in order to find the complete local frame for the second magnetopause crossing, table 4.8. As it can be seen in the picture 4.9 there is a difference between the direction normal to the discontinuity in the first and in the second crossing, the angle between the two directions is $\theta \sim 100°$. On the other side, we can notice that the normal measured in the two cases from the four spacecraft have a good agreement. In particular, we can compute the angle between the different vectors, they are collected in the table 4.9.

Looking at table 4.9, we can notice that the angles between the normals computed from the different spacecraft in both the analyzed crossings are really small, so the results from the four observation points are in good agreement. As said before, the ratio between the eigenvalues is not optimal during the second crossing. Still, looking at the data we can notice that the y

TABLE 4.7: Eigenvectors obtained with the MVA method and their angular incertitudes in the second crossing

	$mms1$	$mms2$	$mms3$	$mms4$
$\mathbf{v}_1$	$(0.63, 0.02, 0.78)$	$(0.62, 0.03, 0.78)$	$(0.62, 0.02, 0.78)$	$(0.62, 0.02, 0.79)$
$\mathbf{v}_2$	$(0.66, 0.51, -0.55)$	$(0.62, 0.60, -0.52)$	$(0.68, 0.49, -0.55)$	$(0.66, 0.52, -0.54)$
$\mathbf{v}_3$	$(-0.41, 0.86, 0.31)$	$(-0.48, 0.80, 0.35)$	$(-0.39, 0.87, 0.29)$	$(-0.41, 0.86, 0.31)$
$\lvert\Delta\phi_{13}\rvert$ (rad)	0.0026	0.0032	0.0023	0.0023
$\lvert\Delta\phi_{23}\rvert$ (rad)	0.0198	0.0338	0.0189	0.0203
$\lvert\Delta\phi_{12}\rvert$ (rad)	0.0027	0.0032	0.0024	0.0024

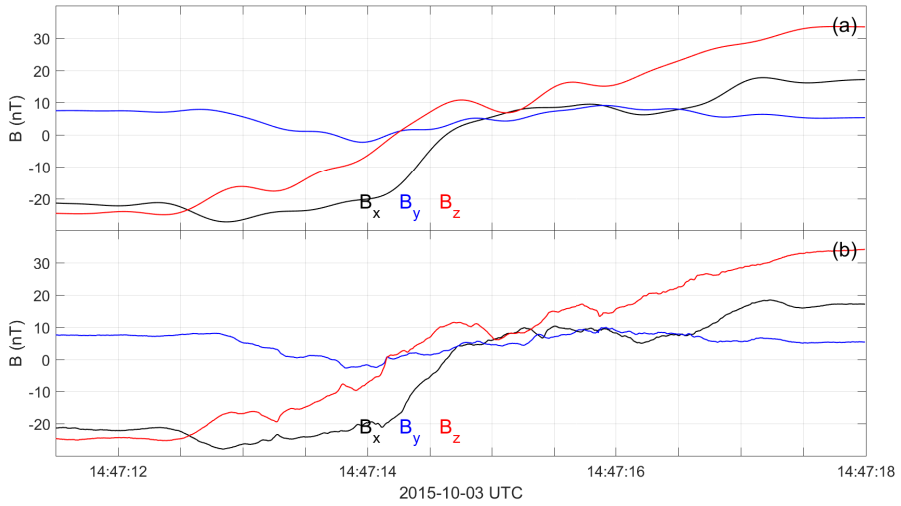

FIGURE 4.8: The three components of **B** from MMS1, second complete magnetopause crossing. The first panel shows the signal after the action of the low-pass filter with $f_{max} = 2\ Hz$, the second panel shows the 'raw' signal.

l	$(0.61,\ 0.02,\ 0.79)$
m	$(0.67,\ 0.53,\ -0.52)$
n	$(-0.43,\ 0.85,\ 0.31)$

TABLE 4.8: LMN frame for the second crossing

component of the field is the one that changes less compared to the others so we can infer, by inspection, that the normal direction will have a predominant component along this axis. This is coherent with the results.

We conclude that the magnetopause is moving fast and in a way that does not allow us to define a single local frame able to describe the discontinuity along the entire interval containing two crossings. We define a local frame for the first crossing ($\mathbf{l}_1,\ \mathbf{m}_1,\ \mathbf{n}_1$), table 4.5 and a local frame for the second ($\mathbf{l}_2,\ \mathbf{m}_2,\ \mathbf{n}_2$), table 4.8.

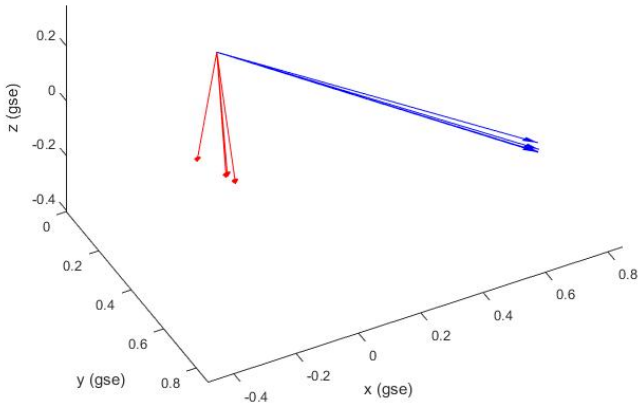

FIGURE 4.9: 3D representation of the normals computed from the four satellites for the two different crossings. The blue fleshes are the normals from the first crossing, the red ones from the second.

TABLE 4.9: Angle between the normal direction computed from different spacecrafts in the first magnetopause crossing. Spacecraft 1 is taken as the reference one and ϕ_{1i} with $i = 2, 3, 4$ indicates the angle between the normal direction computed by spacecraft 1 and spacecraft i.

crossing time	$\phi_{12}(^\circ)$	$\phi_{13}(^\circ)$	$\phi_{14}(^\circ)$
14 : 47 : 00	1.7339	1.7026	0.4548
14 : 47 : 15	0.6912	0.6838	0.4684

4.2 Timing method

On of the most important features of the MMS mission is that it is composed by a constellation of spacecraft. This allows on one side to have four different measures of the same quantity, on the other side to adopt multi-spacecraft methods of analysis that leads us to have a better comprehension of the data. This is the case of the *timing* method. Its theoretical basis is explained in section 2.1.3, here an explication about how we obtained the normal direction is proposed. First of all, the timing method gives the component of velocity's discontinuity parallel to the normal knowing the spacecraft positions and the instants in which the discontinuity passes through each spacecraft. Once obtained that, we can compute the normal direction with a simple normalisation.

Adopting the same notation of chapter 2 the timing method gives the vector $\mathbf{m} = \frac{\hat{\mathbf{n}}}{V}$ as an output. We have to remind that the timing method is based on two fundamental assumptions: the discontinuity is plane and it moves with constant velocity. The first hypothesis is not so ambitious because in the considered intervals of time the separation between the spacecrafts is

$\sim 25km$ (much smaller that the characteristic length of the involved structures), while the second one has to be taken with care. In addiction, since the spacecrafts are moving with a velocity of the order of 1 km/s they can be considered as immobile compared to the discontinuity since typical values of magnetopause's velocity are $\sim 10 - 100km/s$.
We assume that the magnetic field signal seen by the four satellites is not changing its shape in time: the current sheet is only moving through the constellation. The same signal is seen from the first spacecraft that meets the discontinuity and then from the other components of the constellation in an order that depends on the tetrahedron configuration and on the orientation of the discontinuity.

The first problem is to find the instants of the crossing. Once individuated the crossing time of the first satellite, according to the hypothesis, the other signals correspond to the first signal shifted in time. Our purpose is to compute these shifts Δt_{1i} with $i = 2, 3, 4$, choosing spacecraft 1 as the reference one. This can be done using the notion of cross correlation, or, in this case, of autocorrelation with the signals, initially not superpose.
For continuous functions f and g, the cross-correlation is defined as:

$$(f \star g)(\tau) \ = \int_{-\infty}^{\infty} f^*(t)\ g(t+\tau)\, dt, \tag{4.6}$$

where f^* denotes the complex conjugate of f and τ is the lag. Similarly, for discrete functions, the cross-correlation is defined as:

$$(f \star g)[n] \ = \sum_{m=-\infty}^{\infty} f^*[m]\ g[m+n]. \tag{4.7}$$

In our condition, we deal with real functions ($f^* = f$) and $f = g$. Cross correlation is then a functional depending on τ: we want to find the value of the lag τ that maximises the cross correlation integral. Furthermore, we can notice that an equivalent approach is finding the lag τ that minimises the quantity

$$S(\tau) = \sum_{m=-\infty}^{\infty} |f[m] - g[m+n]|^2 \tag{4.8}$$

In our routine we use this second approach.
The data are preliminary treated with a selection of the time interval and also a smoothing procedure in order to eliminate all short period fluctuations associated with wave disturbances, so that only large-scale variations remain. The choice of the time interval is delicate since the magnetic field is supposed to evolve in a monotone way ($\mathbf{B}_{theory} \propto \mathbf{B}_0 \tanh(t - t_{cs})$) so we should chose an interval that contains the inversion of the magnetic field (as well as the current sheet) but that does not contain other structures. If we consider the second magnetopause crossing centered in $t_{cs,2} = 2015 - 10 - 03T14 : 47 : 15.00Z$, as we have already underlined before, there is a low frequency fluctuation that makes the signal non monotone in an interval. This can leads to larger Δt_{1i} uncertainties.
In figures 4.10 and 4.11 the segments of the signals chosen for the timing are showed. We propose only the z component of the magnetic field because even if all the components change sign in this interval, the z component has the most clear monotone behaviour. The results from the

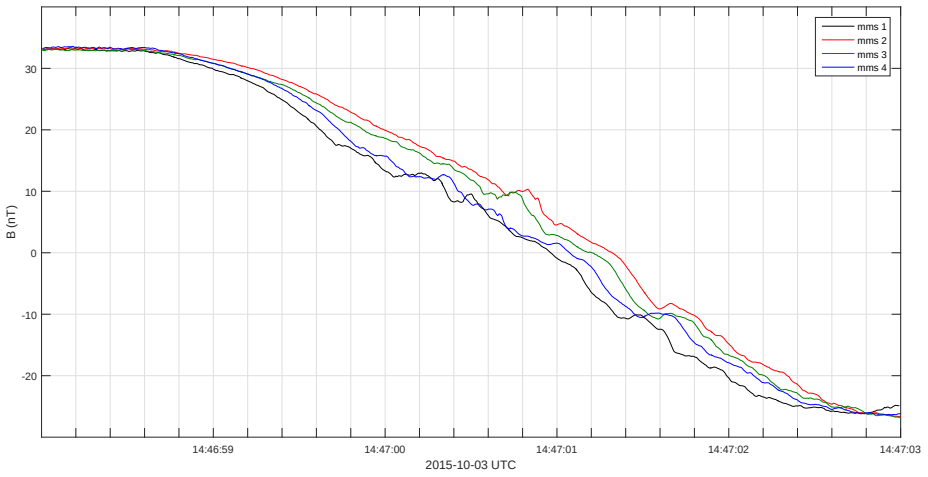

FIGURE 4.10: B_z of the four spacecraft in the interval selected for the *timing* during the first crossing.

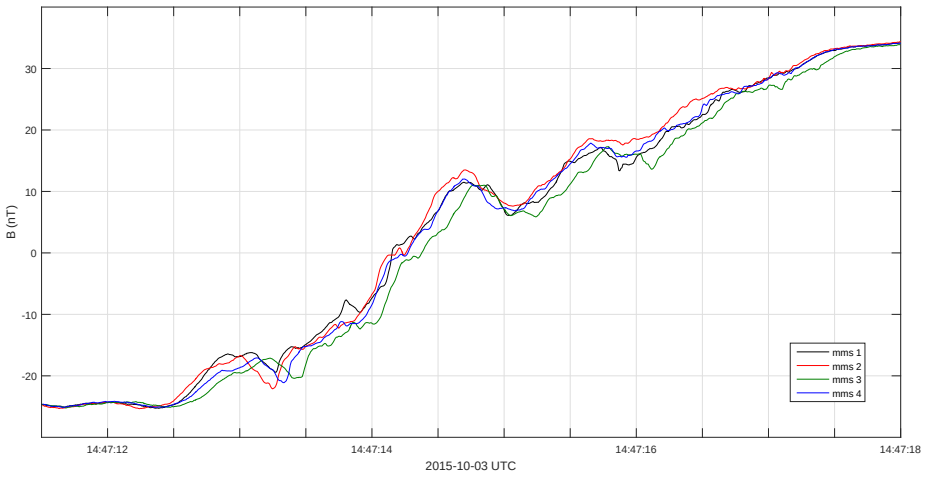

FIGURE 4.11: B_z of the four spacecraft in the interval selected for the *timing* during the second crossing.

cross-correlation based routine are showed in pictures 4.12 and 4.13. Tables 4.10 and 4.11 present the delays obtained through the cross correlation. We notice that in the second crossing Δt_{ij} have big uncertainties. This is due to the lack of monotony of the signal. In addiction, we can see that the error on $\Delta t_{14} > 100\%$. The cause may be the method of error's calculation [1] added to the fact that the two signals are already well superposed before the shift.

To evaluate the goodness of the found delays we can shift each signal of the related delay and see if the superposition with the data from MMS1 is good. Figures 4.12 and 4.13 show the signals as they are recorded by the spacecraft and then the same signals after the application of the shifts.

[1] the error δt_{ij} of the delay Δt_{ij} is defined as the difference between the time when the minimum of the quantity S (defined in 4.8) is reached and the time when S doubles its minimal value.

TABLE 4.10: Time delays in the first crossing.

Δt_{12}	$-0.310 \pm 0.045\ s$
Δt_{13}	$-0.209 \pm 0.069\ s$
Δt_{14}	$-0.116 \pm 0.097\ s$

TABLE 4.11: Time delays in the second crossing.

Δt_{12}	$0.060 \pm 0.084\ s$
Δt_{13}	$-0.135 \pm 0.082\ s$
Δt_{14}	$-0.005 \pm 0.067\ s$

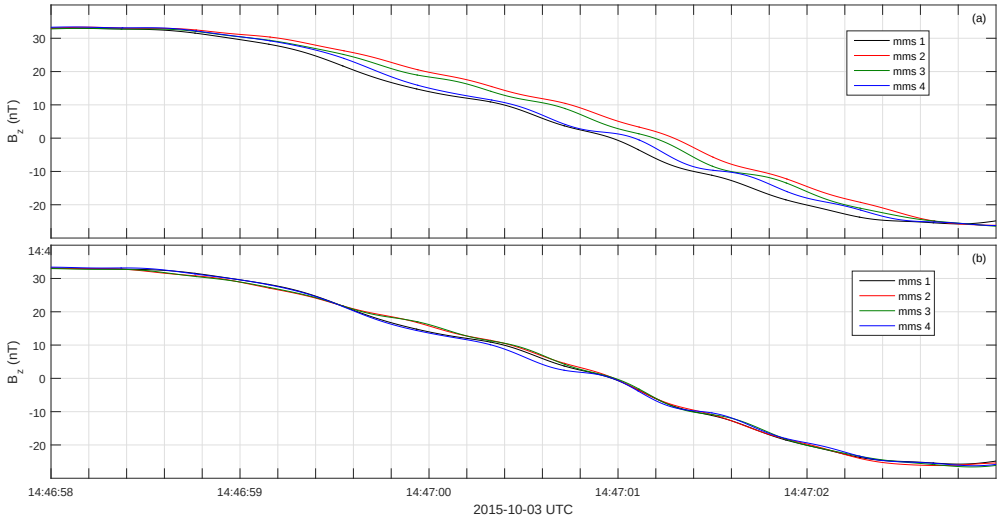

FIGURE 4.12: B_z signals from the four spacecraft in the first magnetopause crossing. Panel (a) shows them as obtained from the measures and panel (b) shows them after applying the shifts computed with the crosscorrelation method. A low-pass filter with $f_{max} = 2\ Hz$ has been applied.

Once we obtained the delays, we are able to compute the normal direction and the corresponding component of the velocity following section 2.1.3. We obtain the results listed in table 4.12.

In figures 4.14 and 4.15 we show a comparison between the mean of the normal direction computed by the four spacecraft data using the MVA method and the normal computed with the *timing* method for the first magnepause crossing. We can see that in the first case the two results

TABLE 4.12: Normal component of magnetopause velocity and normal direction to magnetopause computed with the *timing* method for the two crossings. Velocities errors are $\sim 20\%$.

crossing time	$\hat{\mathbf{n}}$	$\lvert\mathbf{V}_n\rvert(km/s)$
$14:47:00$	$(-0.853,\ -0.324,\ 0.406)$	79.57
$14:47:15$	$(-0.073,\ 0.997,\ 0.016)$	122.38

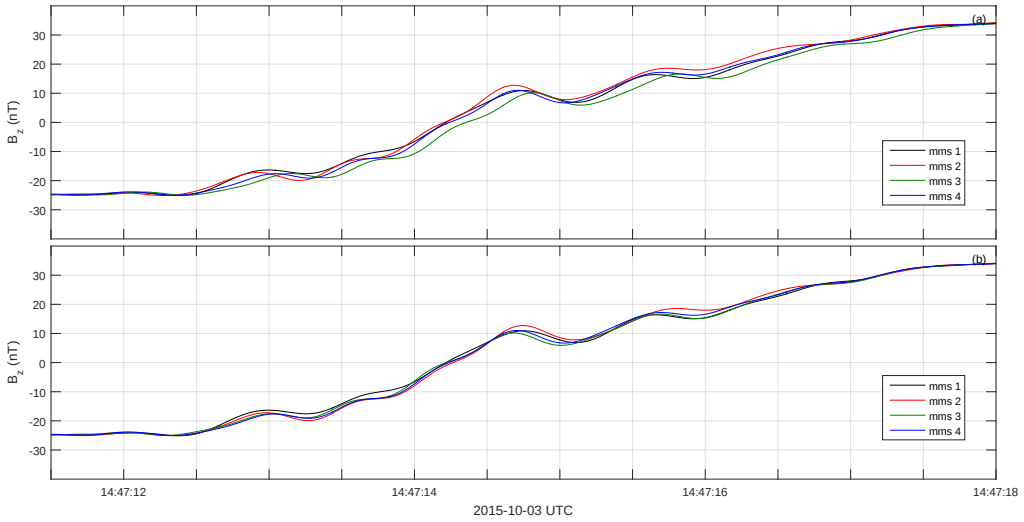

FIGURE 4.13: B_z signals from the four spacecraft in the second magnetopause crossing. Panel (a) shows them as obtained from the measures and panel (b) shows them after applying the shifts computed with the cross correlation method. A low-pass filter with $f_{max} = 2\ Hz$ has been applied.

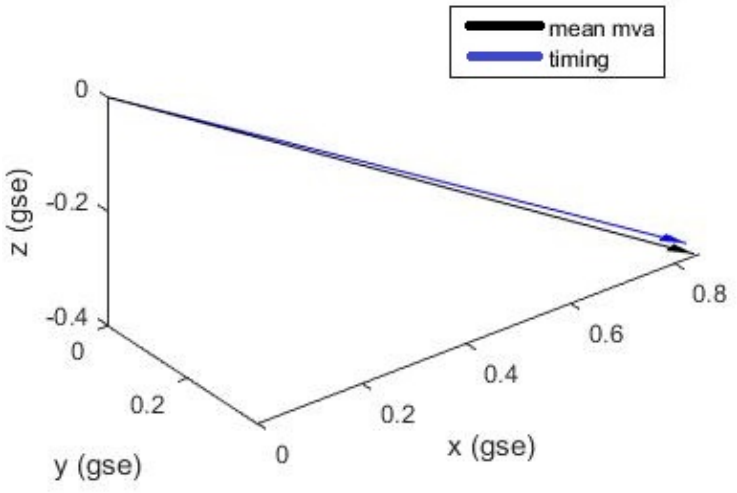

FIGURE 4.14: Mean normal direction computed by the four spacecraft data using the MVA method and normal computed with the *timing* method for the first magnepause crossing

are quite similar, the angle θ between the two directions being $\theta \sim 2°$. In the second crossing the angle is wider, $\theta \sim 30°$.

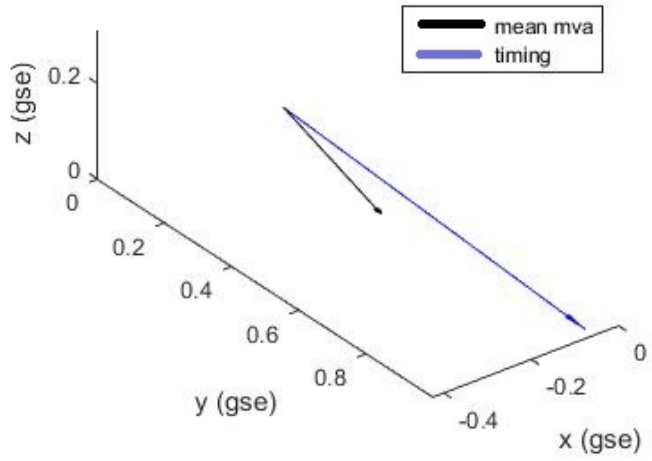

FIGURE 4.15: Mean normal direction computed by the four spacecraft data using the MVA method and normal computed with the *timing* method for the second magnepause crossing

4.2.1 Magnetopause width

In the hypothesis of $v_{spacecraft} \ll v_{MP}$, knowing the velocity of the boundary let us know its width. From the magnetic field data we can estimate that the time needed to the boundary to cross the constellation is $\sim 6\ s$, so we can say that the magnetopause width is $d_{MP} \sim 400\ km$ for the first crossing and $d_{MP} \sim 720\ km$ for the second crossing. This distances correspond to $d_{MP} \sim 6\lambda_i$ and $d_{MP} \sim 10\lambda_i$, in ion scales (see 4.13).

TABLE 4.13: Ion and electrons characteristic lengths: gyroradius and skindepth.

	magnetosheath	*magnetosphere*
$\rho_i(km)$	70	130
$\lambda_i(km)$	70	140
$\rho_e(km)$	0.5	0.5
$\lambda_e(km)$	2	3

4.3 Local LMN frames

The analysis carried out in the previous sections leads to two different set of vectors for each crossing that can be used as local frame in order to describe the magnetopause. In fact, the MVA method directly gives a set of orthogonal vectors; the timing method yields only the

normal direction but it is easy to compute a vector orthogonal to it and then complete the set. We obtained a good agreement between the results from the timing method and the MVA for the first crossing, so we adopt the set LMN yield by the MVA method as the magnetopause's local frame for the first crossing. We already underlined in section 4.1.2 that the situation is different for the second crossing: the magnetic field signal is not monotone and this leads to inaccurate results. This is true also for the timing method. Comparing figure 4.13 and 4.12 we can notice how the superposition of the signals is better in the first crossing. Since one of the signal's features required by the timing method is the monotone evolution we apply it to the density's data within a proper interval. The results are shown in figure 4.16. In this case, $\hat{\mathbf{n}} = (-0.314,\ 0.904,\ -0.290)$ and $|\mathbf{V}_n| = 121$ with an error of the 20 %. Another aspect to take into account is that the component of electric field tangential to the boundary has to be conserved across the boundary. Since this request is better fulfilled if we choose the LMN system yield by the timing method applied to the density, we adopt it as the LMN frame for the second crossing.

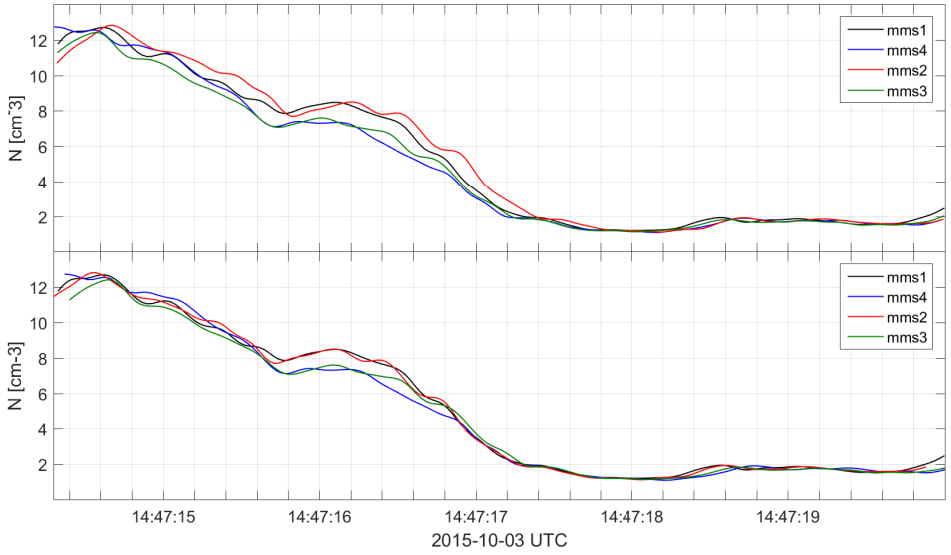

FIGURE 4.16: Density signals from the four spacecraft in the second magnetopause crossing. Panel (a) shows them as obtained from the measures and panel (b) shows them after applying the shifts computed with the crosscorrelation method. A low-pass filter with $f_{max} = 2\ Hz$ has been applied.

In conclusion, we are able to define the two LMN set that will be used in the following (table 4.14 and 4.15).

$\mathbf{l}_1$	$(0.33,\ 0.22,\ 0.92)$
$\mathbf{m}_1$	$(0.43,\ -0.90,\ 0.06)$
$\mathbf{n}_1$	$(0.84,\ 0.38,\ -0.40)$

TABLE 4.14: LMN frame for the first crossing

$\mathbf{l}_2$	$(0.76,\ 0.20,\ 0.61)$
$\mathbf{m}_2$	$(0.63,\ 0.00,\ -0.78)$
$\mathbf{n}_2$	$(-0.15,\ 0.98,\ -0.12)$

TABLE 4.15: LMN frame for the second crossing

4.4 deHoffmann-Teller method

The *deHoffmann-Teller* method has been widely explained in section 2.1.2. In this section we report just the results, listed in table 4.16 and 4.17. The method is applied, as the others in this chapter, to the two different intervals containing the first and the second magnetopause crossing used in the previous sections.

TABLE 4.16: Velocity of the *deHoffmann-Teller* frame of the first crossing.

S/C	$\mathbf{V}_{HT}\ (km/s)$	$\Delta\mathbf{V}_{HT}\ (km/s)$
$mms1$	$(-99.2,\ 133.5,\ 55.5)$	$(4.4,\ 6.1,\ 9.0)$
$mms2$	$(-83.4,\ 136.3,\ 69.8)$	$(4.7\ 7.5,\ 11.0)$
$mms3$	$(-98.0,\ 134.2,\ 57.1)$	$(5.0,\ 7.7,\ 11.3)$
$mms4$	$(-87.7,\ 131.5,\ 60.4)$	$(4.1,\ 5.7,\ 8.6)$
$average$	$(-92.1,\ 133.9,\ 60.7)$	$(9.1,\ 13.6,\ 20.0)$

TABLE 4.17: Velocity of the *deHoffmann-Teller* frame of the second crossing.

S/C	$\mathbf{V}_{HT}\ (km/s)$	$\Delta\mathbf{V}_{HT}\ (km/s)$
$mms1$	$(-201.2,\ 109.7,\ -55.6)$	$(6.2,\ 3.1,\ 7.3)$
$mms2$	$(-191.3,\ 104.3,\ -48.8)$	$(6.5,\ 3.3,\ 7.8)$
$mms3$	$(-197.5,\ 110.3,\ -51.1)$	$(6.2,\ 3.1,\ 7.2)$
$mms4$	$(-193.9,\ 106.1,\ -46.5)$	$(6.7,\ 3.4,\ 7.9)$
$average$	$(-196.0,\ 107.6,\ -50.5)$	$(12.8,\ 6.4,\ 15.1)$

Knowing $\mathbf{V}_{HT}$ is interesting since we can compute the normal component of the velocity of the magnetopause. Applying Eq. 2.18 we find the results listed in table 4.18. They appear to agree within the error bars with the discontinuity's velocities found with the timing method (table 4.12).

TABLE 4.18: Normal component of magnetopause velocity and normal direction to magnetopause computed from $\mathbf{V}_{HT}$.

crossing time	$\lvert\mathbf{V}_n\rvert(km/s)$
14 : 47 : 00	97.3 ± 11.7
14 : 47 : 15	141.8 ± 17.2

Considering the same approximations of section 4.2.1 and referring to the table 4.13 we estimate that the magnetopause width is $d_{MP} \sim 8\ d_i$ for the first crossing and $d_{MP} \sim 12\ d_i$ for the second crossing.

4.5 Current density computation

As already explained in section 2.2, with MMS data we are able to obtain the current density in two different ways: a current $\mathbf{J}_p$, obtained with the data of the *FPI* instrument, given by the Eq. 2.40 and a current obtained via the curlometer technique, given by the Ampère equation Eq. 2.41. In this section the results of the two approaches are shown. This comparison is important because it underlines the new potentialities of the MMS data: with a temporal resolution of 30 ms for electrons and 150 ms for ions we are able to know all the fluctuations of the density current signal. On the other side, we can analyse the difference between the curlometer result and the particles result.
In figure 4.1 we can see that the Tetrahedron Quality Factor is $TQF = 0.95$, this means that the constellation is about to be a regular tetrahedron. Furthermore, since the spacecraft separation is about 25 km we can say that it is much smaller than the characteristic dimension of the region of the current (the width of the magnetopause has been computed in section 4.2.1). In that way, all the conditions to obtain a good estimation of the current via the curlometer technique are fulfilled, we can expect a good agreement between the current density computer with the curlometer and the one computed with the particles velocities.

In figure 4.17 we can notice that the quality factor $\propto \nabla \cdot \mathbf{B}$ is always extremely small, the highest value is $\sim 3\ 10^{-9}$ and it occurs in the interval with a current almost zero. This higher factor can be more likely due to the fact that $\nabla \times \mathbf{B} \sim 0$ in that interval and not to a real change in the value of the divergence. The good result obtained with the curlometer is also shown in figures 4.18 and 4.19. The comparison is clearer in figure 4.19 where we see the three components of $\mathbf{J}$ separately. Discrepancies between the two signals that seems not due to the different resolution is seen in the x component, in the interval $14:47:14 - 14:47:16 UTC$ and in the z component in the interval $14:47:03 - 14:47:06 UTC$. This can indicate that there are current structures with widths below the spacecraft separation and they can not be well reproduced with the curlometer technique. Nevertheless, the global behaviour of the current density computed with the curlometer and the particles data is, to a good approximation, the same.

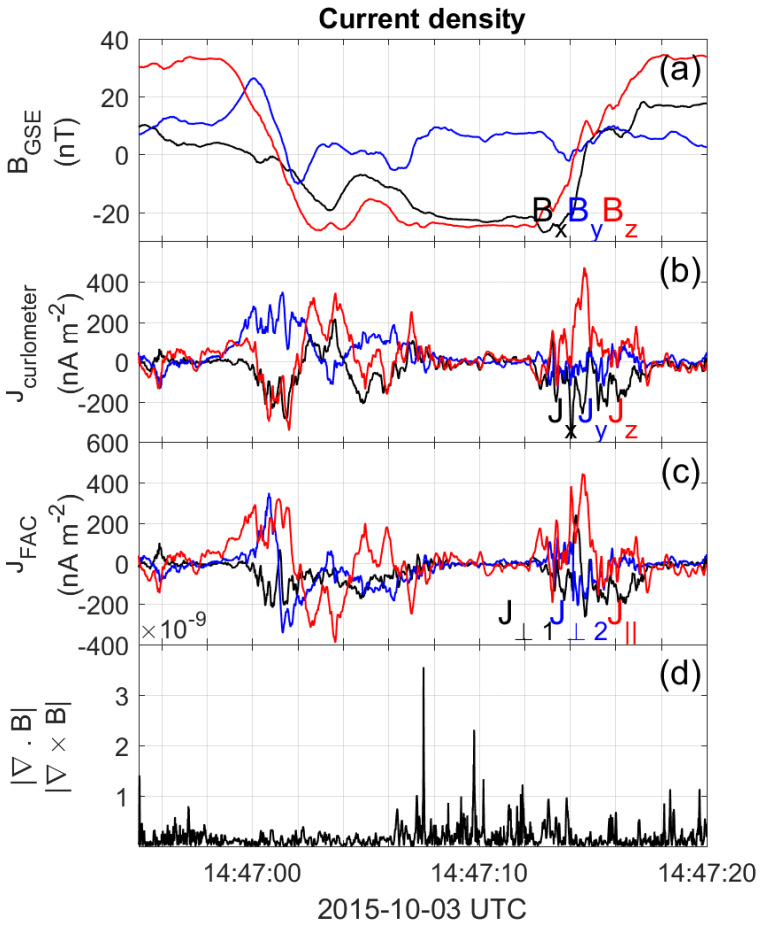

FIGURE 4.17: (*a*) The magnetic field, average on the four spacecraft. (*b*) The current density computed via the curlometer in the GSE system. (*c*) The current density computed via the curlomenter represented in a system with one direction along **B** and the other two directed perpendicularly to **B**. (*d*) The current quality factor $\frac{\nabla \cdot \mathbf{B}}{\nabla \times \mathbf{B}}$.

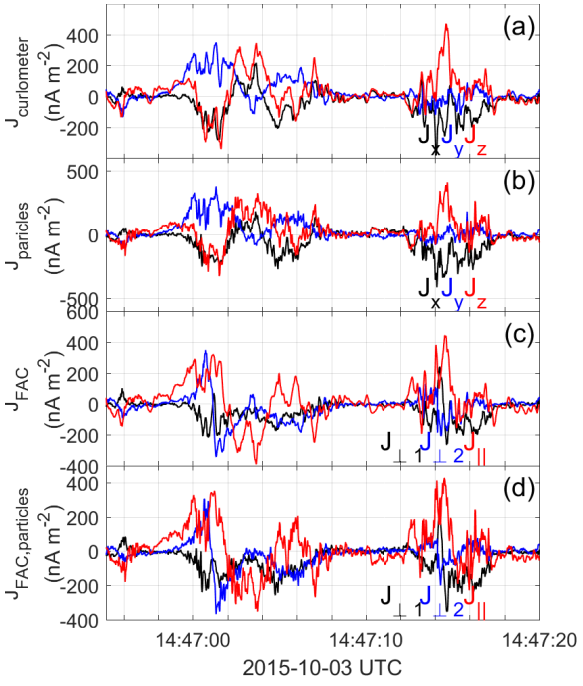

FIGURE 4.18: (*a*) and (*c*) Current densities computed with the curlometer technique, in GSE frame and in the system of coordinates with axes parallel and orthogonal to **B**.. (*b*) and (*d*) Current densities computed with the particles data, GSE frame and in the system of coordinates with axes parallel and orthogonal to **B**.

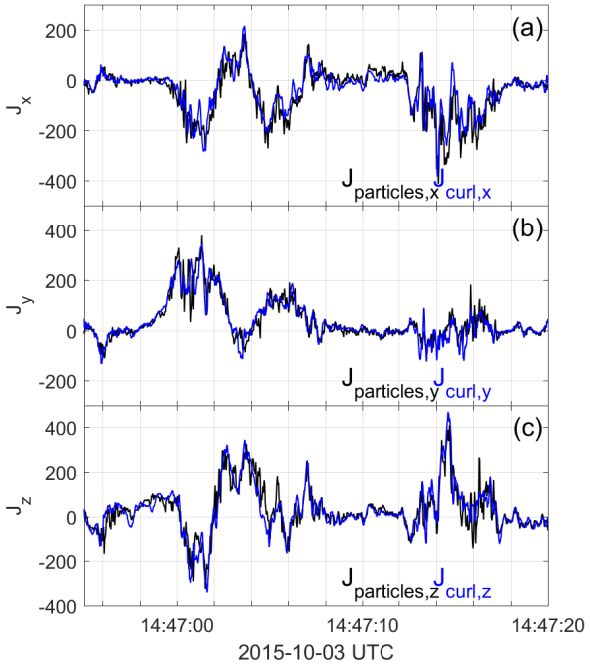

FIGURE 4.19: (*a*) x-component of $\mathbf{J}_p$ and $\mathbf{J}_{curl}$. (*b*) y-component of $\mathbf{J}_p$ and $\mathbf{J}_{curl}$. (*c*) z-component of $\mathbf{J}_p$ and $\mathbf{J}_{curl}$. The unit is always nA/m^2.

Chapter 5

Electric field calibration

This short chapter contains the re-calibration that has been operated on the electric field data. During the data analysis, we realised the presence of an offset in the electric field that needed to be fixed. In fact, in the magnetosheath region, an almost constant gap was present between the electromagnetic velocity computed with the *l2* electric field data and the velocity obtained with the *FPI* instrument, directly from the particles data. The presence of such a gap would have meant that the particles were decoupling from the magnetic field. Since there was no reason for this to happen in that region we concluded that it was the result of a calibration problem. In the following we illustrate in details the calibration procedure we adopted to fix this problem.

In order to analyse the electric field, level *l2* data from the *EDP* instrument have been used. We see that there is a calibration problem which is enlightened by the fact that in the magnetosheath, where the ideal MHD holds, we find that the relation $\mathbf{v}_{i,\perp} = \mathbf{v}_{e,\perp} = \frac{\mathbf{E}\times\mathbf{B}}{B^2}$ is not valid even if there are no currents neither other reasons to explain the particles decoupling from the magnetic field. This can be seen in figure 5.1, where the yellow rectangle includes an interval of time where the MMS constellation was in the magnetosheath. It is clear that there is an offset in the measurements and that it is not due to a physic effect. In this computation $\mathbf{v}_i$ and $\mathbf{v}_e$ are obtained from the *FPI* instrument. For our analysis, we assume that *FPI* is able to give *magnetosheath* measurements which are more reliable than the ones coming from the *EDP* instrument. This hypothesis is supported by some specific feature of the *FPI* instrument. Its energy range is $10\ eV - 30\ keV$ so the cold ions (ions with energy of $1\ eV$ or less) are not measured by this instrument. However, cold ions are almost not present in the magnetosheath, as well as particles with energy that exceeds $30\ keV$, [36], [37] [1]. Furthermore, the magnetosheath usually does not host important gradients in pressure, temperature and density and the values of the last two quantities are relatively big compared to the ones present in the magnetosphere. Also, we have seen in figure 4.19 that there is a good agreement between the current density computed with

[1] We have to precise that this last statement is only partially true. Recent studies as the one presented in [38] show that cold ions may be detected at magnetoheath and magnetopause and that they can also have a role in the magnetic reconnection process.

the curlometer technique and with the data from *FPI*. This is a confirmation of our hypothesis. So, we state that the electric field data of level *l*2 need to be calibrated. In the following of this chapter we will look for the most suitable offsets to apply to the electric field components in order to re-establish the physic condition of non-decoupling in the magnetosheath.

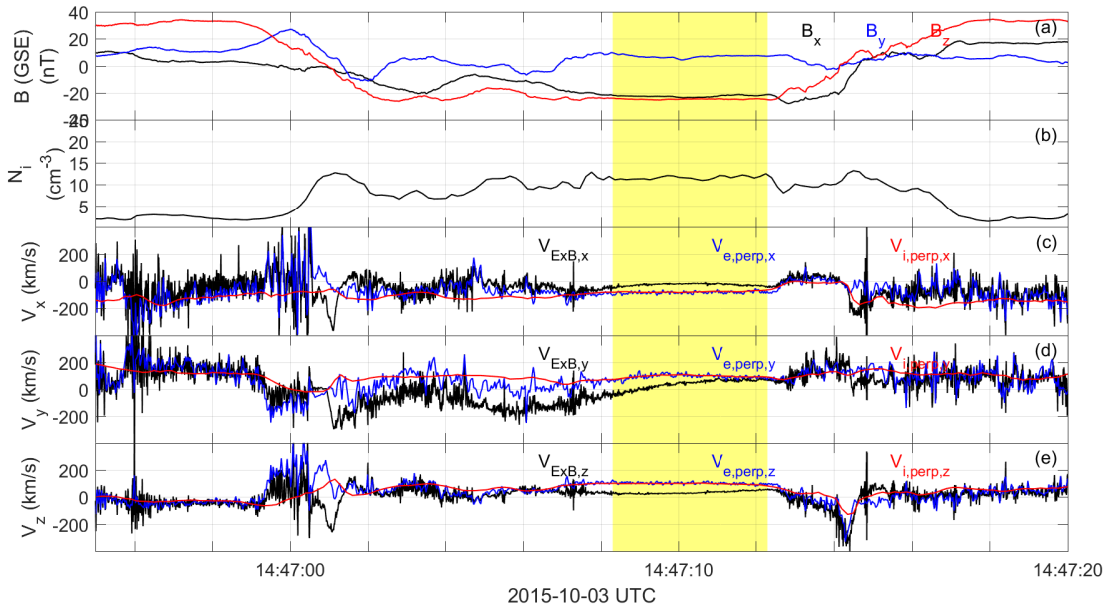

FIGURE 5.1: In panel (a) the three component of the magnetic field in the GSE frame are shown. In panel (b) we have the ion density. In panel (c), (d) and (e) we compare the velocity $\mathbf{E} \times \mathbf{B}/B^2$ with the ion and electron perpendicular velocities (referred to the magnetic field). The yellow rectangle indicates an interval of time $(14:47:08.30 - 14:47:12.30)$ where the MMS constellation was in the magnetosheath. All the data are from MMS1, the same behaviour is seen also by the other spacecraft.

The reader has to be aware that the definition of this offsets has different error sources that will be underlined all along the chapter. First of all, we need to add the proper offset to a 'raw' set of data. Data of level *l*2 already contain some default calibrations they are not suitable for our need. For this reason we start our calibration using the electric field data of level *l*2_*pre*. In this files, data are only given in the spacecraft de-spun frame. Since the angle between the ecliptic and the MMS orbit plane has a maximal value of 3°, we will approximate the spacecraft de-spun frame to the GSE frame. Furthermore, since measurements of E_z are given by the Axial Double Probe while measurements of E_x and E_y are given by the Spin-Plane Double Probe, we try to modify only the x and y components. The z component of the final electric field will be computed lastly using the relation $\mathbf{E} \cdot \mathbf{B} = 0$. Then, even if the standard calibration process involves two kind of parameters (an offset and a multiplying factor, see Appendix B), we will look only for the offset and we will set the multiplying factor to 1.

As said before, our goal is to fix the gap that can be clearly seen in the yellow-shadowed interval in figure 5.1, in other words we want to define new offsets for the electric field component in order to have

$$v_{i,\perp,x} = \left(\frac{\mathbf{E} \times \mathbf{B}}{B^2} \right)_x = \frac{E_y B_z - E_z B_y}{B^2}$$

$$v_{i,\perp,y} = \left(\frac{\mathbf{E}\times\mathbf{B}}{B^2}\right)_y = \frac{E_z B_x - E_x B_z}{B^2} \tag{5.1}$$

$$v_{i,\perp,z} = \left(\frac{\mathbf{E}\times\mathbf{B}}{B^2}\right)_z = \frac{E_x B_y - E_y B_x}{B^2}$$

in the magnetosheath. We can write the same relations also for $\mathbf{v}_{e,\perp}$. Of course, every velocity component depends on two components of the electric and magnetic field but this means that we have to handle two different offsets at a time. So, as a first step in the calibration process we define a new electric field with $E_z = 0$, $\mathbf{E}' = (E_x, E_y, 0)$, and we approximate $\mathbf{E}$ with $\mathbf{E}'$. In that way

$$v_{i,\perp,x} = \left(\frac{\mathbf{E}'\times\mathbf{B}}{B^2}\right)_x = \frac{E_y B_z}{B^2}$$

$$v_{i,\perp,y} = \left(\frac{\mathbf{E}'\times\mathbf{B}}{B^2}\right)_y = \frac{-E_x B_z}{B^2} \tag{5.2}$$

$$v_{i,\perp,z} = \left(\frac{\mathbf{E}'\times\mathbf{B}}{B^2}\right)_z = \frac{E_x B_y - E_y B_x}{B^2}$$

This is not a good approximation since E_z is not zero in the selected interval and if we compute the mean value of each component we see that they have amplitudes of the same order: $|\overline{E_x}| \sim 1.2\ mV/m$, $|\overline{E_y}| \sim 2.8\ mV/m$ and $|\overline{E_z}| \sim 0.5\ mV/m$. However, this is just the first step, preparatory for the following.

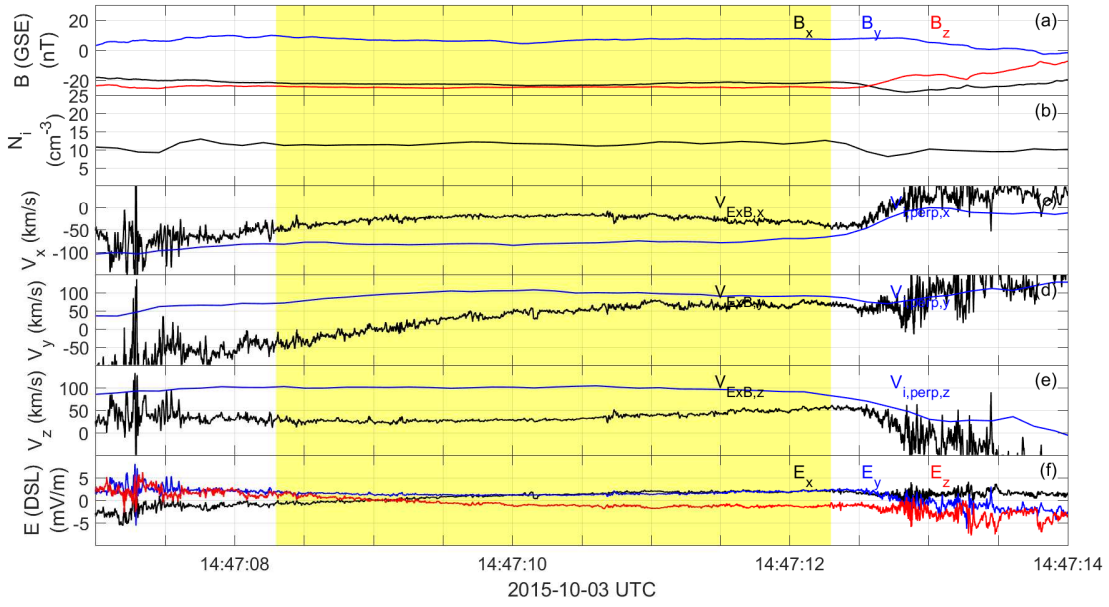

FIGURE 5.2: Zoom of figure 5.1 in the interval $14:47:07.30 - 14:47:14.30$. The electron velocity is not shown anymore since in this region it is equal to the ion velocity. In panel (f) the three components of the electric field from the level *l2_pre* are shown.

We use an iterative and empiric approach: we set an offset for E_y, called ΔE_y and one for E_x, called ΔE_x. Then we compute the RHS of Eq. 5.2 with the new values of E_x and E_y. We change the offsets until we find *by eye* the best match between the components of $\mathbf{v}_{i,\perp}$, $\mathbf{v}_{e,\perp}$ and $\frac{\mathbf{E}'\times\mathbf{B}}{B^2}$. In particular, we see from Eq. 5.2 that the offset on E_x (E_y) influences $v_{i,\perp,y}$ ($v_{i,\perp,x}$). Therefore, the strategy is:

- set ΔE_x, compare $v_{i,\perp,y}$, $v_{e,\perp,y}$ and $\left(\frac{\mathbf{E}'\times\mathbf{B}}{B^2}\right)_y$ and change ΔE_x until we find the best match;
- set ΔE_y, compare with $v_{i,\perp,x}$, $v_{e,\perp,x}$ and $\left(\frac{\mathbf{E}'\times\mathbf{B}}{B^2}\right)_x$ and change ΔE_y until we find the best match;
- compare $v_{i,\perp,z}$, $v_{e,\perp,z}$ and $\left(\frac{\mathbf{E}'\times\mathbf{B}}{B^2}\right)_z$ (where E_x and E_y are both present).

In table 5.1 we list the offsets ΔE_x and ΔE_y found for each spacecraft in the approximation $E_z = 0$ while in figure 5.3 we show the results obtained by applying the offsets on the electric field and recalculating $\left(\frac{\mathbf{E}'\times\mathbf{B}}{B^2}\right)$ for one of the spacecraft, MMS1. Figure 5.3 is meant to describe our calibration's result, we obtained the same behaviour for the other spacecraft.

We assign an error of $\pm$ 0.5 mV/m to both the offsets and we consider the chosen offset as good when we reach a gap < 20 km/s between $\mathbf{v}_{i,perp}$ and the calibrated $\left(\frac{\mathbf{E}'\times\mathbf{B}}{B^2}\right)$. In fact, the errors on velocities are between 10 % and 20 % and the speed is ~ 100 km/s for all the velocity components. Furthermore, in figure 5.3 (and in the following) we have plotted the ion but not the electron velocity. This is done in order to have an image easy to read; ion and electron velocities are the same within the error bars so no information is lost in these images.

TABLE 5.1: Offsets of the E_z and E_y for each spacecraft in the approximation $E_z = 0$.

	ΔE_x (mV/m)	ΔE_y (mV/m)
$mms1$	3.5	1.2
$mms2$	3.8	1.2
$mms3$	3.4	1.4
$mms4$	3.8	1.4

Now that we have a set of preliminary offset we repeat the same procedure with an electric field $\mathbf{E}''$ having the z component computed from $\mathbf{E}\cdot\mathbf{B} = 0$. Also in this case, we assign an error of $\pm$ 0.5 mV/m to both the offsets and we consider the chosen offset as good when we reach a gap < 20 km/s between $\mathbf{v}_{i,perp}$ and the calibrated $\left(\frac{\mathbf{E}''\times\mathbf{B}}{B^2}\right)$. The obtained results for ΔE_x and ΔE_y are shown in table 5.2 while in 5.4 is presentend a new comparison between the components of $\mathbf{v}_{i,perp}$ and the calibrated components of $\left(\frac{\mathbf{E}''\times\mathbf{B}}{B^2}\right)$.

Figures 5.2, 5.3 and 5.4 present the data in the same interval of time in order to make the comparison between the uncalibrated and the calibrated electric field as simple as possible. Applying the offsets that we have been defining in this chapter allows to establish the physic condition of

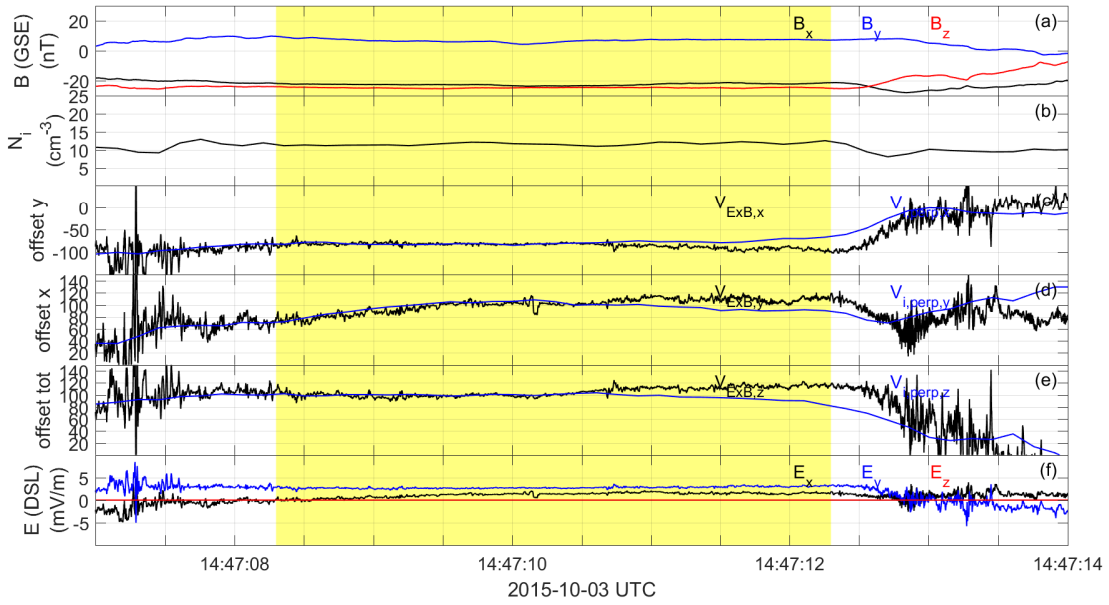

FIGURE 5.3: All data from MMS1. *(a)* The three components of the magnetic field. *(b)* The particles density. *(c)* Comparison between the electromagnetic velocity and the perpendicular (to the magnetic field) ion velocity, x component. $v_{E\times B,x}$ contains the new electric field with the offset on E_y. *(d)* Comparison between the electromagnetic velocity and the perpendicular (to the magnetic field) ion velocity, y component. $v_{E\times B,y}$ contains the new electric field with the offset on E_x. *(e)* Comparison between the electromagnetic velocity and the perpendicular (to the magnetic field) ion velocity, z component. $v_{E\times B,z}$ contains the new electric field with the offset on E_x and E_y. *(f)* The three components of the electric field $\mathbf{E}' = (E_x, E_y, 0)$. In panels *(c)*, *(d)* and *(e)* the black line is the $\mathbf{v}_{E\times B}$ component while the blue line is the $\mathbf{v}_{i,\perp}$ component. The yellow region indicates the same interval as figure 5.1.

non-decoupling between particles and magnetic field in the magnetosheath. Therefore, we have defined a new electric field that will be used in all the other chapters of this work.

TABLE 5.2: Offsets of the E_z and E_y for each spacecraft with the z component of the electric field computed from the relation $\mathbf{E}\cdot\mathbf{B} = 0$.

	ΔE_x (mV/m)	ΔE_y (mV/m)
$mms1$	3.0	1.2
$mms2$	3.5	1.2
$mms3$	3.2	1.4
$mms4$	3.9	1.4

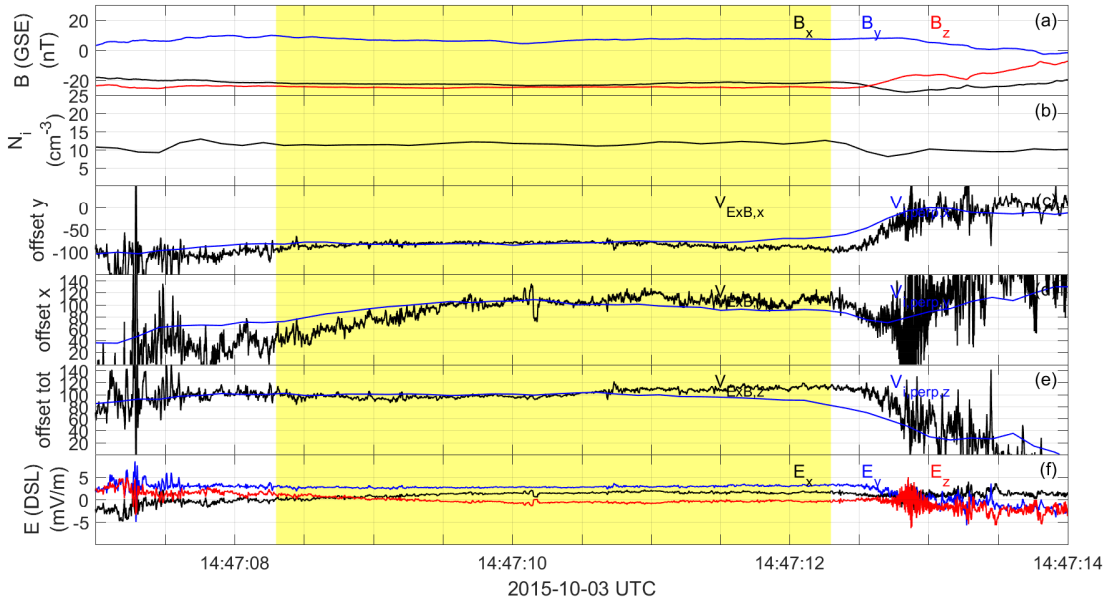

FIGURE 5.4: All data from MMS1. *(a)* The three components of the magnetic field. *(b)* The particles density. *(c)* Comparison between the electromagnetic velocity and the perpendicular (to the magnetic field) ion velocity, x component. $v_{E\times B,x}$ contains the new electric field with the offset on E_y. *(d)* Comparison between the electromagnetic velocity and the perpendicular (to the magnetic field) ion velocity, y component. $v_{E\times B,y}$ contains the new electric field with the offset on E_x. *(e)* Comparison between the electromagnetic velocity and the perpendicular (to the magnetic field) ion velocity, z component. $v_{E\times B,z}$ contains the new electric field with the offset on E_x and E_y. *(f)* The three components of the electric field $\mathbf{E}''$. In panels *(c)*, *(d)* and *(e)* the black line is the $\mathbf{v}_{E\times B}$ component while the blue line is the $\mathbf{v}_{i,\perp}$ component. The yellow region indicates the same interval as figure 5.1.

Chapter 6

Evaluation of the terms of Ohm's law

Chapters 4 set all the basis for the data analysis in the local frame of the magnetopause. This is essential, as we already underlined before, since in this way we are able to look at the data without the effects that rotations and motion could induce on them. Furthermore, only in that way a fruitful comparison with the results from simulation can be conducted.
In this chapter, we continue the analysis of the event of October,3 2015, characterised with two consecutive crossings, with the aim of computing all the terms of the generalised Ohm's law and to understand their contribution to the electric field during magnetic reconnection. Section 6.1 analyses in details the two crossings and individuates the presence of evidences of reconnection throughout the first one (Hall field signature, particle acceleration) while these are not present anymore at the time of the second crossing. A comparison between the electric and $\mathbf{v}_i \times \mathbf{B}$ and $\mathbf{v}_e \times \mathbf{B}$ allows to identify an ion diffusion region.
Section 6.2 is devoted to the computation of the electric field parallel to the magnetic field. This is always a tricky quantity to measure because of the value of the electric field, usually of the same order of the error bar. We see that there is a DC electric field lasting $\sim 1\ s$ during the first crossing that confirms the reconnection's signatures identified before.
In the last part of the chapter we deal with the computation of the terms of the generalised Ohm's law. Section 6.3 starts presenting the results that have been achieved until now with data from the Cluster mission and conclusions from simulations. Then we present our results: we report an encounter with a ion diffusion region in the first crossing, Ohm's law's predominant term is the Hall term as expected. During the second crossing we do not observe reconnection, the ideal Ohm's law holds. In the last section of the chapter we apply our scripts to the data of October,16 in order to check them. We obtain a good agreement with the results of [16].

6.1 Evidences of reconnection

Some of the typical evidences of reconnection are listed in section 1.4. In figure 6.1 and 6.2 we can see the magnetic field and the ion velocity in the LMN frame for both the crossing. Two important signatures of reconnection characterize the first crossing and are not visible in the second one. During the first crossing, the m component of the magnetic field exhibits a Hall field that indicates the decoupling of ions from the magnetic field. Electrons are likely still frozen with the magnetic field, as we will see in the following. This behaviour has been explained in section 1.3.3 and the sign and the shape of the magnetic field is compatible with the Hall field observed in asymmetric reconnection simulations, [30]. Another evidence of magnetic reconnection is the presence of a clear *jet* in the l component of the ion velocity. Ion velocity is $\sim 200\ km/s$ directed southward ($\mathbf{l}_1$ direction is almost $\mathbf{z}$ direction of the GSE system, see table 4.5) right before the crossing and then it becomes directed northward and with a value of $\sim 100\ km/s$. These two features let us think that a magnetic reconnection process is occurring during the first crossing. In particular, we are crossing a ion diffusion region as witnessed by the Hall field. In figure 6.2 the second crossing is shown and the Hall field is no longer present, as well as particle acceleration. The ion velocity appears to be almost constant across the current sheet. Our hypothesis is that $\sim 15\ s$ after the first crossing the reconnection process has stopped, or the motion of the magnetopause put the spacecraft constellation in a position where the reconnection is no longer observable. In both the conditions, this event offers the possibility to look at the plasma and field condition of reconnection and no-reconnection right afterwards, with a separation of $\sim 10\ s$ between the two status.

Therefore, we have identified an ongoing reconnection process throughout the first crossing. In figure 6.3 the two crossings are shown together in the GSE frame. In this frame we can still see the presence of the *jet* within the first crossing while the three components of the ion velocity stay almost constant in the following one. The vertical black line indicates the centre of the current sheet, while the yellow shaded region has a width of double the characteristic time corresponding to the ion gyroradius ρ_i. In other words, we define a $t_{gyro} = \rho_i / V_{MP}$ where V_{MP} is the norm of the magnetopause velocity, the characteristic velocity of the system. So, t_{gyro} is a ion time scale. We notice that the Hall quadrupolar field is $\sim 4\ t_{gyro}$ wide in time. In addition, the last panel of figure 6.3 shows the electron temperature computed along the direction parallel and perpendicular to the magnetic field. There a slight increasing (of the order of $\sim 1\%$) of it across the current sheet, as expected. This means that we are crossing a ion diffusion region but not an electron diffusion region, as confirmed by figure 6.4. There, we can see that at $\sim 14:47:00$ the ions are decoupling from the magnetic field and the electrons. This is more evident in the z and x components, where we can see the $\mathbf{E} \neq -\mathbf{v}_i \times \mathbf{B}$. In other words, ideal Ohm's law does not hold anymore for ions in this interval in proximity of the current sheet.

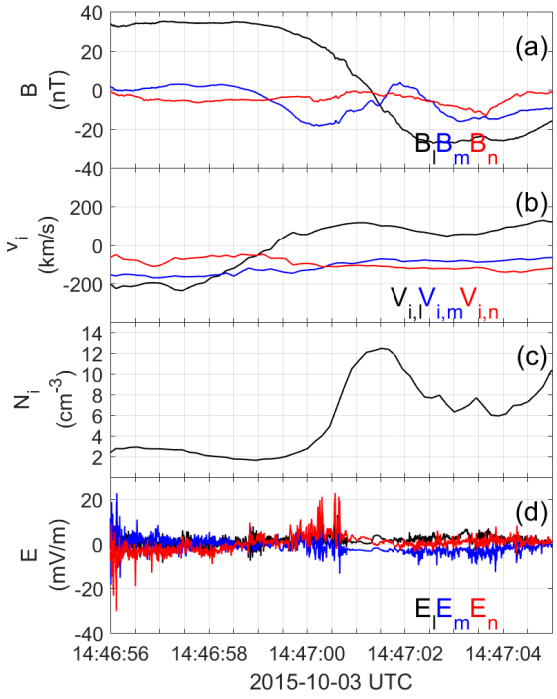

FIGURE 6.1: (*a*) The magnetic field. $\mathbf{B}_m$ shows the quadrupolar shape typical of the Hall field. (*b*) The ion velocity. We can see the acceleration, southward before and northward after, in the l component while the velocity stays approximatively constant in the other directions. (*c*) The ion density (*d*) The three components of the electric field.
All the data are shown in the LMN system and they are from MMS3. An equivalent behaviour is seen by the other spacecraft.

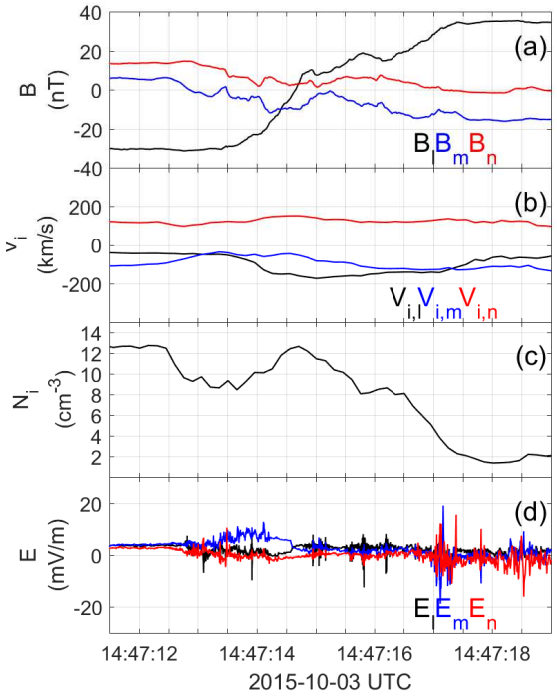

FIGURE 6.2: (*a*) The three components of the magnetic field (*b*) The ion velocity. (*c*) The ion density (*d*) The three components of the electric field.
All the data are shown in the LMN system and they are from MMS3. An equivalent behaviour is seen by the other spacecraft.

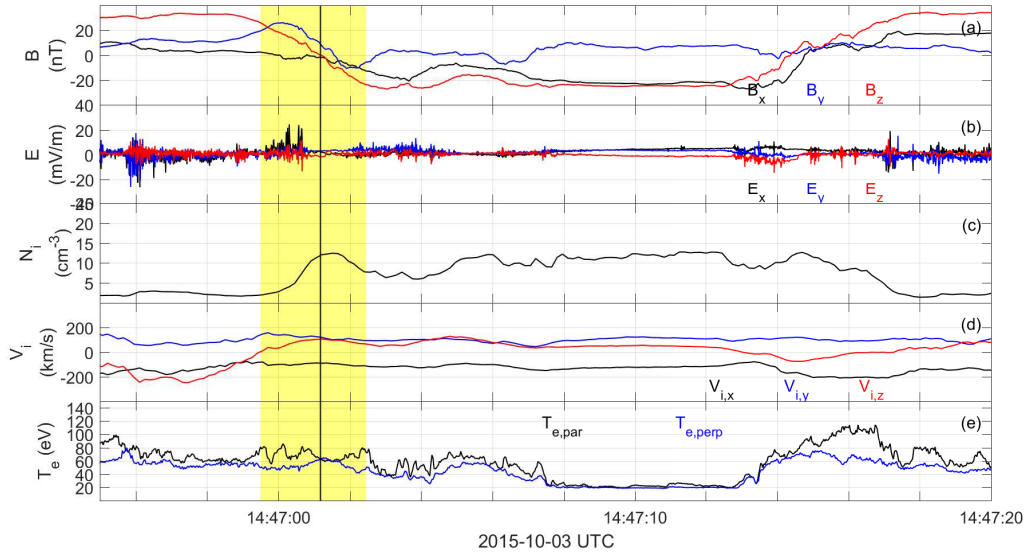

FIGURE 6.3: (*a*) The three components of the magnetic field (*b*) The three components of the electric field. (*c*) The ion density (*d*) The ion velocity. (*e*) The electron temperature, parallel and perpendicular to the magnetic field.
The vertical black line indicates the centre of the current sheet, while the yellow shaded region has a width of double the characteristic time corresponding to the ion gyroradius ρ_i. All the data are shown in the GSE system and they are from MMS3. An equivalent behaviour is seen by the other spacecraft.

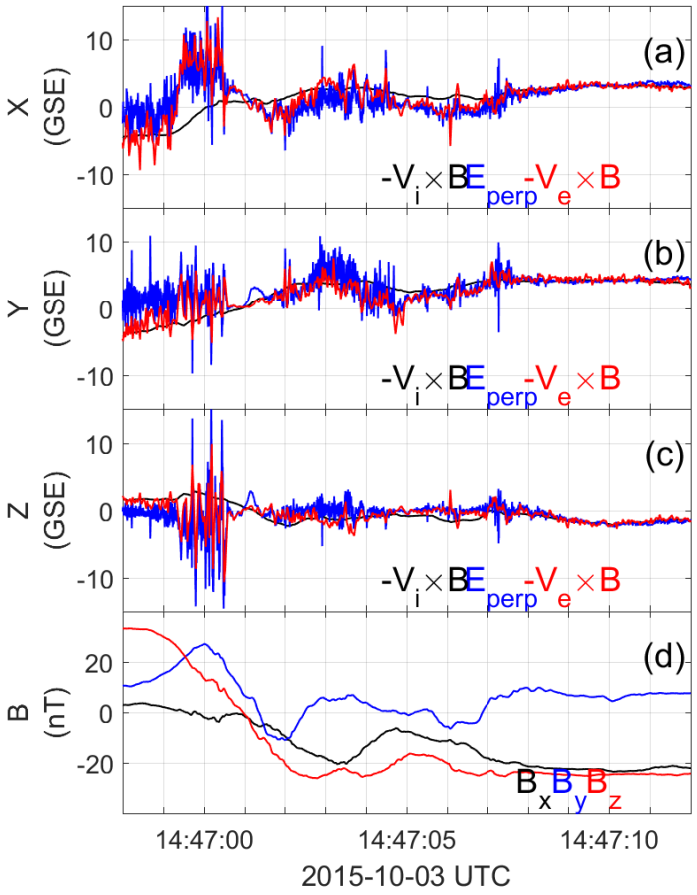

FIGURE 6.4: Panles (a), (b) and (c) show the three component of the electric field, $-\mathbf{v}_i \times \mathbf{B}$ and $-\mathbf{v}_e \times \mathbf{B}$. We spot the presence of a ion diffusion region in the interval $14:46:59 - 14:47:01$ and the presence of waves. All the data are shown in the GSE system and they are from MMS1. An equivalent behaviour is seen by the other spacecraft.

6.2 Parallel electric field computation

As we said in section 1.3.3 (Eq. 1.38) the presence of an electric field parallel to **B** is a condition that has to be fulfilled in case of reconnection. Indeed, the frozen-in condition does not hold when the curl of this quantity is non-zero, but in practice that is probable whenever there is significant deviation of the parallel electric field from zero. Nevertheless, it is extremely difficult to estimate this quantity a cause of the presence of waves that can mask its presence and also because it is usually of the order of the error on the electric field. The MMS mission should overcome this difficulty. However, even if the instrumental error is 0.5 mV/m, the total uncertainty on the electric field (adding the other sources of error) yield a $\delta E_{par} \sim 2\ mV/m$ that makes the evaluation of the parallel electric field ardous. In this section, we compare different way to obtain the parallel electric field. In panel *a* of figure 6.5 we present the parallel electric field that is already computed in *EDP* file of level *l2_pre*. The maximal values of the field are reached at 14 : 46 : 59.50 but these fluctuations are likely due to the presence of waves since they do not give any contribution to the dissipated power, as one sees in panel *b* of the same figure. The biggest contribution to $\mathbf{J} \cdot \mathbf{E}$ is found immediately after and we can spot the presence of a DC field between 14 : 47 : 00 and 14 : 47 : 01.

Another way to obtain the parallel electric field is, of course, projecting it on the magnetic field. We do that with the level *l2* data. In order to compare the two results we perform a resampling of the electric field of level *l2_pre* over the magnetic field. This allows also to filter some of the fluctuations due to the waves.
Figures 6.6 and 6.7 show respectively the parallel electric field obtained from the data of level *l2_pre*, resampled over the magnetic field and the parallel electric field obtained from the data of level *l2*. While in figure 6.6 the parallel electric field shows fluctuations around 0 mV/m and a DC field of $\sim 1\ mV/m$ in the interval 14 : 47 : 00 and 14 : 47 : 01, in figure 6.7 we observe a non-zero parallel electric field that has a peak $>\ 2\ mV/m$ in $14:47:00 - 14:47:01$ and then it lasts for several seconds. This behaviour should yield a wide diffusion region of which we find no trace in the other phases of the study. Therefore, we conclude that it is better to consider the *l2_pre* data for now.

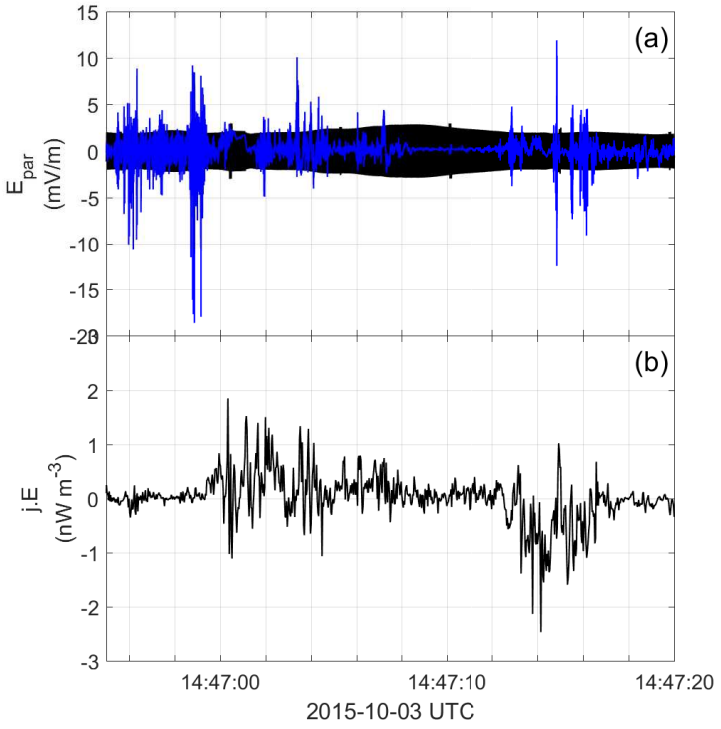

FIGURE 6.5: (*a*) Parallel electric field obtained from the data of level *l2_pre*. The black region is the error bar of $\sim 2\ mV/m$, the blue line is the electric field itself. (*b*) The dissipated power $\mathbf{J} \cdot \mathbf{E}$, the electric field is computed in the magnetopause frame. Data are from MMS1.

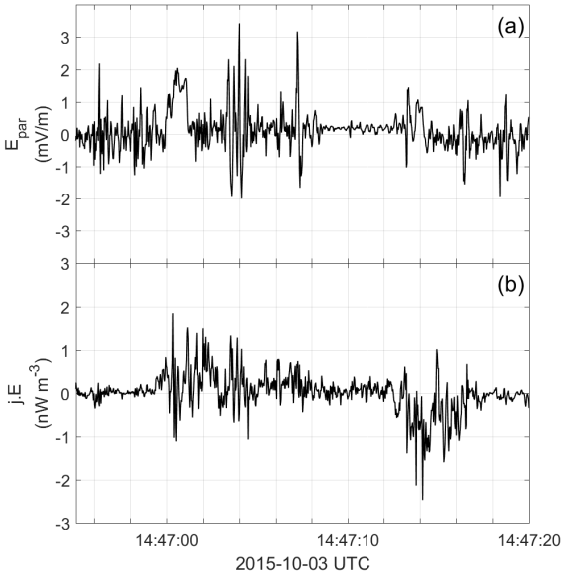

FIGURE 6.6: (*a*) Parallel electric field obtained from the data of level *l2_pre*, resampled over the magnetic field. (*b*) The dissipated power $\mathbf{J} \cdot \mathbf{E}$, the electric field is computed in the magnetopause frame. Data are from MMS1.

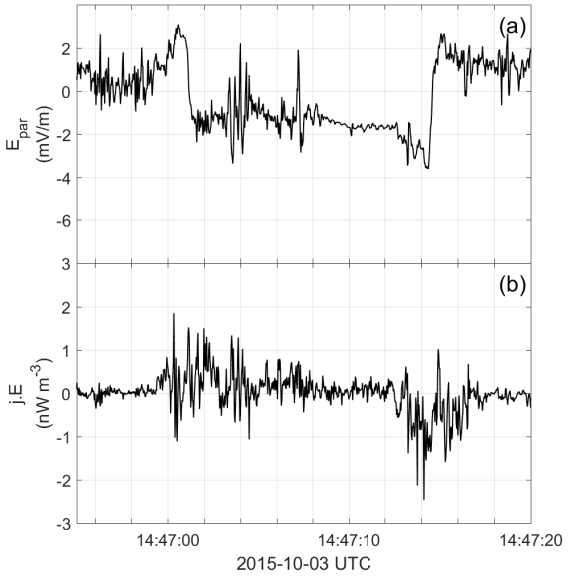

FIGURE 6.7: (*a*) Parallel electric field obtained from the data of level *l2*. (*b*) The dissipated power $\mathbf{J} \cdot \mathbf{E}$, the electric field is computed in the magnetopause frame. Data are from MMS1.

6.3 The Ohm's law

After the analysis of the event given in the last two sections, we focus on the Ohm's law and the evaluation of all its terms.

Efforts has been already done in the past in order to compute this quantities, in particular with the data of the Cluster mission [17], [18], [19]. In fact, even if Cluster was meant to explore the polar cusp, it unexpectedly became a major contributor to the reconnection problem. Clearly, Cluster did not investigate reconnection at the subsolar magnetopause, but an anti-parallel magnetic fields configuration appears along its orbit as well. However, Cluster had limited time resolution and usually larger spacecraft separation (with a minimum inter-spacecraft distance of 100 km), providing insight into reconnection on the ion scale only. Electron scales were barely approached.

In particular, Cluster cannot determine the important parallel component of the electric field, except in very rare current sheet orientations, because there were no 3-axis sensors. Furthermore, the pressure terms and the inertial term are impossible to determine from the time and energy resolution available with Cluster instrumentation. In particular, the pressure tensor is not measured so the pressure term of Ohm's law is estimated from temperature and density measurements. Since for particles measurements the time resolution is equal to the spin period (4 s for Cluster), it is not even sufficient to determine the $\mathbf{v}_i \times \mathbf{B}$ term in Ohm's law on times scales shorter that the spacecraft spin. Therefore, with Cluster measurements it was impossible to perform a complete investigation of Ohm's law and to reach a complete understanding of the mechanisms of the reconnection process. In order to better understand the results that have been achieved with Cluster, in figure 6.8 and 6.9 we show the evaluation of the Ohm's law proposed respectively in [17] and [19].

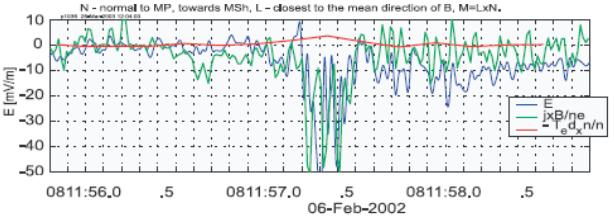

FIGURE 6.8: On February 6, 2002 at 0800 UTC, the Cluster constellation was in the high latitude afternoon magnetopause. These are three terms of the generalised Ohm's law derived from observation. Adapted from [17].

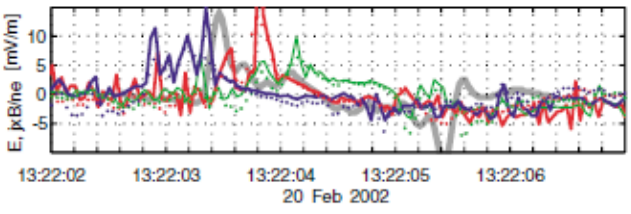

FIGURE 6.9: On February 20, 2002 at 1300 UTC the Cluster constellation reported magnetopause crossings tailward and duskward of the cusp. The electric field (solid lines) and the Hall term (dotted lines) normal to the magnetopause are shown for three of the spacecraft C2, C3, C4. The thick grey line indicates result from simulations. Adapted from [19].

Several attempts to evaluate Ohm's law have been made also trough simulations. In [21] the electron pressure nongyrotropies support collisionless magnetic reconnection even if electrons are not free to move in the diffusion region. Then, one of the latest studies can be found in [20]. In this paper, the problem is faced with a particle-in-cell simulation. They compute all the term of Ohm's law inserting also the anomalous resistivity term (in this case $\propto \delta n\ \delta\mathbf{E}$, where δn corresponds to the density fluctuation and $\delta\mathbf{E}$ to the electric field fluctuation). Even though the contribution of the anomalous resistivity and of the pressure terms are the two mechanisms

that have been widely invoked to be responsible for the electric field in the generalised Ohm's law, their results suggest that another term linked with turbulence, the *turbulent momentum transport* term ($\propto \nabla \cdot (\delta \mathbf{v}_e \, \delta \mathbf{A})$, where $\mathbf{A}$ is the vector potential), sustains the electric field. In particular, they observe that the contribution of this term rises concurrently with a process of current sheet filamentation. All these results need to be confirmed and sustained by experiments.

Lately, in June 2016, an Ohm's law evaluation has been done here [16]. Data of an encounter with an electron diffusion region are presented and the terms of Ohm's law are computed. This paper represents the first attempt to evaluate the terms of Ohm's law with MMS data. From the computation of the dissipated power computed for every term, it emerges that a big contribution (up to 50% of the total) seems to be represented by the unidentified residual, probably due to the anomalous resistivity, whose source is still not identified. Nevertheless, it may play an important role at the electron diffusion region. This paper can be a way to check our scripts about the Ohm's law, as we will do in the following.

6.3.1 Computation of the terms

In this section we show the computation of all the terms of the generalised Ohm's law of Eq. 1.41 that we report here for clarity:

$$\mathbf{E} + \mathbf{u} \times \mathbf{B} = \frac{1}{ne}\mathbf{J} \times \mathbf{B} - \frac{1}{ne}\nabla \cdot \left(\overline{\mathbf{P}}_e - \frac{m_e}{m_i}\overline{\mathbf{P}}_i\right) + \frac{m_e}{ne^2}\left[\frac{\partial \mathbf{J}}{\partial t} + \nabla \cdot (\mathbf{J}\mathbf{u} + \mathbf{u}\mathbf{J})\right] + \mathbf{A}_e \tag{6.1}$$

Since $\mathbf{P}_{e,jk} \sim 0.1 \; \mathbf{P}_{i,jk}$ for every j and k, the term $\frac{m_e}{m_i}\overline{\mathbf{P}}_i$ makes corrections of less than 1%, so it is neglected in the following.
The computation of the Hall term is quite straightforward since the current density has already been computed in section 4.5.
The pressure term is computed using the components of the pressure tensor yield by the *FPI* instrument. Since we already know how to compute the gradient of a quantity, we try to exploit that in order to obtain the divergence of the pressure tensor. In fact, if $\overline{\mathbf{T}}$ is a symmetric tensor (as the pressure one),

$$(\operatorname{div} \overline{\mathbf{T}})_k = (\operatorname{grad} \overline{\mathbf{T}}_{kk})_k + (\operatorname{grad} \overline{\mathbf{T}}_{kj})_j + (\operatorname{grad} \overline{\mathbf{T}}_{ki})_i. \tag{6.2}$$

This represents something completely new since, as we already said, we are now able to get high resolution measure of the pressure gradient while this was impossible with the data from the previous missions.

The computation of the inertia term is made using again Eq. 6.2 on the tensors $\mathbf{J}\mathbf{u}$ and $\mathbf{u}\mathbf{J}$. The term $\frac{\partial \mathbf{J}}{\partial t}$ is neglected since the behaviour of the current density is more or less the same for the four spacecraft (with the lags due to the fact that the spacecraft do not cross the current sheets all at the same time). This can be seen in figure 6.10 and 6.11. The only difference between the signals can be spot in the n direction at the time $\sim 14:47:00.50$ but it does not effect

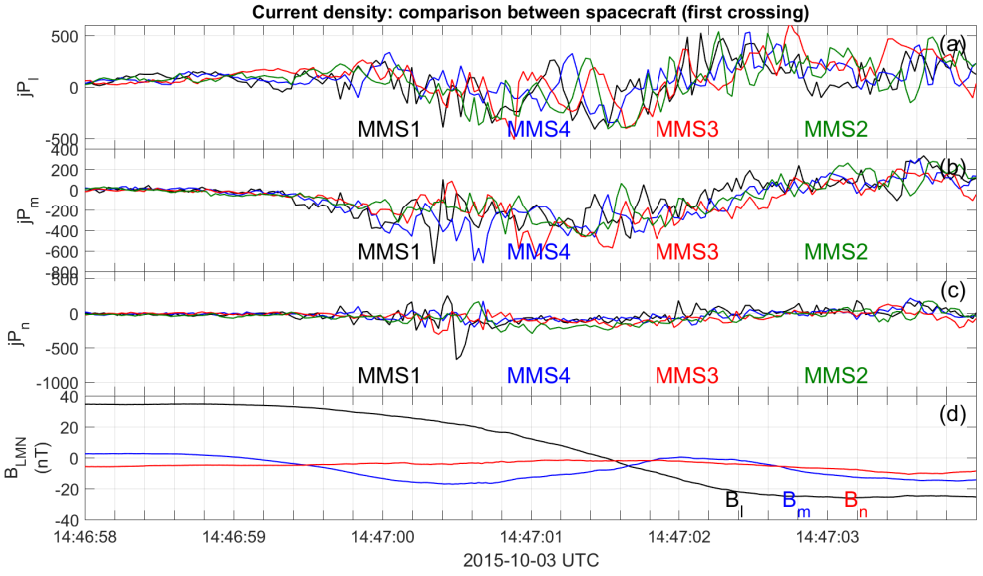

FIGURE 6.10: (a) l component of the current densities computed with the particles data for the four spacecraft. (b) m component of the current densities computed with the particles data for the four spacecraft. (c) n component of the current densities computed with the particles data for the four spacecraft. (d) The three component of the magnetic field. The unit of the three components of the current densities is $\mathbf{nA/m^2}$. All the quantities in this figure are plotted in the LMN system of the first magnetopause crossing.

significantly the whole term (there is a difference of the order of 0.005 mV/m). The computation of the inertia term is also completely new since the time resolution of the previous mission was largely not sufficient.

As witnessed already by 6.4, we are more likely looking at a ion diffusion region while there are not evidences of electrons decoupling from the magnetic field. Therefore, as we already said in section 1.3.3.1, the pressure and the inertia terms are expected to be negligible compared to the Hall term. Indeed, this is what we see in figure 6.12 and 6.13 where all the computed terms are shown separately. We notice that, in particular, the inertia term is negligible compared to the others. Furthermore, we can already infer from these figures that while in the first crossing the electric field is mainly sustained by the Hall and also the pressure term; during the second crossing all the terms on the right hand side of Eq. 6.1 are smaller that the 'ideal' term $\mathbf{u} \times \mathbf{B}$.

It is easier to compare the importance of the different terms and to better understand their role if we look at figure 6.14 and 6.15. In panel c all the terms are superposed and the Hall and the ideal term are clearly the two concurring to the electric field. In panel d we plot the left and the right side of Eq. 6.1. Indeed,

$$\mathbf{E}_{rhs} = \frac{1}{ne}\mathbf{J} \times \mathbf{B} - \frac{1}{ne}\nabla \cdot \overline{\mathbf{P}}_e + \frac{m_e}{ne^2}\nabla \cdot (\mathbf{Ju} + \mathbf{uJ}) \tag{6.3}$$

$$\mathbf{E}_{lhs} = \mathbf{E} - \mathbf{u} \times \mathbf{B} \tag{6.4}$$

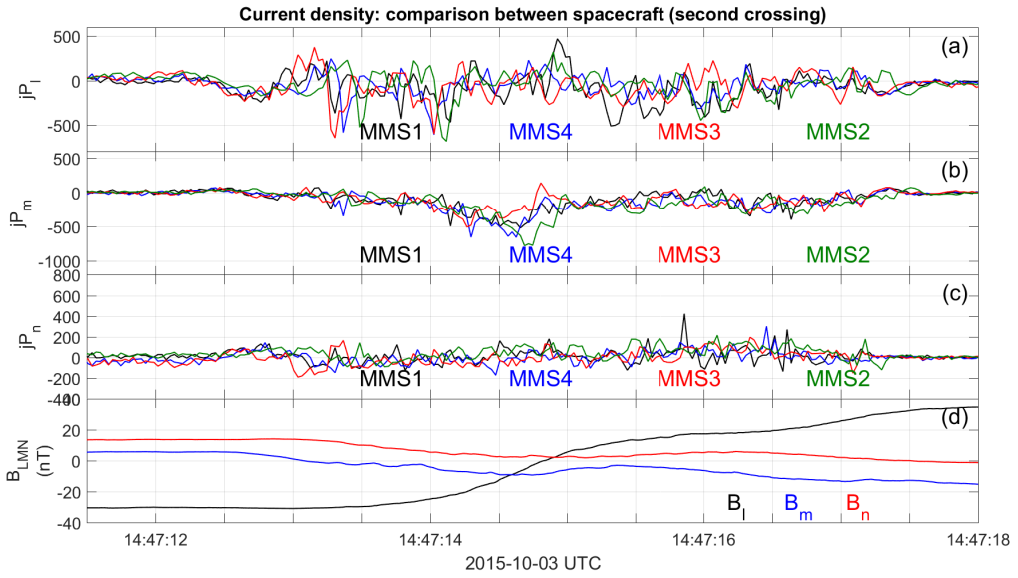

FIGURE 6.11: (*a*) l component of the current densities computed with the particles data for the four spacecraft. (*b*) m component of the current densities computed with the particles data for the four spacecraft. (*c*) n component of the current densities computed with the particles data for the four spacecraft. (*d*) The three component of the magnetic field. The unit of the three components of the current densities is $\mathbf{nA/m^2}$. All the quantities in this figure are plotted in the LMN system of the second magnetopause crossing.

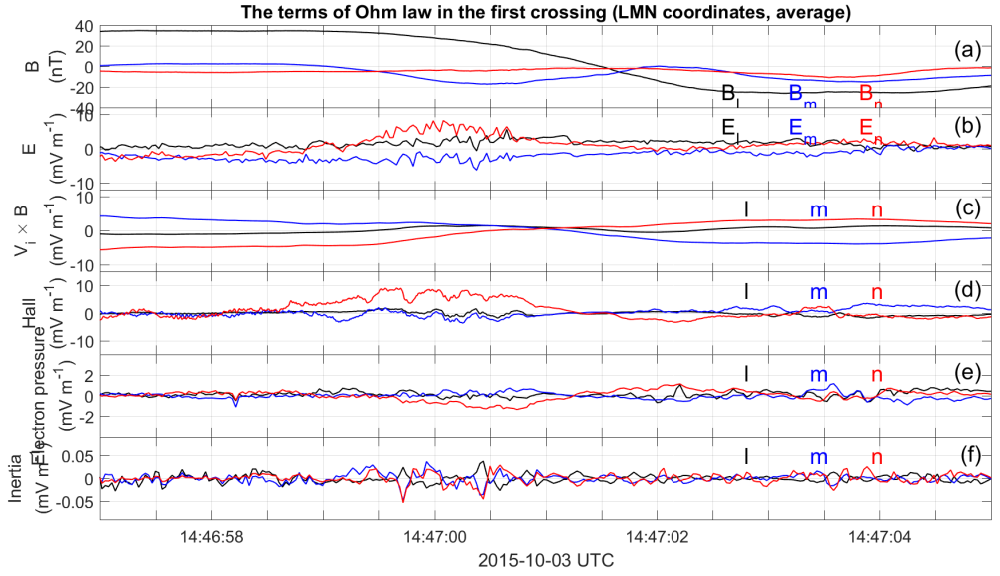

FIGURE 6.12: (*a*) The three components of the magnetic field. (*b*) The three components of the electric field. (*c*) The 'ideal' term $\mathbf{u} \times \mathbf{B}$. (*d*) The Hall term $\frac{1}{ne}\mathbf{J} \times \mathbf{B}$. (*e*) The pressure term $-\frac{1}{ne}\nabla \cdot \overline{\mathbf{P}}_e$. (*f*) The inertia term $\frac{m_e}{ne^2}\nabla \cdot (\mathbf{Ju} + \mathbf{uJ})$. All the quantities are computed in the LMN frame of the first crossing.

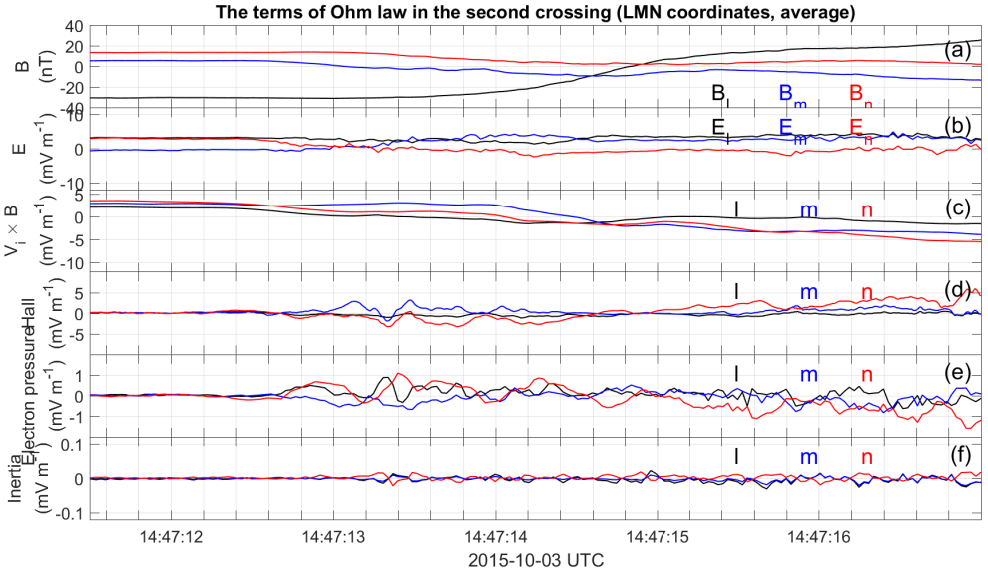

FIGURE 6.13: (*a*) The three components of the magnetic field. (*b*) The three components of the electric field. (*c*) The 'ideal' term $\mathbf{u} \times \mathbf{B}$. (*d*) The Hall term $\frac{1}{ne}\mathbf{J} \times \mathbf{B}$. (*e*) The pressure term $-\frac{1}{ne}\nabla \cdot \overline{\mathbf{P}}_e$. (*f*) The inertia term $\frac{m_e}{ne^2}\nabla \cdot (\mathbf{Ju} + \mathbf{uJ})$. All the quantities are computed in the LMN frame of the second crossing.

In figure 6.14 and 6.15 we report only the n components of all the terms and then of $\mathbf{E}_{rhs}$ and $\mathbf{E}_{lhs}$ but in all the cases we find a good agreement these last two quantities, within the error bars of $\sim 1\ mV/m$. Indeed, the behaviour of $\mathbf{E}_{rhs}$ and $\mathbf{E}_{lhs}$ is the same, there some small fluctuation in $\mathbf{E}_{lhs}$ that are probably due to the presence of waves in the electric field signal.
Concerning the second crossing, in figure 6.15 we notice that the ideal Ohm's law is verified.

We verify the validity of the Ohm's law in the case of an encounter of a ion diffusion region. We confirm the result obtained in the past but we add a contribution: we give the estimation of terms that was not possible before and we improve the computation of other terms. For example, it is worth to remember that the 'ideal' term could present only one measurement in 4 seconds with Cluster data, while now we have a measurement of the ion velocity each 125 ms.

The term $\mathbf{A}_e$ in Eq. 6.1 is not computed in this study since we found that it has not a crucial role in this event: the generalised Ohm's law is verified within the error bars without adding its contribution. However, in this case we do not observe the electron diffusion region while in [16] an encounter with an EDR is analysed and the the terms that we have computed here are not sufficient to satisfy the equality in the Ohm's law. At the electron scales, then, the contribution of the anomalous resistivity might be crucial. This deserves further investigation: in particular, the origin of the anomalous resistivity is still not known and a proper determination of the contribution of waves is required in order to have a better comprehension of the process.

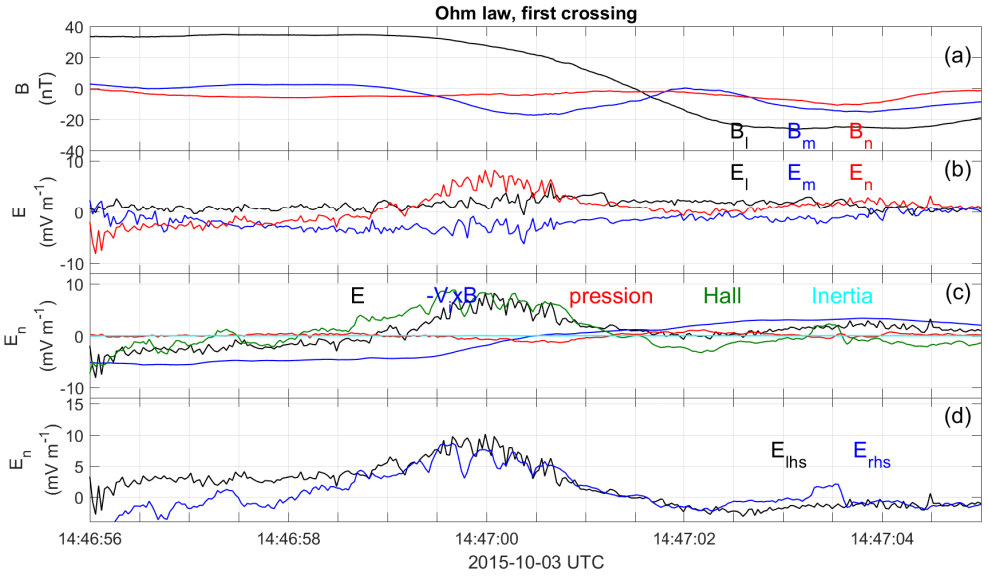

FIGURE 6.14: (*a*) The three components of the magnetic field, average of the four sapcecraft. (*b*) The three components of the electric field, average of the four spacecraft. (*c*) All the terms of Ohm's law superposed, shown in the n direction. (*d*) $E_{lhs,n}$ and $E_{rhs,n}$ as defined in Eq. 6.4. All the quantities are computed in the LMN frame of the first crossing.

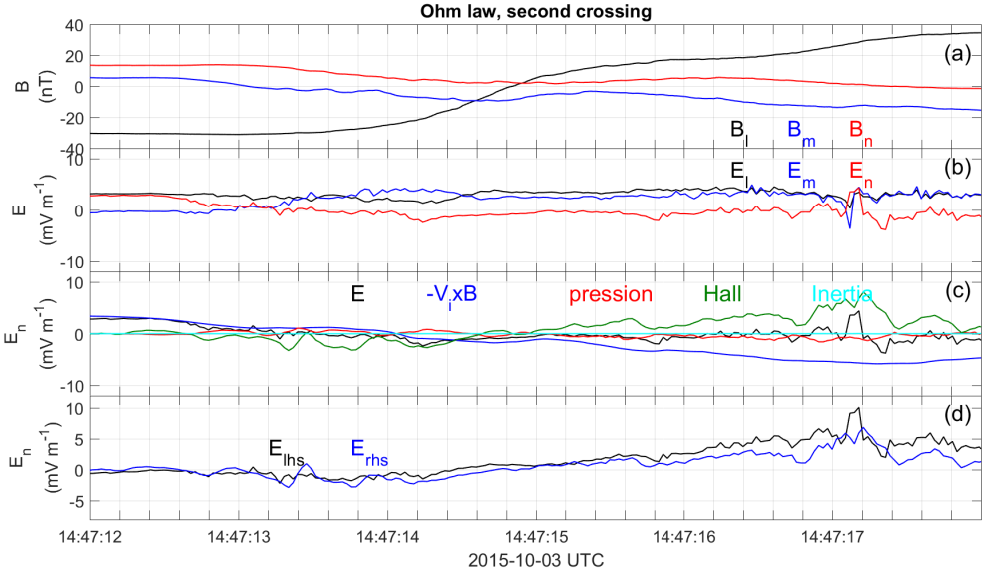

FIGURE 6.15: (*a*) The three components of the magnetic field, average of the four sapcecraft. (*b*) The three components of the electric field, average of the four spacecraft. (*c*) All the terms of Ohm's law superposed, shown in the n direction. (*d*) $E_{lhs,n}$ and $E_{rhs,n}$ as defined in Eq. 6.4. All the quantities are computed in the LMN frame of the second crossing.

6.3.2 Checking our results: the event of October, 16 2015

Since [16] represents the first published attempt to evaluate all the terms of Ohm's law using MMS data, we reproduce the paper's results in order to check our work. We obtain a really good agreement. In this section, we just insert the figure 4 of the paper in figure 6.17 and our reproduction of it, figure 6.16. The only difference we can spot is in the inertia term: with our computation, it reaches a maximum value of 0.2 mV/m in both l and m direction, while in panel d of 6.17 the peaks reach -0.6 mV/m in the m direction. Indeed, there is no a big difference, the two results are the same within the error bar. Nevertheless, while we compute the inertia term as it is in Eq. 6.1 (without any further approximation), Torbert *et al.* compute the inertia term in this way: $m_e/ne[\nabla \cdot (n\mathbf{v}_i\mathbf{v}_i - n\mathbf{v}_e\mathbf{v}_e)]$.
This is an important check for our scripts and on the other side we propose our method for the computation of the inertia term.

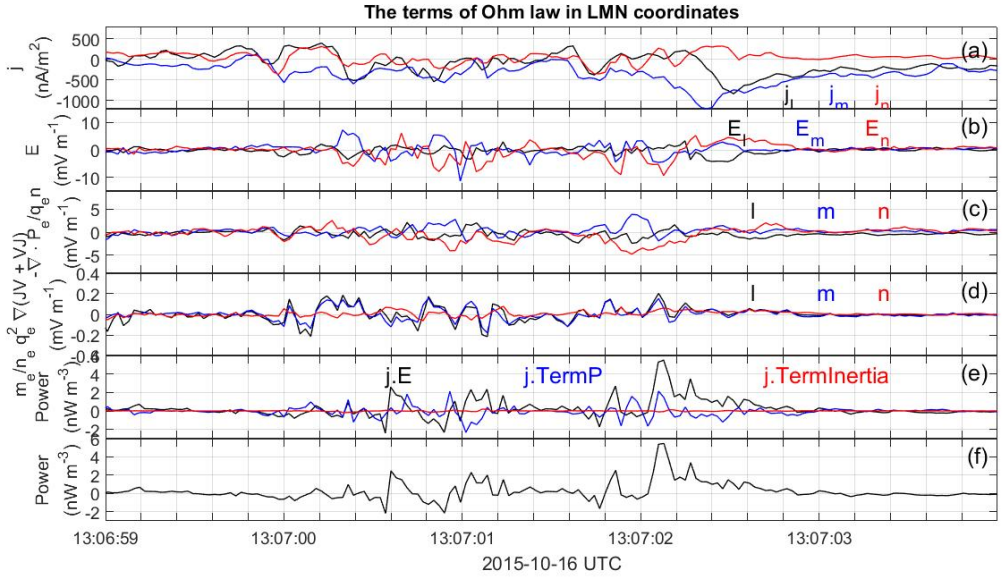

FIGURE 6.16: (a) The current density. $(b-d)$ The comparison of terms in Ohm's law for interval around $13:07:02$. (e) The total power dissipation from individual terms. (f) The residue, $\mathbf{J}\cdot\left(\mathbf{E}' + \nabla\cdot\mathbf{P}/ne + m_e/ne^2[\nabla\cdot(\mathbf{Ju}+\mathbf{uJ})]\right)$.

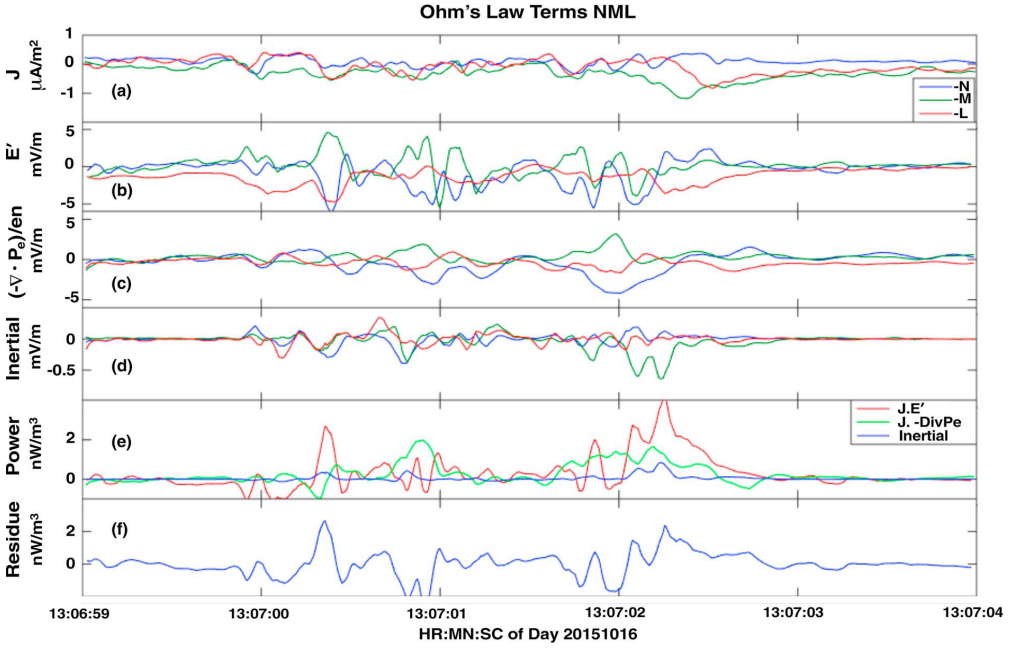

FIGURE 6.17: (a) The current density. $(b-d)$ The comparison of terms in Ohm's law for interval around $13:07:02$. (e) The total power dissipation from individual terms. (f) The residue, $\mathbf{J}\cdot(\mathbf{E}'+\nabla\cdot\mathbf{P}/ne+m_e/ne[\nabla\cdot(n\mathbf{v}_i\mathbf{v}_i-n\mathbf{v}_e\mathbf{v}_e)])$. Figure from [16].

Chapter 7

Conclusions and outlook

In this section we shall summarize the main concepts and results of this thesis and to discuss possible future work.

This study is devoted to the computation of the terms in the generalised Ohm's law. This equation is fundamental in the theory of collisionless reconnection since knowing the relative importance of the different terms should lead to a better comprehension of this process, that is still largely not understood. However, only few studies in the past has been focused on this purpose and results from simulations do not perfectly agree between each other.
This thesis presents one of the first examples of complete evaluation of the Ohm's law terms.

We analyse for the first time the event of October,3 2015, when the MMS constellation have been crossed repeatedly by the magnetopause. We focus on two crossings in particular: one of them shows evidences of magnetic reconnection. It deals with an asymmetric reconnection event with a few nT guide field. We identify an encounter with a ion diffusion region, while we are not able to spot the electron diffusion region during this event.
We verify the validity of the Ohm's law computing all the terms at the highest resolution available, [14]. The evaluation of the pressure and the inertia term represents a new achievement allowed by the data of the MMS mission.
We confirm the results obtained in the past: the electric field during the reconnection event (at ion scale) is sustained by the Hall term. The pressure term and especially the inertia one are negligible at this scale.
In conclusion, we add the estimation of terms that was not possible before and we improve the computation of other terms. For example, it is worth to remember that the 'ideal' term $\mathbf{u} \times \mathbf{B}$ could present only one measurement every 4 seconds with Cluster data, while now we get a measurement of the ion velocity each 125 ms.

This thesis gives rise to a number of important topics that could not be investigated in detail during this work. Its limitations leave a number of open questions which serves to outline possible future directions of research. The individuation of encounters with electron diffusion regions will lead to a better comprehension of the role of the pressure and the inertia term. This is still

controversial, even in simulations.
Furthermore, even if in this study the term of the so-called *anomalous resistivity* is not taken into account, it is shown in [16] that in proximity of the electron diffusion region it may be a fundamental role. Since its definition highly depends on the morphology of the spectre, a detailed analysis of the waves mode and turbulence would be needed.
In addiction, the improving of data calibration throughout the rest of the mission will yield better measurements, *e.g* of the parallel electric field, leading to a more accurate picture of reconnection.

Appendix A

Coordinate systems

In order to facilitate the reading, the coordinates system used in the thesis can be found here:

Geocentric Solar Ecliptic system (GSE): The X-axis points from the Earth towards the Sun. The Y -axis and the X-axis lie in the ecliptic plane and the Y-axis points towards the dusk. The Z-axis is perpendicular to the ecliptic plane and directed towards the Northern ecliptic pole.

Geocentric Solar Magnetospheric system (GSM): The X-axis points from the Earth towards the Sun. The X-Z plane contains the dipole axis. The Y -axis is perpendicular to Earth's magnetic dipole, it points towards the dusk.

De-spun Body Spacecraft Coordinate System (DBCS): It is the spacecraft frame. It is very close to Geocentric Solar Ecliptic (GSE) coordinates (within $2° - 3°$) since MMS maintains an equatorial orbit (in the the phase that contains the data treated in this thesis).

De-spun Sun-pointing L-momentum vector (DLS): The Z-axis is the spin axis of the spacecraft. The X-axis is directed positive towards the Sun, the Y-axis completes the orthogonal system.

Minimum variance system (LMN): It is a local system obtained with the Minimum Variance Analysis, 2.1.1 where the N direction is directed normally to the structure (current sheet ...) and the M and L direction are tangent to the structure.

Appendix B

Standard calibration for the SDP instrument

Double-probe electric field experiments (see section 3.2.1) have been used already on other mission, in particular, the Electric Field and Wave (EFW) instrument on Cluster had the same structure and basic principle of the SDP instrument on Magnetospheric Multiscale. For this reason, the calibration process for SDP follows essentially the same procedures used for EFW, [45]. In this Appendix, the standard procedure for the calibration of the SDP data is briefly reviewed. It involves spin fits of the data and definition of several offsets. The aim of this Appendix is to summarize the basic principle of the calibration done for SDP and to make the reader aware of some of the issues and the problems one have to deals with during the calibration process. Procedures of cross-calibration and inter-calibration are not addressed here.

The raw data available from SDP are the two orthogonal electric field components in the spinning frame, E_{12} and E_{34} and the potential measured by each probe P_i, $i = 1, 2, 3, 4$.
After an initial cleaning of the data from the bad measures due to electronic issues and saturations, the first step of the calibration deals with the spin fit. The spin fit takes into account that the spacecraft is spinning with a period T ($T \sim 20\ s$ for MMS) so the signal, which in this case is the probe differential difference, is fitted to

$$\begin{aligned} y &= \sum_{n=0}^{\infty} a_n \ \sin(n\omega t) + \sum_{n=0}^{\infty} b_n \ \cos(n\omega t) \\ &= a_0 \ + \ b_0 \ + \ a_1 \sin(\omega t) \ + \ b_1 \cos(\omega t) \ + \ a_2 \sin(2\omega t) \ + \ b_2 \cos(2\omega t) \cdots \end{aligned} \tag{B.1}$$

where $\omega = 2\pi/T$. Usually, the second order terms are already negligible comparing to the others. In the case of not negligible second or even third order terms there might been some problems with the measurements. In order to adopt the same definitions we find in [45], we call A the zero-order term $A = a_0 + b_0$, while $a_1 = B$ and $b_1 = C$.

The terms B and C provide the spin resolution 2-D electric field in DSL system:

$$E_{x,spin} = \alpha(B - \Delta E_x) \tag{B.2}$$

$$E_{y,spin} = \alpha(C - \Delta E_y) \tag{B.3}$$

where α is an amplitude correction due to the spacecraft potential affecting the electric field measurements and ΔE_x, ΔE_y are offset depending on the plasma conditions obtained from the inter-spacecraft calibration and the cross calibration with other instrument (not detailed in this thesis). For the Cluster mission, $\alpha = 1.1$.

As the spin fit would typically yield different values for the electric field from the two different probe pairs, it is useful to introduce an additional offset, the *delta* offset Δ_{p12p34}:

$$\Delta_{x,p12p34} = E_{x,spin}(E_{12}) - E_{x,spin}(E_{34}) \tag{B.4}$$

$$\Delta_{y,p12p34} = E_{y,spin}(E_{12}) - E_{y,spin}(E_{34}) \tag{B.5}$$

Furthermore, we introduce the raw data DC offset Δ_{raw}. Ideally, the DC level of the raw data should be zero. However, small differences between the probe surfaces and in the electronics create a DC offset in the raw data. If not corrected, it shows up as a signal at the spin frequency in the despun electric field. Δ_{raw} can be computed as the time average of the zero-order term A previously defined. Since it is found that A not only depends on the electronic of the instrument, but also on the plasma environment, Δ_{raw} is usually computed with an average over a fixed number of spins with empirically determined weights. Finally, we obtain the despun full-resolution electric field:

$$E_x = \mathrm{Re}[(E_{12} - \Delta_{raw,12})\mathrm{e}^{i\phi_{12}}] + \mathrm{Re}[(E_{34} - \Delta_{raw,34})\mathrm{e}^{i\phi_{34}}] - \Delta_{x,p12p34} \tag{B.6}$$

$$E_y = \mathrm{Re}[(E_{12} - \Delta_{raw,12})\mathrm{e}^{i\phi_{12}}] + \mathrm{Re}[(E_{34} - \Delta_{raw,34})\mathrm{e}^{i\phi_{34}}] - \Delta_{y,p12p34} \tag{B.7}$$

where $\phi_{12} = \phi_{34} + \frac{\pi}{2}$ is the spin phase of probe 1 with respect to the sun.

Bibliography

[1] D. Biskamp, *Magnetic Reconnection in Plasmas*, Cambridge University Press, (2000).

[2] E. R. Priest and T. G Forbes, *Magnetic Reconnection*, Cambridge University Press, (2000).

[3] M. Yamada, F. M. Levinton, N. Pomphrey, R. Budny, J. Manickam and Y. Nagayama, *Investigation of magnetic reconnection during a sawtooth crash in a hightemperature tokamak plasma*, Phys. Plasmas, 1, 3269, (1994).

[4] R. Giovannelli, *A Theory of Chromospheric Flares*, Nature, 158, 81, (1946).

[5] J. W. Dungey, *Interplanetary Magnetic Field and the Auroral Zones*, Phys. Rev. Lett. 6, 47, (1961).

[6] H. P. Furth, *Sheet pinch instabilities caused by finite conductivity*. Bull. Am. Phys. Soc. 6, 193, (1961).

[7] H. P. Furth, J. Killeen and M. N. Rosenbluth, *Finite-Resistivity Instabilities of a Sheet Pinch*, Phys. Fluids 6, p. 459484, (1963).

[8] P. A. Sweet, *The neutral point theory of solar flares, in Electromagnetic Phenomena in Cosmical Physics*, IAU Symp. 6, ed. B. Lehnert (Cambrige Univ. Press, London) (1958).

[9] E. N. Parker, *Sweet's mechanism for merging magnetic fields in conducting fluids*, J. Geophys. Res., 62, 509, (1957).

[10] H. E. Petschek, *Magnetic field annihilation*, in AAS/NASA Symposium on the Physics of Solar Flares, edited by W. N. Ness, p. 425, NASA, Washington, D. C., (1964).

[11] W. Baumjohann, R. A. Treumann, *Basic Space Plasma Physics*, Imperial College Press, (2012).

[12] MMS site: `http://mms.space.swri.edu/index.html`.

[13] IRFU site: `https://github.com/irfu/irfu-matlab`

[14] J. L. Burch, T. E. Moore, R. B. Torbert and B. L. Giles, *Magnetospheric Multiscale Overview and Science Objectives*, Space Sci Rev (2015).

[15] D. N. Baker, L. Riesberg, C. K. Pankratz, R. S. Panneton, B. L. Giles, F. D. Wilder and R. E. Ergun, *Magnetospheric Multiscale Instrument Suite Operations and Data System*, Space Sci Rev, 199, Issue 1, pp 545-575, (2016).

[16] R. B. Torbert, *et al.*, *Estimates of terms in Ohms law during an encounter with an electron diffusion region*, Geophys. Res. Lett., 43, 59185925, (2016) .

[17] M. André, A. Vaivads, S. C. Buchert, A. N. Fazakerley and A. Lahiff, *Thin electron-scale layers at the magnetopause*, Geophys. Res. Lett., L03803, (2004).

[18] Y. V. Khotyaintsev, A. Vaivads, A. Retinò, M. André, C. J. Owen and H. Nilsson, *Formation of inner structure of a reconnection separatrix region*, Phys. Rev. Lett., 97, 205003, (2006).

[19] A. Vaivads, Y. Khotyaintsev, M. André, A. Retinò, S. C. Buchert, B. N. Rogers, P. Décréau, G. Paschmann and T. D. Phan, *Structure of the Magnetic Reconnection Diffusion Region from Four-Spacecraft Observations*, Phys. Rev. Lett., (2004).

[20] H. Che, J. F. Drake and M. Swisdak, *A current filamentation mechanism for breaking magnetic field lines during reconnection*, Nature, 474, 184187, (2011).

[21] M. Hesse, M. Kuznetsova and M. Hoshino, *The structure of the dissipation region for component reconnection: particle simulations*, Geophys. Res. Lett., 29, 1563, (2002).

[22] S. A. Fuselier, W. S. Lewis, C. Schiff, R. Ergun, J. L. Burch, S. M. Petrinec and K. J. Trattner, *Magnetospheric Multiscale Science Mission Profile and Operations*, Space Sci Rev, 199, Issue 1, pp 77-103,(2016).

[23] G. Pucella, S. E. Segre, *Fisica dei Plasmi*, Zanichelli, (2009).

[24] G. Paschmann, M. Øieroset and T. D. Phan, *In-Situ Observations of Reconnection in Space*, Space Sci Rev, 178:385-417, (2013).

[25] P. W. Daly, G. Paschmann. *Analysis Methods for Multi-Spacecraft Data*. International Space Science Institute, Bern, Switzerland, (2000).

[26] F. S. Mozer, S. D. Bale and T. D. Phan, *Evidence of Diffusion Regions at a Subsolar Magnetopause Crossing*,
Phys. Rev. Lett., 89(1):015002, (2002).

[27] N. Aunai, *Simulation numérique de la reconnexion magnétique : mécanismes cinétiques sous-jacents à la description fluide des ions*, Université Paris Sud - Paris XI. Français. NNT : 2011PA112004, (2011).

[28] A. Chasapis Giannakopoulos, *Study of magnetic reconnection in turbulent plasma using satellite data*, Université Paris Sud - Doctoral School of Astronomy and Astrophysics.

[29] A. Vaivads, A. Retinò and M. André, *Microphysics of Magnetic Reconnection*, Space Sci Rev, 122: 1927, (2006).

[30] P. L. Pritchett, *Onset and saturation of guide-field magnetic reconnection*, Physics of Plasmas, 12, 062301, (2005).

[31] J. L. Burch, *et al.*, *Electron-scale measurements of magnetic reconnection in space*, Science, 352, Issue 6290, (2016).

[32] G. Paschmann, *Space Physics: Breaking through the lines*, Nature, 439, 144-145, (2006) .

[33] V. M. Vasyliunas, *Theoretical models of magnetic field line merging*, 1, Rev. Geophys. 13, 303, (1975).

[34] G. Chanteur, *Accuracy of Fields Gradient Estimations by Cluster: Explanation of its Dependency upon Elongation and Planarity of the Tetrahedron*, European Space Agency (ESA), ESA-SP, vol. 449, p.265, (2000).

[35] M. W. Dunlop, A. Balogh, K.-H. Glassmeier, and P. Robert, *Four-point Cluster application of magnetic field analysis tools: The Curlometer*, J. Geophys. Res. 107(A11), 1384, (2002).

[36] J. H. Lee and V. Angelopoulos, *On the presence and properties of cold ions near Earth's equatorial magnetosphere*, J. Geophys. Res. Space Physics, 119, 17491770, (2014).

[37] S. Toledo-Redondo, M. André, A. Vaivads, *et al.*, *Cold ion heating at the dayside magnetopause during magnetic reconnection*, Geophys. Res. Lett., 43, 5866, (2016).

[38] S. Toledo-Redondo, A. Mats, Y. V. Khotyaintsev *et al.*, *Cold ion demagnetization near the X-line of magnetic reconnection*, Geophys. Res. Lett., 43, 67596767, (2016).

[39] R. B. Torbert, C. T. Russell, W. Magnes *et al.*, *The FIELDS Instrument Suite on MMS: Scientific Objectives, Measurements, and Data Products*. Space Sci Rev 199: 105, (2016).

[40] P. Lindqvist, G. Olsson, R. B. Torbert *et al.*, textitThe Spin-Plane Double Probe Electric Field Instrument for MMS, Space Sci Rev 199: 137, (2016) .

[41] R. E. Ergun, S. Tucker, J. Westfall *et al.*, *The Axial Double Probe and Fields Signal Processing for the MMS Mission*, Space Sci Rev 199: 167, (2016).

[42] C. T. Russell, B. J. Anderson, W. Baumjohann, *et al.*, *The Magnetospheric Multiscale Magnetometers*, Space Sci Rev 199: 189, (2016) .

[43] C. Pollock, T. Moore, A. Jacques, *et al.*, *Fast Plasma Investigation for Magnetospheric Multiscale*, Space Sci Rev 199: 331, (2016).

[44] C. W. Carlson, D.W. Curtis, G. Paschmann and W. Michael, *An instrument for rapidly measuring plasma distribution functions with high resolution*, Adv. Space Res., 2, 7, (1982).

[45] Y. V. Khotyaintsev, P.-A. Lindqvist, C. M. Cully, A. I. Eriksson and M. André, *In-flight calibration of double-probe electric field measurements on Cluster*, Geosci. Instrum. Method. Data Syst., 3, p.143-151, (2014).